HOW NEURONS EXPLOIT FRACTAL GEOMETRY

by

JULIAN SMITH

A DISSERTATION

Presented to the Department of Physics
and the Graduate School of the University of Oregon
in partial fulfillment of the requirements
for the degree of
Doctor of Philosophy

June 2020

DISSERTATION APPROVAL PAGE

Student: Julian Smith

Title: How Neurons Exploit Fractal Geometry

This dissertation has been accepted and approved in partial fulfillment of the requirements for the Doctor of Philosophy degree in the Department of Physics by:

Tristan Ursell	Chair
Richard Taylor	Advisor
Benjamín Alemán	Core Member
Cris Niell	Institutional Representative

and

Kate Mondloch	Interim Vice Provost and Dean of the Graduate School

Original approval signatures are on file with the University of Oregon Graduate School.

Degree awarded June 2020

DISSERTATION ABSTRACT

Julian Smith

Doctor of Philosophy

Department of Physics

June 2020

Title: How Neurons Exploit Fractal Geometry

Neuroscientists do not fully understand why neurons acquire their morphology and specific dendritic structure. This is important knowledge because the shape of neurons is connected to the health and computational power of the brain; it determines the number, type, and the robustness of the connections; and it may lead to improvements in retinal prostheses. Previous research indicated that the shape of electrodes may influence the stimulating power and bio-compatibility of retinal prostheses and any device that interfaces between brains and machines. In the first part of this dissertation, we worked with 3D reconstructions of adult CA1 rat hippocampal neurons and used fractal analysis to look at their physical properties, such as their mass, surface area, bounding area, and their dendritic profile. We altered the morphology of the neurons to investigate three fundamental questions: 1) To what extent are neurons fractal? 2) Where did the fractal shape come from? 3) Why are they fractal? We developed a framework to answer these

questions and further apply that framework towards the understanding of why a neuron would establish a planar versus non-planar dendritic morphology. In the following section of this dissertation, we focused on the general application of this research, specifically in the hopes of restoring vision and improving retinal prostheses. We compared three electrode designs that could one day achieve this goal by replacing damaged photoreceptors, stimulating healthy neurons, and utilizing the rest of the functional retina to transmit an appropriate signal to the brain. In the final section of this dissertation, we propose an experiment to assess the connection between the neurons and the electrode, which is based on the information and knowledge gathered from the previous sections and informed by our research at the University of Oregon. This dissertation includes previously unpublished co-authored material.

CURRICULUM VITAE

NAME OF AUTHOR: Julian Smith

GRADUATE AND UNDERGRADUATE SCHOOLS ATTENDED:
University of Oregon, Eugene, OR
Washington State University, Pullman, WA

DEGREES AWARDED:
Doctor of Philosophy, Physics, 2020, University of Oregon
Master of Science, Physics, 2020, University of Oregon
Bachelor of Science, Physics, 2011, Washington State University

AREAS OF SPECIAL INTEREST:
Fractal Geometry
Fractal Analysis
Architectural Design
Neurons
Visual Perception of Fractals
Education

PROFESSIONAL EXPERIENCE:

Graduate Research Assistant, University of Oregon, Eugene, OR (2015-2020)

Graduate Teaching Fellow, University of Oregon, Eugene, OR (2013-2015, 2020)

Consultant, Fractals Research LLC, Eugene, OR (2015-2020)

Instructor, North Star Program, Eugene, OR, (2016)

Participant, Neurotechnologies for Analysis of Neural Dynamics, Princeton, NJ, (2016)

GRANTS, AWARDS AND HONORS:

Architectural Product of the Year Award (USA, 2019)

Gold in the Nightingale Awards Competition (Healthcare Design Expo, USA, 2019)

Buildings Merit Innovation Award (USA, 2019)

The Interior Design HiP Award (USA, 2019)

The NeoCon Best of Show Innovation Award (USA, 2019)

The Metropolis NYC-DESIGN Award (USA, 2019)

Honorary Interior Design NYC-DESIGN Award (USA, 2019)

Weiser First-year Teaching Assistant Award, University of Oregon, 2014

PUBLICATIONS:

Julian H. Smith, Conor Rowland, Bruce Harland, Saba Moslehi, Rick D. Montgomery, Kris Schobert, William J. Watterson, John Dalrymple-Alford, and Richard P. Taylor. How Neurons Exploit Fractal Geometry to Optimize their Network Connectivity. *submitted*

Saba Moslehi, Julian H. Smith et al. The use of fractal geometry to enhance the assembly of retinal cells on patterned electrodes. *in preparation*

William J. Watterson, Saba Moslehi, Kara M. Zappitelli, Julian H. Smith, David J. Miller, Conor T.Rowland, Julie E. Chouinard, Stephen L. Golledge, Richard P. Taylor, Maria-Thereza Perez, and Benjamn Alemn (2020). The Roles of an Aluminum Underlayer in the Biocompatibility and Mechanical Integrity of Vertically Aligned Carbon Nanotubes for Interfacing with Retinal Neurons. *Micromachines*, 11, 546

Julian Smith, Conor Rowland, Saba Moslehi, Richard Taylor, Anastasija Lesjak, Martin Lesjak, Sabrina Stadlober, Luis Lee, Jackie Dettmar, Mark Page, and Jeanette Himes (2020). Relaxing Floors: Fractal Fluency in the Built Environment.*Nonlinear Dynamics, Psychology, and Life Sciences*, 24(1):127–141

R. P. Taylor, T. P. Martin, R. D. Montgomery, J. H. Smith, A. P. Micolich, C. Boydston, B. C. Scannell, M. S. Fairbanks, and B. Spehar (2017). Seeing shapes in seemingly random spatial patterns: Fractal analysis of Rorschach inkblots. *PloS One*, 12(2)

William Watterson, Saba Moslehi, Julian Smith, Rick Montgomery, and Richard Taylor (2016). Fractal Electronics as a Generic Interface to Neurons. In *The Fractal Geometry of the Brain*,553–565

Melissa H. Dancy, Charles R. Henderson, and Julian H. Smith (2014). Understanding Educational Transformation: Findings from a Survey of Past Participants of the Physics and Astronomy New Faculty Workshop. In *2013 Physics Education Research Conference Proceedings*,113–116, Portland, OR. American Association of Physics Teachers.

Rick Lytel, Shoresh Shafei, Julian H. Smith, and Mark G. Kuzyk (2013). Influence of geometry and topology of quantum graphs on their nonlinear optical properties.*Physical Review A*, 87(4)

ACKNOWLEDGEMENTS

To feel unconditional love, without the pressure of expectation or judgement is an incredible gift. I am so grateful to my parents, Katharina Hirsch and Greg Smith, and my brother, Nick Smith, for providing me with that gift. I am so proud of you all.

I'd like to thank my advisor, Richard Taylor, for his creativity, optimism, and unparalleled ability to manifest a diverse set of experiences. Never would I have anticipated, that with your guidance, I would not only have contributed to the advancement of physics, neuroscience, and psychology, but also have won numerous design awards.

I'd like to thank my committee, Tristan Ursell, Benjamín Alemán, and Cris Niell, for their continued guidance and support. Tristan, you taught my favorite course in graduate school, provided resources for our group at a critical time, and were an excellent person to talk to for all the moments in-between. Ben, you have always been incredibly supportive of my research interests, provided resources and expertise, and brought an insatiable curiosity to the table. Cris, you bring a clarity of thought that I deeply appreciate. I'd like to thank Maria-Thereza Perez and Jayanth Banavar. Maithe, you helped me transition into the field of neuroscience with skill, humor, and some fantastic long lunches. Jayanth, your critical thinking and thought provoking questions have been incredibly illuminating in bringing our work to fruition. I would also like to thank Anastasija and Martin Lesjak. You provided the most fantastic introduction into the world of design. You both are stars. I am lucky that all of these individuals not only have brilliant minds, but are also exceptional people.

I'd like to thank my labmates and friends, Rick Montgomery, Bill Watterson, Saba Moslehi, Kara Zappitelli, Conor Rowland, and Willem Griffiths. Rick, you've been an inspirational resource and created the path for the bulk of the research presented here. Bill, I can't express how much I respect you as a researcher and friend. It is often that I wish to be doing nothing other than having a beer or playing a board game with you. Saba, you are one of the strongest individuals I know. Thank you for letting me borrow some strength from time to time. Kara, you're such a badass researcher and person. I admire your sincerity, candidness, and determination. Conor, thank you for bringing your energy and ideas into our research, without you, this work wouldn't be nearly the same.

I'm fortunate enough to have a tremendous support system at home. I'd like to thank my housemates, Ian, Caleb, and David. I'll never forget the farmhouse, nor the many adventures we've had exploring the world together. I look forward to all of our future adventures. Additionally I'd like to thank Nick, Caleb, and David again, as well as Pat and Spencer, who helped me in the final strides of preparing this document.

Finally, I'd like to thank all my friends. Together we've built a wonderful community. Thank you for the late night conversations, humor, games, dancing, and vibrancy. Together we make this world a better place every day.

The research in this dissertation was funded by W M Keck foundation.

TABLE OF CONTENTS

LIST OF FIGURES

Figure Page

Figure Page

LIST OF TABLES

Table Page

CHAPTER I

INTRODUCTION

The natural world is full of useful systems which derive beauty from how elegantly they pack function into a seemingly complex, but fundamentally simple, form. Trees reach to the sky, collecting light to photosynthesize, lungs fill the chest cavity supplying oxygen to the bloodstream, and arteries deliver that oxygen throughout the body to keep tissue alive. It is not surprising that form is intimately tied to function, given how integral that relationship is in natural selection. To accomplish these demanding requirements biological structures often use one of nature's most ubiquitous tools, fractal geometry.

Fractals are frequently utilized in nature because they optimize the balance between cost and benefit. Often surface area is highly valued, while mass and/or volume is costly or constrained. For instance trees use the surface area of their leaves to collect light, and oxygen uses membrane surface area for diffusion either out of the lungs, or the bloodstream. Perhaps it should have been expected then that the brain, and it's processing unit, the neuron, exhibit fractal qualities [1, 2, 3, 4, 5, 6, 7].

Neurons are the crucial processing cell in the central nervous system (CNS) of nearly all animals. They are largely responsible for how we think, feel, and move. Originally the entire CNS was thought to be one continuous network of cells, without gaps between the cells. In 1887 Santiago Ramón y Cajal challenged this theory when he used a relatively new neuron staining technique to produce intricate drawings of neurons which lead to the current scientific understanding - the CNS is composed of discrete cellular units. Immediately a question arises -

what dictates the complexities of one neuron connecting with another? It speaks to the diversity and complexity of the CNS that we still do not fully understand this question. Then, in 1931 a science fiction concept is ignited when Frankenstein was adapted to film - can we use electrodes to connect to the body and brain? Since then science fiction has become science fact.

Electrodes are a powerful tool in medicine, research, and technology. They have been widely used to regulate heart rhythms with a pacemaker [8], restore hearing with cochlear implants [9], alleviate Parkinson's tremors with deep brain stimulation [10], enable fully functioning prosthetic limbs [11], and even restore sight to the blind with retinal implants [12]. Furthermore, incorporating fractals into electrode design is promising. Simulations show that the electrical properties of small-scale fractal electrodes will efficiently stimulate neurons [13, 14]. Fractals are mechanically flexible, a desirable property for implanting electrodes in the curved space at the back of the eye [15]. Fractals exhibit favorable optical properties including extraordinary transmission of light [16, 17] (where the light transmitted through an electrode is greater than a naive 'pixel count' predicted by ray optics) and tuning of the transmitted wavelength optics [18, 19].

To fully utilize the benefits of these promising effects the neurons must be healthy and in close physical contact with the electrodes. This would require that 1) the neurons preferentially connect to the electrodes rather than the gaps between the electrodes, 2) glia, the support cell of the central nervous system, do not proliferate on the electrodes, and build up scars, 3) glia proliferate in the gaps and are close enough to provide their health benefits. During my Ph.D. we have spent a significant amount of time investigating systems that promote the aforementioned conditions on large-scale electrodes (Area $\approx 36\ mm^2$).

We designed experiments with carbon nanotubes (CNTs) as the electrode material because they promote neuron adhesion and growth, yet they inhibit glial proliferation. By patterning the CNTs into fractal geometries with multi-scaled interconnected gaps we encouraged glial proliferation in the gaps, thereby keeping those glial cells close to the neurons on the CNTs. In addition, we identified a network organization in the gaps that we labelled a small-world network. We did so because observations of the identified small-world network match the general properties of small-world networks in the literature [20, 21, 22], thereby implying efficient communication flow between neurons. These neurons in the gaps then connect to the neurons on the electrodes. Therefore stimulated neurons on the electrode could additionally pass a signal to the CNS via the small-world network in the gaps.

We have spent a significant amount of time investigating large scale electrodes, but in order to achieve better electrodes appropriate for most applications we need to shrink electrodes down to the size scale of an individual neuron. This is necessary from a technological point-of-view because the stimulating and recording resolution increases with decreasing electrode size. For instance, currently retinal implant technology can restore vision such that an individual might be able to identify where the door in a room is, but it is far from the theoretical maximum, which would allow an individual to recognize a loved one's face[23].

How we design small-scale electrodes that interface with neurons is a focus of our research and a practical aim of this dissertation. What if we fabricated electrodes at the size scale of a neuron such that they had the same characteristics or complementary characteristics to the neurons that are meant to attach to

them? Would they become more biophilic? Would there be other enhanced favorable responses? We specifically ask whether designing a fractal electrode with characteristics complementary to a neuron, which has been identified as having a fractal morphology, would provide a favorable response. In order to design such an electrode it would be useful to understand the fractal qualities of a neuron. However, although there is a general understanding that neurons are fractal, central questions have not been explored.

In this dissertation we focus on the central questions necessary to understand the fractal-like morphology of neurons. To what extent are neurons fractal? What are the geometric properties that produce their fractal-like behavior (e.g. distribution of lengths, angles, etc.)? Why does a neuron have a fractal-like structure? Does it come from a balance between a neurons' costs and their need to connect to other neurons? Once we have addressed the above questions we return to our initial question on electrode design. We ask whether the fundamental qualities of neurons can be applied to electrode design even though their costs and benefits are not identical.

In this introduction we provide the language, subjects, and context for this dissertation. Later, we will make the claim that a fractal framework is an appropriate framework to discuss geometric properties and their implications for a neuron. Therefore it is critically important that the reader has a basic ken of what a fractal is, how we generate fractal geometries, and a method for measuring the fractal dimension. It is equally important that the reader understand the basic anatomy, functioning, and energetic costs associated with a neuron. We discuss glial cell properties because neurons rely heavily on them, and because they play a particularly notable role when the nervous system interacts with external

materials, such as electrodes. We describe the general structure and function of a subretinal implant, the specific electrode of our expertise. We then summarize relevant recent results from our group: neuronal and glial response to physical cues; neuron network formation when culturing on carbon nanotubes patterned into complex fractal geometries, and electrical properties for stimulating neurons at the single neuron scale [1].

In Chapter 2 we look at the fundamental behaviors of neurons. We investigate their branching statistics and how their connectivity and costs vary with the fractal dimension as the neurons are modified. We identify that neurons follow the relevant behaviors of H-Tree branching fractals. In Chapter 3 we apply the fractal framework established in Chapter 2. We introduce a cost-benefit formalism that we first use to calculate the behaviors of the CA1 hippocampal neurons using heavily constrained exact H-Tree models. We then use these H-Tree models to investigate whether a more ED2 or ED3 morphology is advantageous. We apply the same framework to electrode design, accounting for the differences between them and neurons. Finally in Chapter 4 we integrate our findings and propose an experiment to look at the fundamental behaviors of neurons as they maintain proximity to electrodes. We design it to maximize the chances of a neuron process following an electrode once it has been reached, and to learn the fundamental branching dynamics of a neuron as it grows along an electrode.

1.1. Fractals

Fractals are self-similar objects in mathematics and nature [25], where self-similar refers to having the same statistical characteristics, such as space

[1]For a detailed description of the experiments referenced in this introduction the reader should see the dissertations of S. Moslehi [24] and W.Watterson [23]

filling properties, at increasingly small size scales. This property leads to a scale-invariance, where one cannot determine the degree of magnification purely from appearance, because without a priori knowledge there are no known measures of length to use as a guide. In mathematics, fractals can repeat exactly and infinitely. For instance, Fig. 1.1a shows an exact branching fractal that can be zoomed in on at specific scales to show the exact same pattern repeated. In nature, fractals are statistically self-similar and only repeat over a finite length range. For example, the tree branches in Fig. 1.1b are statistically self-similar over a few orders of magnitude. In this dissertation we will deal with both exact (e.g. H-Trees Fig. 1.12) and statistical fractals (e.g. Neurons Fig. 1.6).

Fractal scaling is motivated by the way that three primary Euclidean shapes (a line, a square, a cube) scale with size. Consider the one-dimensional line in Fig. 1.2. The number of lengths N increases as L decreases in the following way: $N = (L/L_1)^{-1}$, where L_1 is the length of the undivided line. For a square, the number grows as $N = (L/L_1)^{-2}$. Finally, for a cube, the number of units that fill a three-dimensional space grows by $N = (L/L_1)^{-3}$ as L is decreased. In each instance, the negative of the exponent is the intuitive value for the dimension of the object. The line is a 1D object, the square 2D, and the cube 3D. A scaling relationship with a generalized dimension D is written as,

$$N \propto (L/L_1)^{-D}. \tag{1.1}$$

Fractal shapes also follow this scaling relationship but allow for non-integer, or fractional, values of D. [2]

[2]Benoit B. Mandelbrot coined the term fractal in his book *The Fractal Geometry of Nature*[25].

FIGURE 1.1. Mathematical and natural branching fractals.(a) The mathematical branched fractal features an exact, infinitely repeating pattern when zoomed in at increasingly fine size scales.(b) The tree branch pattern statistically repeats at finer size scales. However, as with all fractals in nature, the scaling range over which it is self-similar is finite.

We use this scaling relationship to measure the dimension of a fractal with a tool called box counting. This tool directly measures the amount of space an object occupies at different size scales (Fig. 1.3). As with the Euclidean example, we can count the number of boxes filled, N, at each new box size, L. The exponent D, if consistent over many different box sizes, gives us our fractal dimension. The scaling range refers to the variation in box sizes in which an object maintains a consistent D value [26]. For natural fractals, we typically expect a scaling range of at least an order of magnitude. We do note though, that just because

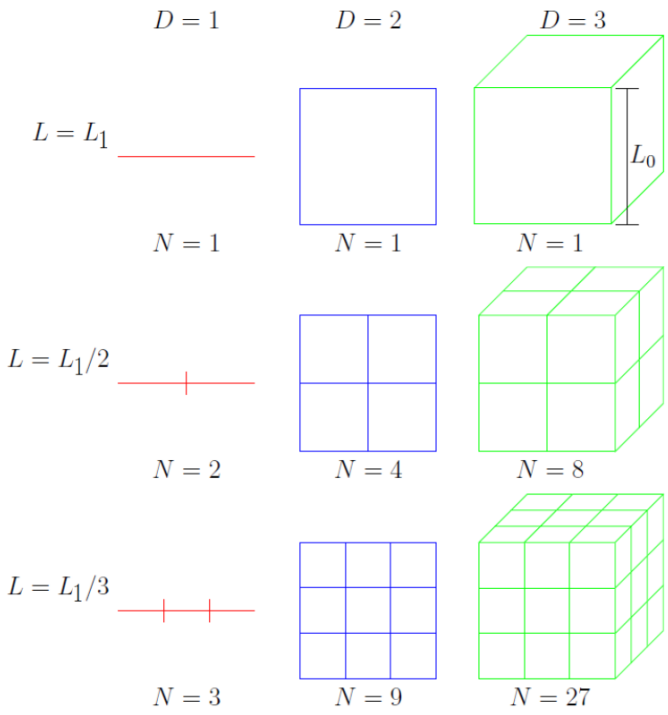

FIGURE 1.2. Scaling with euclidean dimensions. An intuitive idea of dimension is developed by measuring Euclidean objects, with different sized units, in one, two, and three dimensions. The number of units N that spans the object grows as L^{-D}, where L is scaling rate, and D is the dimension.

an object has a limited scaling range, does not necessarily mean that it is not fractal. In Section 2.5 we discuss in detail how the box counting fractal dimension is calculated.

An object cannot have a fractal dimension D greater than the space it is embedded within [25]. The embedding dimension is the fewest number of dimensions required to describe an object. All natural objects exist in the 3 dimensional world, but at different size scales an object might only use a portion of that space. Take a long cylindrical tube for example. If we zoom down to the atomic level, then we need all 3 dimensions to describe that object. Zooming out, each atom becomes point-like, but together they make a thin surface which we

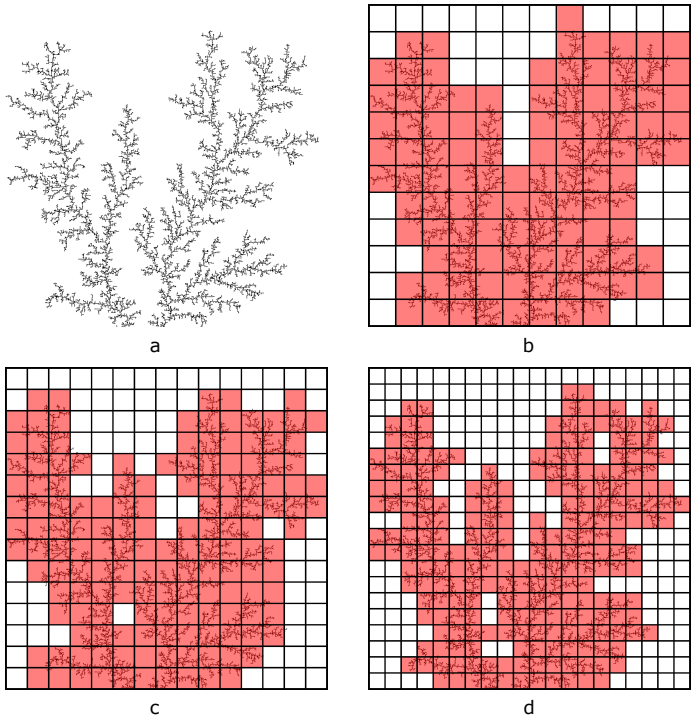

FIGURE 1.3. An example of counting boxes on a fractal tree. The number of colored boxes grows as a function of the box size in a non-integer power because the pattern is a fractal object. Reprinted with permission from the author [27].

can describe with 2 dimensions. Zooming out even further, we start to see the curvature of the tube and the hole going down its center. Eventually this becomes a long line, which can be described with 1 dimension. The number of dimensions needed to describe the tube at each size scale is the embedding dimension. Since the box counting dimension cannot exceed the space it is embedded within, the calculated D would be less than or equal to 3, 2, or 1 respectively. The size scale at which we look at an object, or the box counting sizes we choose, matters.

This is the same as with neuron models we analyze. The 3D reconstructions are sets of tubes that branch in complicated ways. Because we are interested in the branching pattern of the neurons, we will say that a neuron that extends into 2-dimensions at the size scale of its branching (greater than the branch width of

$\sim 2\mu m$ and less than the maximum displacement between any two points on the neuron) is defined as an embedding dimension 2 (ED2) object, whereas a neuron that extends into 3-dimensions is defined as an ED3 object. For our purposes the size scale of a neuron's branching is between the branch width of $\sim 2\mu m$ and the maximum displacement between any two points on the neuron which ranges between 185 μm and 690 μm.

We can use the same scaling relationship in equation 1.1 to generate fractals, where we only slightly modify how we think of the terms. L_1 becomes the size scale of a seed pattern, L the size scale of the current iteration, and N the number of new patterns in that iteration (Fig. A.1 & A.2).

For example, we use two different H-Tree constructions in this dissertation. Method 1 is most natural when investigating the behavior of neurons (Chapter 2 & 3), while method 2 is convenient when we compare different electrode designs, which we will explore at the end of Chapter 3. Method 1 has branches that decrease in length with every new branch. Starting with a straight branch at length L_1, we draw two shorter branches at right angles with reto the first through its endpoints. The length of each new branch is divided by $2^{1/D}$ (see A.1). This process is then repeated for each new branch, adding increasingly shorter lengths. Several H-Trees with different D values and numbers of iterations can be seen in Fig. 1.12 & 2.10. Method 2 uses an 'H', with equal height and width as the seed pattern, and iteratively adds smaller H's to the ends of each H (Fig. A.2). Both methods can be used to create ED2 and ED3 H-Trees.

We see that a higher D value has relatively more length at small size scales, and thus we say it has relatively more fine structure. Conversely, a low D value has relatively more coarse structure.

Mandelbrot introduced the term fractal geometry to describe physical objects as a way to allow comparison with mathematical patterns. He insisted that the term should only be used if it is a useful description for the object and if there is a physical reason for thinking the object is multi-scaled [25]. We apply fractals to our investigation of neurons and electrodes because, as we will show, both conditions are satisfied.

1.2. Inside the brain and retina

1.2.1. Neurons

A neuron is a cell in the nervous system that transmits information via electrical activity [28]. A typical neuron consists of a cell body (soma), dendrites, and an axon (see Fig. 1.4), and upon reaching maturity never divides. The axon extends from the cell body and often gives rise to many smaller branches. Dendrites also extend from the cell body and receive messages from other neurons. In general both dendrites and axons are referred to as neuron processes or neurites. Neurons make connections at synapses which can occur along the length of dendrites and axons, or at a processes end [29]. The receiving synaptic component on a dendrite is a spine, and the transmitting synaptic component on an axon is a bouton. Neurons have many spines along their dendrites. For example, a single pyramidal neuron in the hippocampal CA1 region possesses as many as 30,000 dendritic spines [30].

1.2.1.1. Neural stimulation

Neurons transmit information through electrochemical signalling. For chemical signalling, neurotransmitters are released from synaptic vesicles in the

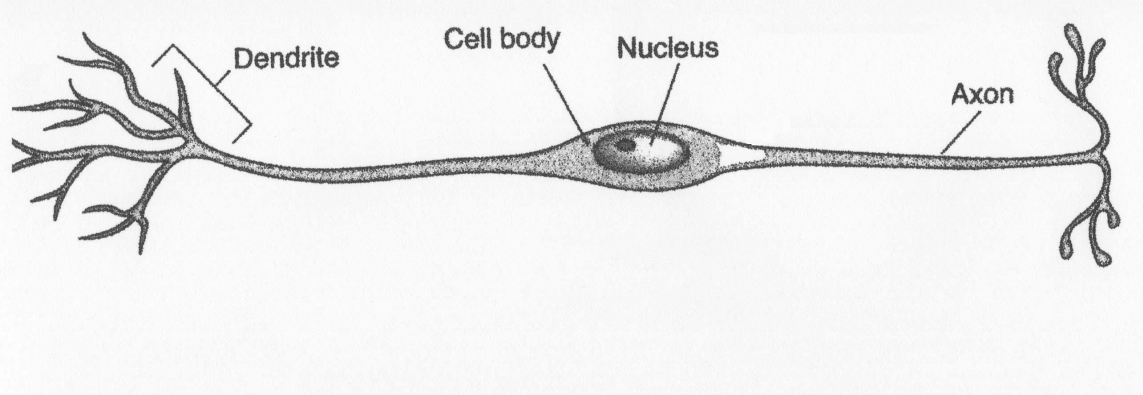

FIGURE 1.4. The anatomy of a neuron. A typical neuron consists of a cell body (soma), dendrites, and an axon. A retinal bipolar cell is shown.

presynaptic bouton and bind to the dendritic spine's postsynaptic receptors, which causes the receptor molecules to be activated in one of two general ways. Either ion channels are opened, causing different ions to enter or exit the cell, or the intensity of response to future neurotransmitters can be modulated [31]. For electrical signalling, a change in the electrical potential near the neuron results in ions flowing in or out of the neuron. These signalling mechanisms work because a neuron maintains a membrane potential, V_m, such that the intracellular potential, V_{in}, is less than their extracellular potential, V_{out}.

$$V_m \equiv V_{in} - V_{out}. \tag{1.2}$$

Neurons are *depolarized* if $V_m > 0$ or *hyperpolarized* if $V_m < 0$. The potential difference which prevents diffusion of ions across the membrane is known as the resting potential. For a typical mammilian neuron the resting potential is -70 mV.

In a passive neuron model, a neuron's membrane can be modeled as a resistor and capacitor in parallel (Fig. 1.5)[32, 33]. The membrane creates an impermeable separation between charged ions, i.e. a capacitor, while ion channels

establish a narrow pore for ions to flow through, i.e. a resistor. More complicated models (Hodgkin and Huxley) extend this same generic scheme to include selective channels for different types of ions [34] and are more appropriate for models which involve active signalling (e.g. action potentials).

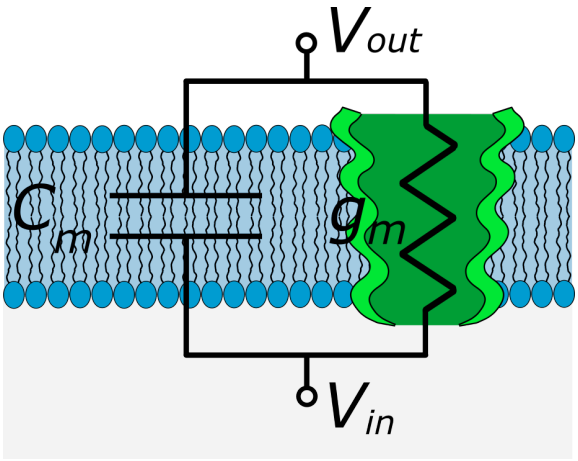

FIGURE 1.5. Passive cell membrane circuit model. The cellular membrane behaves as a resistor (ion channels) and capacitor (membrane) in parallel. The membrane capacitance is C_m and the membrane conductance is g_m. The membrane potential, V_m, results from an imbalance in ions and charged proteins between the intracellular and extracellular space. Reprinted with permission from the author [23]

Receiving signals causes the electrical potential within a neuron to change. For many neurons (e.g. CA1 pyramidal, Purkinje) if the incoming signals depolarize the neuron by a threshold amount ($\sim 15mV$), then they elicit a binary response in the receiving neuron, in which it transmits a signal through its axon (i.e. fires an action potential). If the inputs don't reach this threshold amount of depolarization then it stays silent to downstream neurons. Other neurons (e.g. retinal bipolar) transmit a signal via a graded potential, where the amplitude is proportional to the strength of the stimulus [29]. After the signal is transmitted in

either case, the neuron then spends energy to pump ions across the cell membrane such that it returns to its resting membrane potential [30].

Alternatively, one can bypass the synapses and apply an external electric field directly to a neuron which induces it to transmit a signal [35]. This property enables the design of electrodes for stimulating neurons, which can then pass signals downstream using prototypical mechanisms [36].

1.2.1.2. Neuron morphology

Neuron morphology can be drastically different (see Fig. 1.6). For example, CA1 pyramidal neurons have a distinct morphological shape with two sets of dendrites extending from opposing sides of it's soma in a fairly sparse network. As we will discuss again in Chapter 2 & 3, those dendrites have a broom-like shape, but satisfy the condition we established for ED3 objects. The Purkinje neuron takes a different approach. It forms a dense network with a single initial branch from the soma. In two dimensions, it's dendrites almost fill space entirely (Fig. 1.6b), but if looked at from another viewpoint we see that there is no extension into the third dimension (Fig. 1.6d). The Purkinje neuron satisfies the condition for an ED2 object.

1.2.1.3. Neuron energy expenditure and geometric costs

There are two types of energy expenditure in the brain, signalling and non-signalling. Signalling is the brain's primary mechanism for information processing and is carried out by neurons. This includes energy used for action potentials, synaptic transmission, and maintaining resting potentials. These processes are largely driven by energy in the form of adenosine triphosphate (ATP)

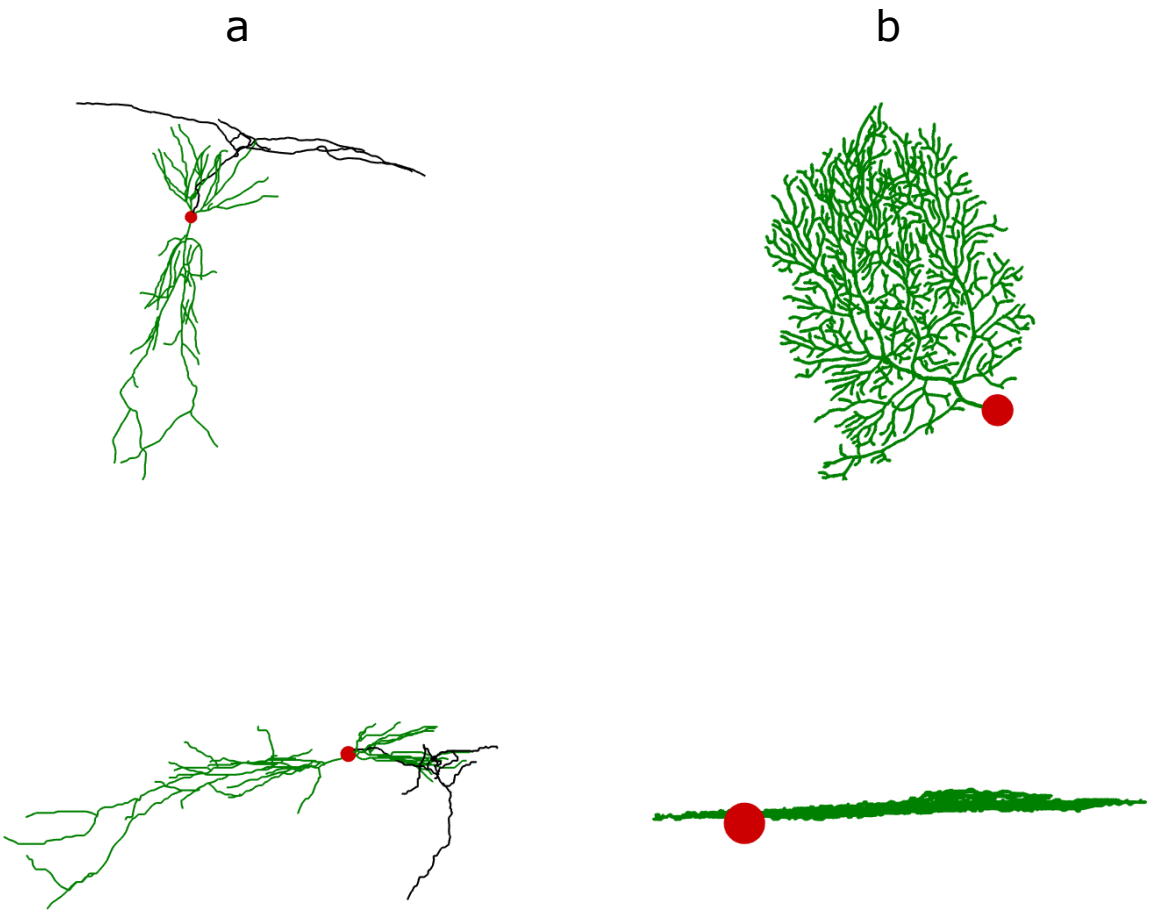

FIGURE 1.6. Example neuron morphology. Two example neurons (column a & b) are shown from two distinctive viewpoints (top & bottom row). Dendrites are shown in green, the soma in red, and the axon in black. (a) CA1 Hippocampal Neuron, partial axon shown. Dendrites are broom-like but extend into all 3 dimensions (ED3). The soma diameter is 10 μm. (b) Purkinje neuron. Axon not shown. Dendrites are essentially planar (ED2). The soma diameter is 18 μm. Models reconstructed from neuromorpho.org [37].

being supplied to ion pumps throughout a neuron, which are located at both synapse and non-synapse surfaces. The amount of ATP expended is proportional to the membrane capacitance for action potential propagation or ion channel conductance in the absence of action potentials [38]. In both instances, the energy is proportional to the membrane surface area.

The non-signalling energy expenditure in the brain is used for metabolism and to build/move material (e.g. actin treadmilling, microtubule dynamic instability, lipid turnover, protein synthesis, and mitochondrial proton leak).

Although both types of energy expenditures have many interwoven complexities, we can re-frame them in terms of geometric costs. We identified that the signalling expenditures can primarily be related to a surface area. Similarly we propose that the non-signalling expenditures can be described in terms of geometric costs such as mass, surface area, process length, and occupying space. For example, lipid turnover is necessary to maintain a healthy cell membrane, which varies with surface area [39];the energy required for protein synthesis would be much greater with a more massive cell [40]; and during the construction of processes, neurons must consider the boundaries of other cells, incurring an occupancy cost[41]. This is particularly the case when it comes to neuron tiling, where neurons of the same type reduce their dendritic overlap [42, 43].

1.2.2. Glia

Glia are supportive cells in the central nervous system (CNS). They are as numerous as neuronal type cells, constituting 50% of the brain [44]. They have four main functions: surrounding neurons and holding them in place; supplying nutrients and oxygen to neurons; insulating one neuron from another; destroying pathogens and removing dead neurons. They also play a role in neurotransmission and synaptic connections. They have a wide variety of morphologies. Some have extensive dendritic tendrils, while others are more egg like (the shape they often take to divide), while still others take on the form of the structures they wrap

around (like axons). Unlike neurons, glial cells can differentiate and proliferate (divide) throughout their life.

Glial cells proliferate and enlarge as a reaction to trauma, infection, or neurodegeneration [45]. With severe damage a glial scar can form, which is a thick layer of glia through which neuron processes can no longer pass [46]. Unfortunately, electrodes induce trauma when implanted, and once a glial scar forms, it can inhibit the stimulation or recording capability of the electrode by pushing neurons far from the electrode site.

Glial scar formation can be reduced. Their formation decreases with implant size [47, 48, 49]. Completely wireless technologies reduce scar formation because they can limit downstream micromotions at the electrode site [36]. Another technique involves pre-loading an anti-glia drug on the implant [50]. Also, matching the stiffness of the natural environment by the insertion of soft hydrogels into the CNS can reduce scar tissue formation [51]. Finally, as Piret et al. (2015) showed, glia will preferentially proliferate on flat surfaces compared to textured ones, a technique that allows neurons to stay close to the electrodes that stimulate them [52].

1.2.3. Retina

Positioned at the back of the eye, the retina is responsible for the initial stages of visual processing (Fig. 1.7). The retina consists of different layers of neurons organized in two-dimensional sheets stacked on top of each other. Light entering the eye passes through the inner retina and activates rod and cone photoreceptors, which act like the pixels in a camera. Bipolar cells transmit a signal from the photoreceptors to ganglion cells, which transmit a digitized signal

to the brain. At the photoreceptor-bipolar interface, horizontal cells modify the signal, and at the bipolar-ganglion interface, amacrine cells modify the signal. Each step is complex but necessary for the brain to receive an appropriate signal.

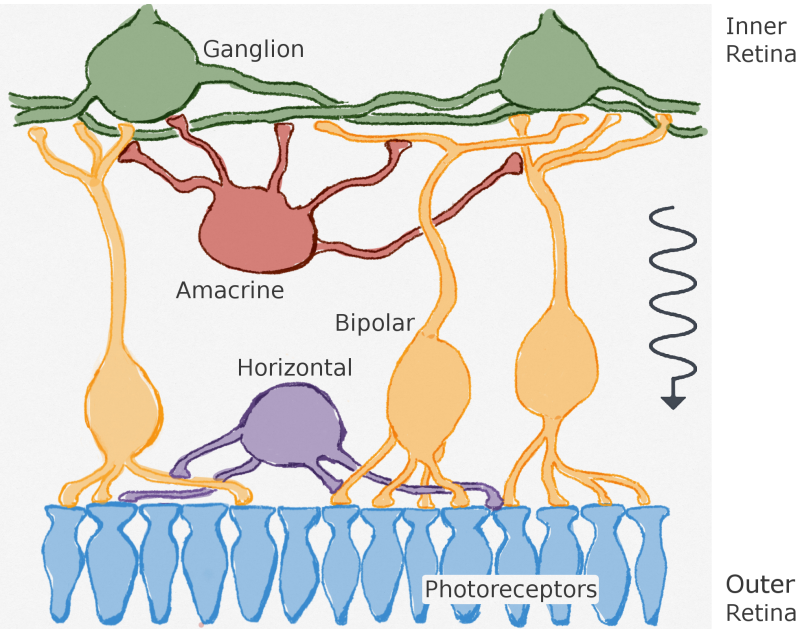

FIGURE 1.7. The structure of the retina. There are five main classes of neurons in the retina. Photoreceptors, horizontals, and bipolars all respond to light with graded potentials. Amacrine cells exhibit both passive and active membranes. Ganglion digitize the sum of signals from bipolars and amacrines and send action potential spikes to the optic nerve. Reprinted with permission from the author [23].

The three types of glia that exist in the retina are astrocytes, microglia, and Müller cells [45]. Astrocytes and microglia are located throughout the retina. Astrocytes provide a scaffold for neurons to grow on, regulate ionic concentrations, help form the blood brain barrier, provide a fuel reserve for neurons, help regulate blood flow, collect waste products and move them to the capillaries, and have a role in the structure and formation of synapses. Microglia are responsible for the elimination of microbes, dead cells, redundant synapses, protein aggregates, and

other debris that may endanger the retina. Müller cells extend through all retinal layers and are responsible for maintaining the structural and functional stability of the retina. They encapsulate neurons to improve synaptic coupling, maintain homeostasis, provide structural support, regulate the volume of the retina, and provide metabolites to microglia.

1.3. Subretinal implants

Subretinal implants have the potential to restore vision to blind patients without properly functioning photoreceptors. Retinitus pigmentosa (RP) and age-related macular degeneration (AMD) are two diseases that cause cell death in photoreceptors which leads to vision loss. Together, these diseases account for a global cost in excess of $343 billion, including $255 billion in direct health care costs. [53]. Subretinal implants (Fig. 1.8) replace the damaged photoreceptors with microphotodiodes combined with electrodes that directly stimulate bipolar neurons, but leave the remaining functional retina intact. Ideally a single microphotodiode would replace each photoreceptor. However, even with an electrode that has 4 times the area of 1-1 replacement, visual acuity could be restored to 20/80, allowing patients to read large font sized text and recognize faces [23].

In this dissertation subretinal implants with integrated photodiodes are discussed. When appropriate, the material of choice is vertically aligned carbon nanotubes (VACNTs). VACNTs are a promising material for electrodes because of their nanoscale morphology [54], flexibility [55], and double-layer capacitance [56]. All of the carbon nanotubes discussed in this dissertation are VACNTs and therefore the 'VA' portion will be dropped, leaving just CNTs.

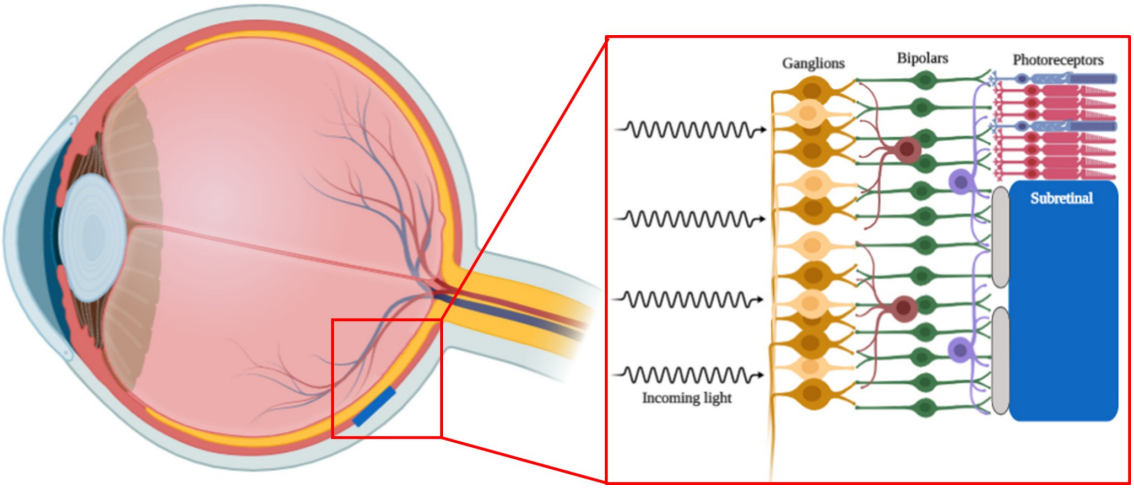

FIGURE 1.8. Schematic of the eye showing the position of a subretinal implant. The inset is a zoom in of the boxed area, indicating different neuronal layers in the retina. The subretinal implant is in contact with bipolar neurons. Reprinted with permission from the author [24]

Ideally, the implant is self-powered via the photodiode as it reduces the number and severity of complications [57]. This introduces a technical hurdle because the photodiode area required to power an electrode capable of stimulating neurons is large.

Because our focus is on electrodes for stimulating neurons, we will henceforth refer to any patterned material as an electrode, regardless of whether it is made of an electrode material or otherwise has the appropriate conditions for functioning (e.g. a power source).

1.4. *in vitro* experiments

It is well established that cells not only follow chemical cues, but also mechanical ones [58, 59]. One experiment attempted to answer whether chemistry or topography is the dominant surface cue in determining neural growth by seeding embryonic (E18) hippocampal neurons directly between PDMS microchannels

and immobilized neural growth factor [60]. Microchannels were 1 or 2 μm wide and 400 nm deep. In the presence of solely topographical cues or chemical cues, hippocampal axons preferentially grew from a flat area onto the striped pattern 70% of the time (Fig. 1.9), indicating that the elongating axons preferred topographical cues. In another experiment rows of gallium phosphide nanowires were fabricated and it has been shown that glial cells preferentially grew on flat surfaces between the nanowires [52].

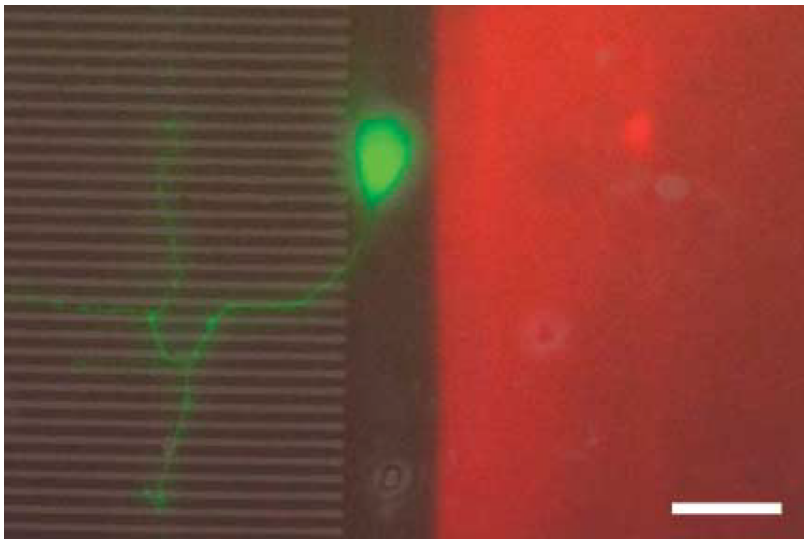

FIGURE 1.9. Axons prefer topographical over chemical surface cues. Hippocampal neurons placed between PDMS microchannels and neural growth factor preferentially grow axons towards the topographical surface cues. Scale bar, 25 μm. Image from Gomez et al. (2007).[60]

These studies motivated a set of *in vitro* experiments where we tested whether geometrically patterned CNTs could guide the proliferation of glial cells into regions away from the surface of the electrodes, as well as enhance neuronal adhesion and outgrowth on the electrodes surface. Neuron and glial cells were obtained from young mouse retinas. The retinas were dissociated such that individual cells without processes were suspended in a medium that was then

seeded onto the patterned CNT samples where they were allowed to re-grow processes and proliferate over days. After incubation, neurons and glial cells were fixed and marked with immunohistochemistry techniques such that they could be viewed in a fluorescence microscope.

By introducing rows of CNTs separated by rows of silicon, it was established that retinal cells follow mechanical cues. Next, by adopting H-Tree fractal electrode geometries while using the same materials, it was shown that the network formation of neurons and glial cells was modified compared to the row samples and also between different fractal H-Trees.

This section summarizes a set of observations that pertain to this dissertation from *in vitro* experiments performed by graduate students in the Taylor and Alemán labs. Saba Moslehi (SM) fabricated samples. SM, William J. Watterson (WJW), Kara M. Zappitelli (KMZ), Conor Rowland (CR) imaged and characterized CNT samples. David Miller (DM), KMZ, Curtis Colwell, Derek Hallman, and Benjamín Alemán (BA) designed and developed the VACNT synthesis process. DM built the CVD furnace, the gas delivery system, and wrote the CVD control software. SM, WJW, KMZ, Julian H. Smith (JHS), and CR performed cultures, immunohistochemistry and fluorescence imaging procedures. SM, WJW, and JHS developed the necessary image processing tools. SM and JHS performed image processing and developed data visualization tools. SM completed a statistical analysis of the data and analyzed the results. All students were trained on the culture protocols by Maria-Thereza Perez (MTP). Richard P. Taylor and (BA) were PIs on this project. For a full list of materials, methods, and results see the S.Moslehi dissertation [24].

1.4.1. Alternating rows of CNTs and flat Si

Alternating rows of CNTs and flat silicon (Si) with varying widths were used to understand how mechanical cues influenced retinal neurons and glia in the culture environment (Fig. 1.10). Neuronal survival, adhesion, and process growth were all enhanced on the CNTs compared to the flat Si. The nanoroughness [54] and lower rigidity [61, 62] of the CNT surfaces was preferred for neurons, but not ideal for glial cells, whose proliferation was hindered on the CNT surfaces due to the lack of motility [63].

Very few neuron clusters were seen on CNT surfaces. We proposed that this occurs for two predominant reasons. 1) Neuron motility is low on CNT surfaces and 2) neurons adhere strongly to the CNT topography. Therefore neurons would not actively move to form clusters, nor would they be as susceptible to other neurons that would pull them into a cluster. Glia were able to grow in size, often forming a dendritic structure, but very few were found on the CNT surface. Furthermore, neuron processes preferentially followed the edges of the rows when given the option. The smooth rigid surface of Si enhanced glial proliferation. On Si surfaces neurons were characterized by less process length but more clustering, the defining features of a small-world network [20] (Fig. 1.11). Although the parameters of a small-world network were never directly studied in these experiments, it was hypothesized that larger clusters observed on Si were the result of small-world network formation. This hypothesis is supported by other research which has previously shown experimentally that in-vitro neuronal networks tend to develop from a random network state toward a small-world configuration [21, 22].

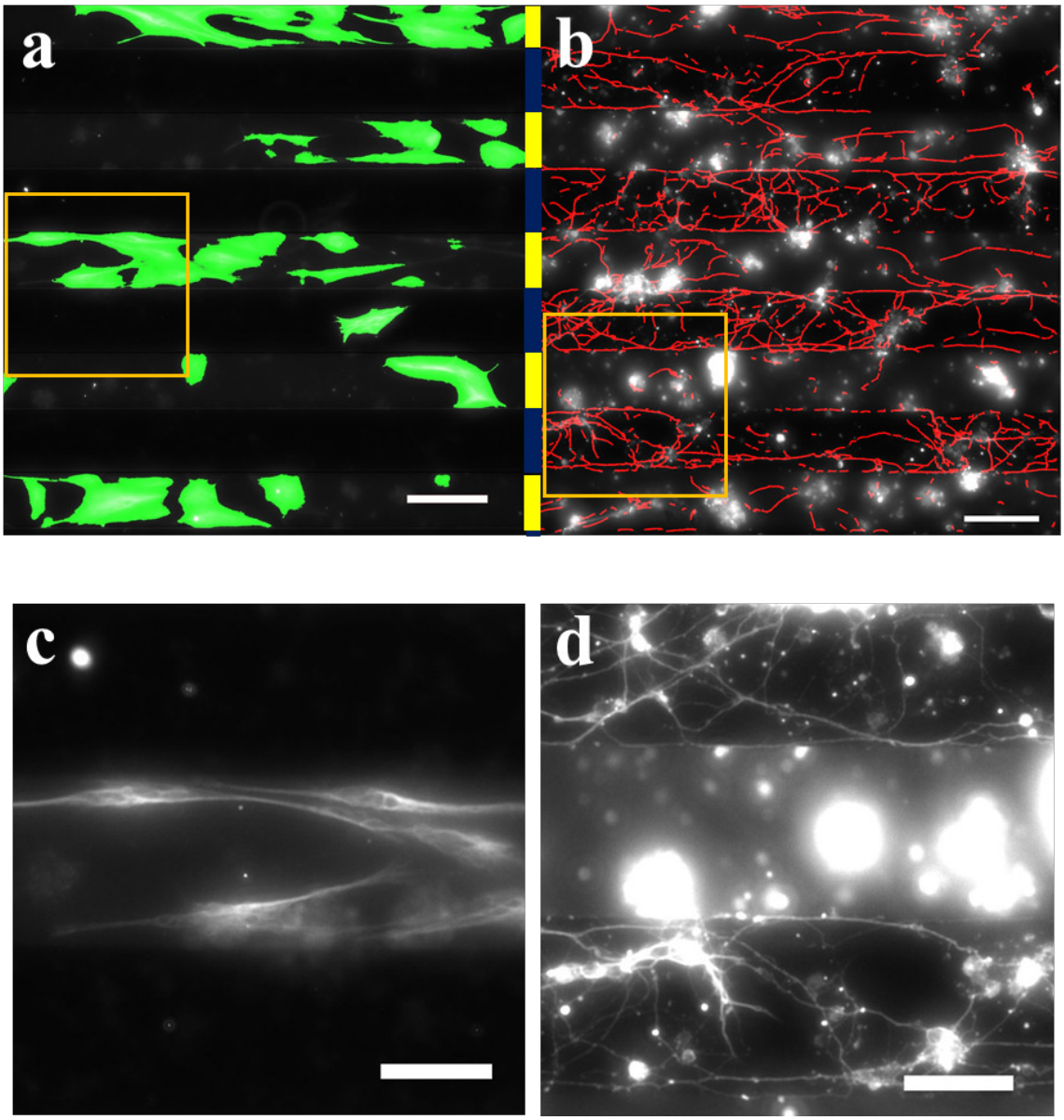

FIGURE 1.10. Schematic showing retinal cells following mechanical cues. Example of neuron processes and glial proliferation on alternating horizontal rows of CNTs (blue) and Si (yellow). Fluorescence image with analysis overlay of (a) glia area (green) and (b) neuron processes (red). (a) and (b) show separate glia and neuron channels of the same field of view. Glia are noticeably in the Si regions and neurons on edges of CNTs. (c,d) Zoom in on the marked area in (a) and (b) respectively without the analysis overlay. Scale bars are 100 m in (a,b) and 50 μm in (c,d). Modified with permission from the author [24]

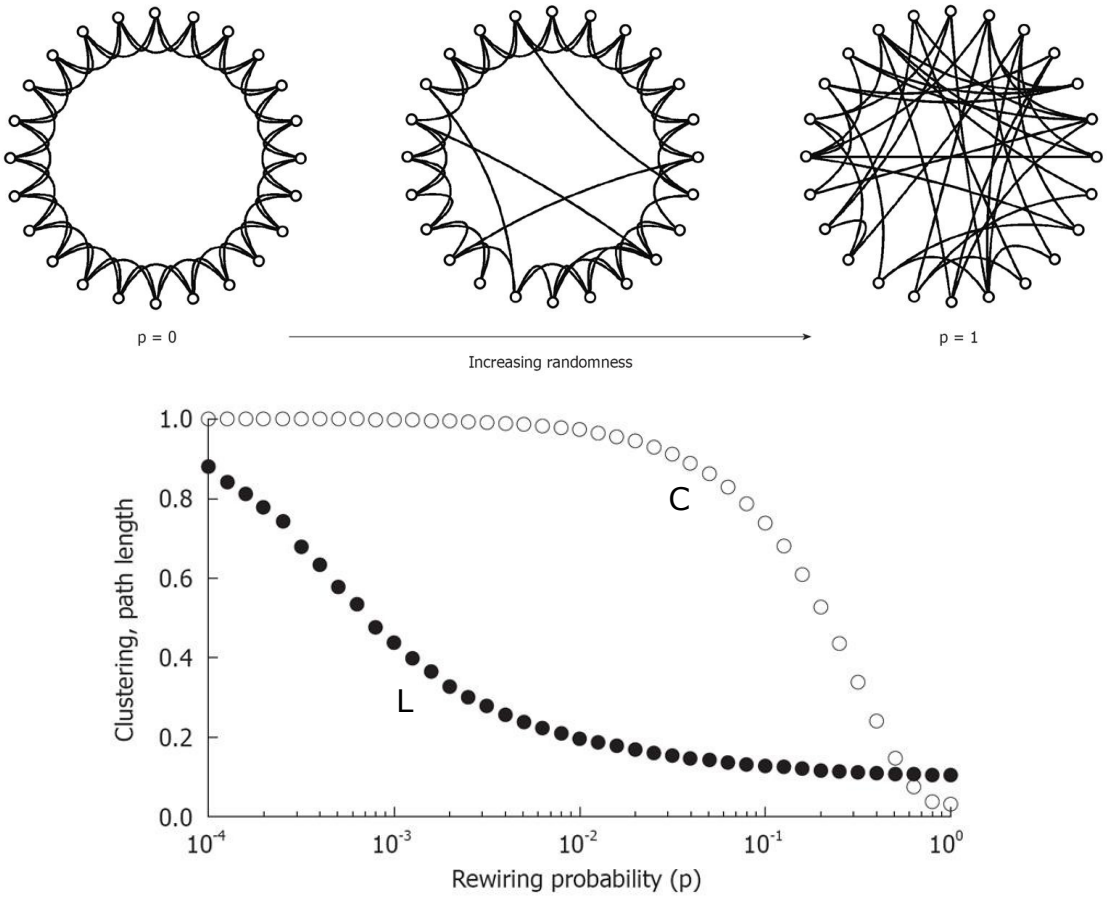

FIGURE 1.11. The Watts-Strogatz model of the small-world network. The rewiring networks are changed from regular grids to random networks by breaking and remaking links at random. Between the extremes (0 = regular grid, 1 = fully random network), the networks are 'small-world', with high clustering C and short average path lengths L between any two points (normalized)[64].

1.4.2. Small-world networks

Small-world networks are such that most entities (e.g. A neuron, airport, etc. Often referred to as a node) are not neighbors of one another, but the neighbors of any given entity are likely to be neighbors of each other and most entities can be reached from every other entity by a small number of hops or steps (Fig. 1.11). A neighbor refers to an entity that is directly connected to another, not necessarily

a physically close neighbor. For example, airport networks have been shown to be small-world [65], because many smaller airports are connected to an airport hub (e.g. Denver International Airport), forming a cluster, and that hub connects to other airport hubs. One cannot find a direct flight from Eugene to Berlin, but with just a few connecting flights, this trip is possible.

Small-world networks might be beneficial for networks of neurons for several reasons. First, the deletion of a random entity for some small-world networks has been shown to rarely cause a dramatic increase in the mean shortest path length [66], a sign that the network would be resiliant to cell death. Additionally, small-world networks are highly connected which enables efficient information flow, and adds to the strength of the networks as computational units. However, developing extended and vastly branched processes has a high energetic cost. A small-world network maintains this highly connected network while simultaneously reducing the amount of length, and therefore the energetic cost [22].

Ultimately, a simple system was created that successfully hindered glial growth on the surface of the electrode and improved neuronal growth, while keeping glia inside Si areas in close contact with neurons on both surfaces. Critically, the neurons that are stimulated on the electrode are connected to an efficient small-world network on the Si surface, thereby increasing the area of neurons that could connect to the retina and stimulate downstream neurons.

1.4.3. Fractal geometries

H-Tree fractals were generated (Fig. 1.12) with different D values (1.1, 1.5, and 2) and with iterations ranging from 4 to 6. We fabricated CNT structures on

a Si substrate out of these geometries and performed 17 day *in vitro* dissociated retinal cell cultures on them.

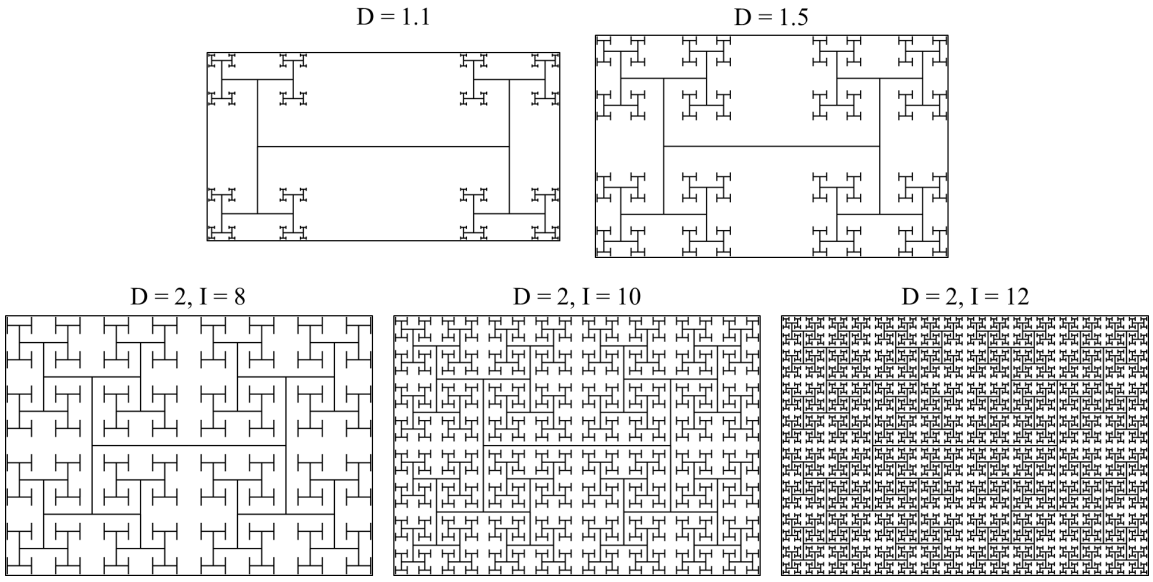

FIGURE 1.12. The set of H-Tree geometries used for *in vitro* experiments. H-Tree fractals were generated with different D values (1.1, 1.5, and 2) and with iterations ranging from 8 to 12 according to Equation 1.1. The width of the each pattern is approximately 6 mm with feature sizes of 20 μm. Reprinted with permission from the author [24].

The same general results observed in row samples also existed in fractal geometry samples. They confined the glial proliferation to Si regions and process length was increased on CNTs. Additionally, the interconnected Si space enhanced glial proliferation such that more glia were seen on fractal geometries compared to those of rows with the same culture duration. At the same time, the neural networks formed on the Si and CNT surfaces were influenced by changing distances of the aggregated cells on the Si.

Four distinct regions for neuron and glial behavior (Fig. 1.13) were identified. On CNTs, the neurons and glia behaved much like they did for the row samples, with some modulation due to the quality of the network on the Si (e.g. more

process length on Si was correlated with more process length on CNTs). The low motility of both glia and neurons meant that processes could extend, but proliferation and aggregation did not occur. For all of the other regions, neurons and glial cells are on the Si surface, where cells are motile. This motility means that glial cells have the opportunity to proliferate [63], but depending on their surrounding environment and the interaction with neurons, they show different behaviors. Neurons don't have as strong of an attachment to Si, so they can move, and be pulled more freely on this surface.

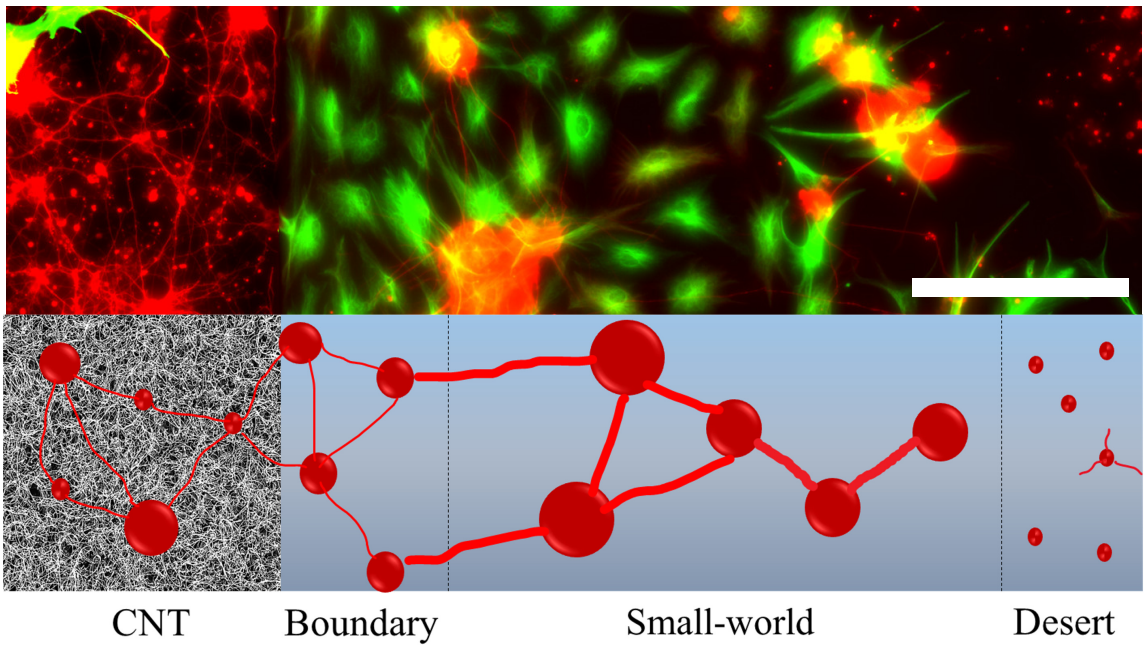

FIGURE 1.13. Retinal cell behavior when interacting with fractal geometries. In the 1st row a representative fluorescence image shows four distinct regions of neural and glial growth identified by the schematic in the 2nd row. Normalized neuron process length decreases from left to right. The small-world regions exhibit the most neuron clusters. Glial cells don't proliferate in the CNT region, but do proliferate a lot in the boundary region and the most in the small-world region. Glia don't proliferate much in the desert region, nor do neurons grow many processes there. The scale bar is 200 μm.

In the 'boundary' regions there are still a lot of anchoring locations provided because of close by CNTs. As neurons make connections with each other they are pulled by other neurons, but many of the neurons are still anchored by neighboring CNTs, therefore clustering has only a modest increase. Glial cells, now with the opportunity to proliferate, often do so to support the robust neuron network. Because a lot of these locations are heavily constrained by the pattern geometry, the area extent of proliferation is often smaller than they would be otherwise.

In the 'small-world' regions, neurons cluster the most and have reduced process length, but still form extensive networks. Here there are more open spaces between CNTs. Neurons are still linked via other neurons to CNT boundaries, but less of them make direct connections. Neurons pull other neurons into larger clusters, consequently reducing the number of processes in these regions, thereby increasing the efficiency at which information is transferred between neurons [67]. Glial cells have the most proliferation in these areas, providing vital support to the neurons.

The 'desert regions were observed furthest from the CNT electrodes. They contained mostly individual cells and very few small clusters with a few shorter processes extending from them. No neural network was observed, and few individual glial cells existed in these regions.

It was found that fractal geometries combined with a textured material could prevent glial scars from covering the electrodes and improve neuron-electrode connectivity while keeping glia close to neurons on both surfaces. Furthermore, we found that the development of the small-world network could be manipulated by changing the D value of the electrode, which in turn could theoretically modify electrode performance.

All of the aforementioned experiments were done *in vitro*, because it was advantageous in maintaining a controlled environment. In the future both explant and *in vivo* experiments are required to see if these results translate to an intact retina.

1.5. Stimulating neurons simulations

Fractal H-Tree geometries are not only useful at the network level, but also at the micro scale when stimulating neurons. A set of simulations showed how subretinal implants that use fractal electrodes give a restoration in visual acuity, up to 20/80, whereas current devices return an acuity of 20/546 at best [23]. Equivalent voltages were applied to square, grid, and fractal electrodes on a $20\mu m$ photodiode (Fig. 1.14) [13]. Each design blocked the same amount of light from entering the photodiode. Charge distribution simulations demonstrate that a lot of charge resides on the bounding perimeter of the electrodes. Fractal electrodes have a large bounding perimeter, which provides a physical explanation for why they can hold much more charge. Additionally, gaps in the fractal electrode didn't reduce effective areas below the Euclidean values. Instead, the associated vertical side walls supply extra area for charge accumulation. The increased capacity to hold charge leads to the fractal electrode generating an extracellular field which extends further from the electrode surface, therefore increasing their stimulating power compared to conventional electrodes with the same covering area. (Fig. 1.14). Similar fractal designs with large areas for charge accumulation will be compared in Chapter 3.

Next, Watterson et al. tested a condition where the electrode voltages were assumed to be supplied by the underlying photodiode. They showed that by

optimizing the fractal electrode 74% less irradiation was required to stimulate all neighboring neurons when compared to the best optimized square. When the threshold irradiation in which the fractal stimulated all nearby neurons was applied, the square only stimulated ∼10% of neurons. The radiation requirements for the fractal guaranteed long-term, safe operation of the implant, whereas the square was very near the maximum permissible safety limit of light that can enter the eye [23].

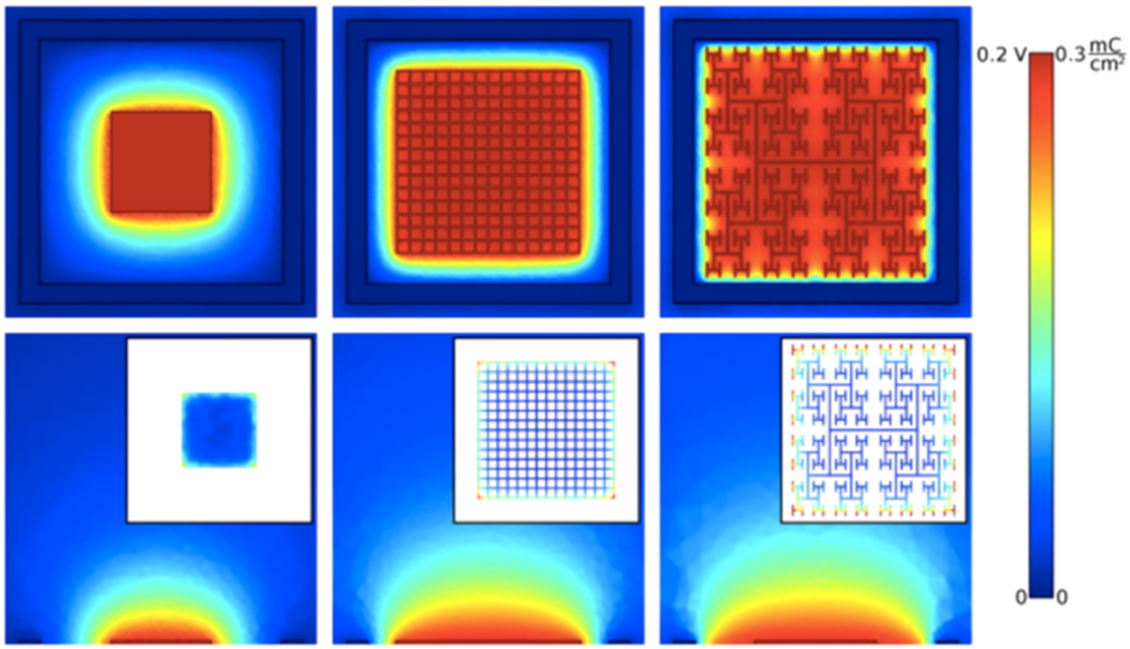

FIGURE 1.14. Electrical simulations of fractal electrodes. Comparison between a square, grid, and fractal extracellular voltages, which correspond to the neuron stimulating power of the electrode. The first row is the horizontal distribution of the voltages generated by a square, grid, and fractal with the same covering area. The second row shows the penetration of the voltage into the extracellular space for a vertical slice in the middle of the electrodes. The insets show the charge density distribution for each geometry. The bounding area of the outer square for all electrodes is 20×20 μm^2, and they are 250 nm tall. Reprinted with permission from the author [13]

CHAPTER II

HOW NEURON'S EXPLOIT FRACTAL GEOMETRY TO OPTIMIZE THEIR NETWORK CONNECTIVITY

This chapter includes work under review. The authors on the paper are J.H. Smith, C. Rowland, B. Harland, S. Moslehi, R.D. Montgomery, K. Schobert, W.J.Watterson, J.Dalrymple-Alford & R.P.Taylor. All authors participated in the study design. BH and JD-A created the neuron model reconstructions; JHS developed the fork and weave angle modification algorithm and the neuron model morphology analysis; JHS and RDM developed the box counting analysis; CR and KS developed the profile analysis; CR developed the H-Tree generation algorithm; JHS, CR, and SM developed the length scaling analysis; JHS, CR, and BH created the figures; all authors helped edit figures; RPT coordinated the project and drafted the manuscript; all authors edited the manuscript.

2.1. Abstract

We investigate the degree to which neurons are fractal, the origin of this fractality, and its impact on functionality. By analyzing three-dimensional images of rat neurons, we show the way their dendrites fork and weave through space is unexpectedly important for generating fractal-like behavior well-described by an 'effective' fractal dimension D. This discovery motivated us to create distorted neuron models by modifying the dendritic patterns, so generating neurons across wide ranges of D extending beyond their natural values. By charting the D-dependent variations in inter-neuron connectivity along with the associated costs, we propose that their D values reflect a network cooperation that optimizes these

constraints. We discuss the implications for healthy and pathological neurons, and for connecting neurons to medical implants. Our automated approach also facilitates insights relating form and function, applicable to individual neurons and their networks, providing a crucial tool for addressing massive data collection projects (e.g. connectomes).

2.2. Introduction

The prevalence of nature's fractals can in many cases be explained by the functionality resulting from their pattern repetition at multiple scales[1, 2, 25]. Along with trees, neurons are considered to be a prevalent form of fractal branching behavior [68]. Although previous neuron investigations have quantified the scaling properties of their dendritic branches, typically this was done to categorize neuron morphologies [1, 2, 3, 4, 5, 6, 7] rather than address the more profound question of how neurons benefit from their fractal geometry. Why does the body rely on fractal neurons rather than, for example, the Euclidean wires prevalent in everyday electronics? Neurons form immense networks within the mammalian brain, with individual neurons exploiting up to 60,000 connections in the hippocampus alone [69]. In addition to their connections within the brain, they also connect to the retina's photoreceptors allowing people to see, and connect to the limbs allowing people to move and feel. Given this central role as the body's 'wiring', we focus on the importance of fractal scaling in establishing the connectivity between the neurons [68]. Previous analysis over small parts of the neuron's dendritic pattern identified scale invariance as one of the geometric factors used to balance connectivity with the energetic cost of maintaining the dendrites[70]. In order to determine the precise role of the scale invariance along

with the most appropriate parameter for describing it, we first need to address more fundamental questions to what extent are neurons really fractal and what is the geometric origin of this fractal character? To do this, we construct 3-dimensional models of rat neurons using confocal microscopy. We show that, despite being named after trees, dendrites are significantly different in their scaling behavior. Whereas trees have famously been modeled using a fractal distribution of branch lengths, the ways in which the dendrites fork and weave through space are important for determining their fractal character. We demonstrate that fractal dimension D is a highly appropriate parameter for quantifying the dendritic patterns because it incorporates dendritic length, forking and weaving in a holistic manner that directly reflects the neuron's fractal-like geometry. Serving as a measure of the ratio of fine to coarse scale dendritic patterns, we use D to directly map competing functional constraints - the costs associated with building and operating the neuron's fractal branches along with their ability to reach out and connect to other neurons in the network. By investigating 1600 distorted neuron models with modified dendrite length, forking and weaving behavior, we propose that the neuron D values reflect a network cooperation that optimizes these constraints, with connectivity outweighing cost for neurons with high D values. Remarkably, D captures this functional optimization even though the fractal-like scaling behavior occurs over a highly limited range of size scales.

We use confocal microscopy to obtain images of CA1 pyramidal neurons in the coronal plane of the dorsal rat hippocampus (Fig. 2.1a, Fig. 2.5). Their somata are located in the stratum pyramidale (SP) of the CA1 region. Axonal and dendritic arbors extend from each soma, with the dendritic arbor featuring component apical and basal arbors. The complex branching patterns of these

dendritic arbors extend into the neighboring stratum radiatum (SR) and stratum oriens (SO) of the CA1 region where they collect signals from the axons of other neurons [69]. These axons originate either from within the CA1 region and connect to the dendritic arbors from every direction (e.g. O-LM cells, basket cells, bistratified cells and axo-axonic cells)[71], or they originate from other regions such as the neighboring CA2 which extends axons parallel to the strata (e.g. Schaffer collaterals). We construct three-dimensional models of the dendritic arbors from the confocal images of 100 neurons using Neurolucida software [72] (methods Section 2.5.2). The branches in the model are composed of a set of cylindrical segments which have a median length and width W of $2.4\mu m$ and $1.4\mu m$, respectively. The branch 'weave' angles θ are defined as the angles between connecting segments along the branch. We define the fork angle ϕ as the first of the branch weave angles (Fig. 2.1c, Fig. 2.6 and methods Section 2.5.2). The distinct median values for $\theta(11^\circ)$ and $\phi(34^\circ)$ motivated our approach of treating ϕ as a separate parameter from θ. Associated with each ϕ and θ value, there is an additional angle, ψ, measuring the segment's direction of rotation around the dashed axis in Fig. 2.1c. The branch length L is defined as the sum of segment lengths between the forks. As an indicator of arbor size, the maximum branch length L_{max} varies between 109-352μm across all neurons, with a median value for L/L_{max} of 0.24. Because each parameter (ϕ, θ, and L) features a distribution of sizes, we will investigate their potential to generate fractal branch patterns that repeat at multiple scales.

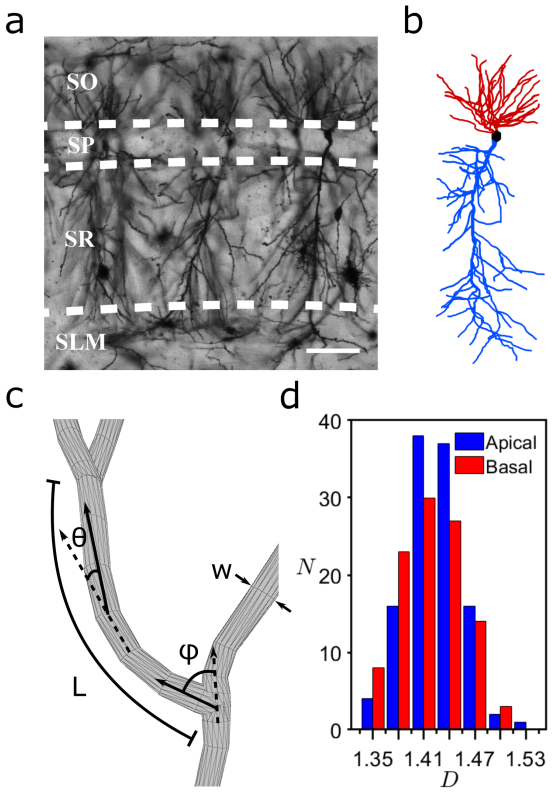

FIGURE 2.1. Neuron properties. (a) An example confocal micrograph (x-y layer) showing three neighboring dendritic arbors, each spanning the oriens (SO), pyramidale (SP), radiatum (SR) and lacunosum-moleculare (SLM) strata of the CA1 region. The dashed lines represent the strata boundaries and the bar corresponds to $100\mu m$. (b) A three-dimensional model of a dendritic arbor (reconstructed from a stack of micrographs in the z direction) featuring the apical (blue) and basal (red) arbors and the soma (black). The neuron's axon arbor is not shown. (c) Schematic showing the neuron parameters L, W, ϕ and θ. (d) Histogram of N that represents the number of neurons with a given D value, measured for the neurons' apical and basal arbors.

2.3. Results

2.3.1. Fractal analysis

In principle, a neuron could extend into the SR and SO layers following a straight line with dimension D = 1 or spread out and completely fill the space with a dimension of D = 3. If they instead adopt fractal branches, then these will be

quantified by an intermediate D value lying between 1 and 3 [25]. This fractal dimension quantifies the relative contributions of coarse and fine scale branch structure to the arbor's fractal shape (fractals with larger contributions of fine structure will have higher D values than fractals with lower contributions of fine structure). Whereas a variety of scaling analyses have been applied to neurons [5, 70, 73, 74, 75] here we adopt the traditional 'box-counting' technique to directly quantify their D value (methods Section 2.5.3). This technique determines the amount of space occupied by the neuron by inserting it into a cube comprised of a three-dimensional array of boxes and counting the number of boxes, N_{box}, occupied by the dendrites (Fig. 2.7). This count is repeated for a range of box sizes, L_{box}. Fractal scaling follows the power law $N_{box} \sim {L_{box}}^{-D}$. The histogram of Fig. 2.1d plots the number of neurons N with a given D value for both apical and basal arbors. The medians of their distributions are D = 1.41 (basal) and 1.42 (apical), indicating that their branches have similar scaling characteristics despite the apical arbors having longer branches that typically feature more forks. Given that D can assume values up to 3, it is intriguing that the dendrites' D values are relatively low. Additionally, the scaling range over which the neurons can be described by this D value is limited to approximately one order of magnitude of L_{box} (methods Section 2.5.3). This is inevitable because the coarse and fine scale limits are set by the widths of the arbor and its branches, respectively (methods Section 2.5.3). We will show that this scaling behavior is so effective that its limited range is sufficient for the low D values to optimize the connectivity process. Accordingly, D serves as an 'effective' fractal dimension for quantifying neuron functionality despite lacking the range associated with mathematical fractal exponents.

To clarify this favorable functionality, we first need to determine which parameters (L, θ, and/or ϕ) contribute to the neuron's fractal-like character. In mathematics, fractals can be generated by using forking angles (e.g. Self-contacting Trees), weave angles (e.g. Peano curves) or branch lengths (e.g. H-Trees) [25]. Because many mathematical fractals are generated by scaling L, we start by comparing the neurons' L behavior to that of H-Trees. Fig. 2.2 shows the scaling relationship of N (the number of branches with a given L/L_{max}) measured for a D = 1.4 H-Tree (Fig. 2.2a, c, e) and a typical basal arbor (Fig. 2.2b, d, f). We assign the branch iterations such that i = 1 corresponds to branches emerging from the soma, i = 2 to the branches emerging from the first forks, etc., with neurons featuring a median of 7 iterations on the basal side and 24 iterations on the apical side (other common iteration assignments such as the Strahler scheme [76] generate similar findings to those below). The H-Tree exhibits the well-defined reduction in L/L_{max} as i increases and follows the expected power law decrease in N as L/L_{max} increases: the magnitude of the data line's gradient in Fig. 2.2e equals the H-Tree's D value of 1.4. This behavior is absent for the neuron: L/L_{max} doesn't depend on i in Fig. 2.2d nor does the Fig. 2.2f data follow a well-defined slope. The neurons' fractal-like character is even preserved when the L/L_{max} distribution is suppressed by setting all branch lengths equal (for the neuron shown in Fig. 2.2h, this common length is chosen such that the combined length of all branches matches that of the undistorted neuron of Fig. 2.2a). The median D value of the basal arbors drops from 1.41 to 1.30 during this suppression. This occurs because the lower branch iterations of the undistorted neuron are consistently shorter than the higher iterations [76] (Fig. 2.2d and Fig. 2.8). This characteristic is removed when the branch lengths are equated,

so pushing the branches further apart and generating the drop in the ratio of fine to coarse structure seen in comparisons of Fig. 2.2b and Fig. 2.2h. Significantly, when we similarly suppress their branch length distribution, H-Trees with a sufficient number of iterations exhibit the expected non-fractal behavior (D = 3) for ϕ= 90°, but display the limited-range fractal behavior if we instead assemble the H-Tree using the neurons' median ϕ value (Fig. 2.2g). This highlights the important role of angles for determining the fractal-like appearance.

This finding opens up an appealing strategy for exploring how the neuron's D value influences its functionality. In Fig. 2.3, we mathematically manipulate the weave angles by multiplying every θ value by a common factor α. This changes the neuron's D value as follows. Values of α higher than 1 increase the weave angles above their natural values and cause the neuron branches to curl up. We set the highest value to be $\alpha = 2$ to ensure that branches rarely intersect. As shown by the blue line in Fig. 2.3, this curling process causes the D value to rise because the amount of fine structure in the neuron's shape increases. Similarly, reducing α causes the branches to gradually straighten out and this reduces the amount of fine structure and D drops. Fig. 2.3 includes a visual demonstration of this curling process. Interestingly, a key feature of curling - that total branch length does not rise with D - is also displayed by the undistorted neurons (and deliberately incorporated into our H-Trees), further emphasizing the appropriateness of this technique. Applying this technique to ϕ and θ simultaneously, we find that either increasing or decreasing α results in a rise in D. This is because the branches move closer together, which generates an increase in the ratio of fine to coarse structure (note: approaching the extreme case of α= 0, the neuron will eventually collapse down to a one-dimensional line).

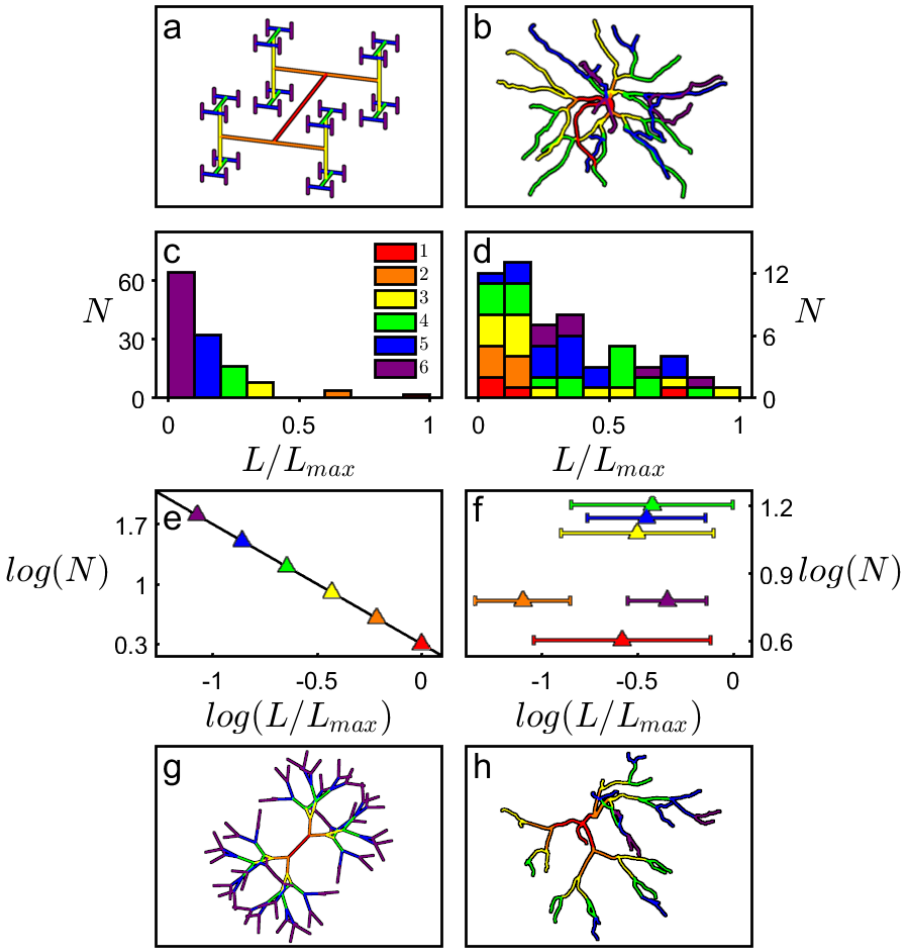

FIGURE 2.2. Neuron branching distribution. A D = 1.4 H-Tree fractal with W = $1\mu m$(a) and an example basal arbor with median W = $1.4\mu m$ (b). The branch iteration i is colored as follows: red (1st branch), orange (2nd), yellow (3rd), green (4th), blue (5th) and purple (6th). Histograms for an H-Tree (c) and neuron (d) plotting the number of branches N with a given value of L/L_{max}. Panels (e) and (f) show the analysis of (c) and (d) plotted in log-log space. Panels (g) and (h) take the H-Tree and neuron shown in (a) and (b) and adjust all their branch lengths to be equal. Additionally, the H-Tree's forking angle ϕ has been adjusted to 35.8°(the median value of the basal arbors).

2.3.2. Connectivity analysis

We now investigate the impact of changing D on the neuron's potential to connect to other neurons. Previous studies established that the arbor's physical structure is sufficient for describing the connection process, with chemical steering

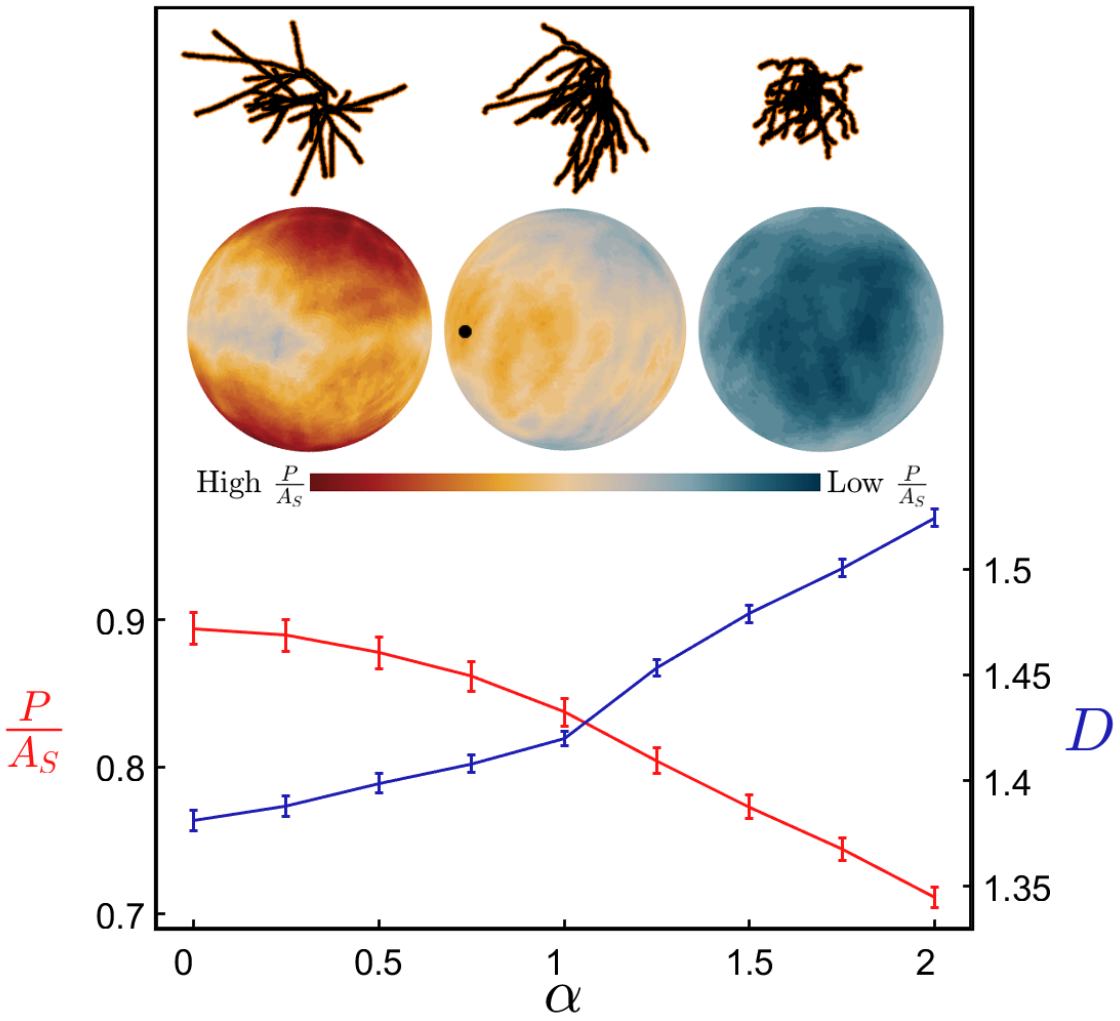

FIGURE 2.3. Adjusting the morphology of neurons by varying the weave. P/A_s (the arbor's profile, P, averaged over all orientations and normalized to the arbor's surface area, A_s) (red) and fractal dimension D (blue) plotted against the weave angle manipulation factor α. The data shown here for both the red and blue lines are averaged over all basal arbors and their variations are represented by the shown standard errors from the mean. The upper insets show an example neuron for $\alpha = 0.25$ (left), 1 (middle) and 1.75 (right). The lower insets show the equivalent profile spheres, where the black dot represents the orientation with maximal P/A_s for the middle neuron and the bar indicates the colors ranging from high to low P/A_s values.

playing a relatively minor role [77]. In particular, the arbor's dendritic density

[78, 79, 80, 81] and resulting physical profile [70] are powerful indicators of its

potential to connect to other neurons. When viewed from a particular orientation, we define the arbor's profile P as the total projected area of its branches. Large profiles will therefore result in the increased exposure of synapses, which are responsible for receiving signals from other neurons. When calculating the profile from the dendrite images, we incorporate an extra layer (orange in Fig. 2.3 upper inset, Fig. 2.9) surrounding the branches (black) to account for outgrowth of dendritic spines - small protrusions which contain the majority of the dendrite synapses (methods Section 2.5.4). For each arbor shown in Fig. 2.3, P is therefore the sum of the projected black and orange areas. We then normalize this projected surface area of the dendrites using their total surface area, A_s, to accommodate for the range in neuron sizes and associated surface areas. (Because the orange areas are included in P but not in A_s, note that $P/A_s > 1$ is possible). The current study adopts the general approach of averaging P/A_s across all orientations of the dendritic arbor to allow for the fact that axons originating from within the CA1 region connect to the dendritic arbors from every direction [71]. The profile variation with orientation can be visualized by projecting the P/A_s values obtained for each direction onto a spherical surface. For the profile spheres included in Fig. 2.3, the neurons are viewed from a common direction which corresponds to the middle point on the sphere's surface. For the natural neuron, the orientation for which P/A_s peaks is marked by the black dot. Typically, this peak occurs in the direction that the Schaffer collateral axons enter from the CA2 region [69] and so maximizes the connectivity of our natural neurons to those incoming axons.

The inverse relationship between P/A_s and D observed for the weave in Fig. 2.3 also occurs when adjusting the fork angle. Its physical origin can be traced to the increased fine structure of high D neurons causing branches to block each

other and so reduce the overall profile. Including this blocking effect is important for capturing the neuron's connectivity because multiple connections of an axon to the same dendritic arbor are known to generate redundancies [70]. Therefore, if a straight axon connected to an exposed branch, subsequent connections to blocked branches wouldn't increase the connectivity and should be excluded. Fig. 2.4a summarizes this blocking effect by plotting P/A_s directly against D for arbors that have had their ϕ and θ values manipulated independently. Fig. 2.4b demonstrates that this blocking reduction in P/A_s is also seen for H-Trees (which have had their weaves similarly adjusted - see methods Section 2.5.4 and Fig. 2.9), highlighting that the blocking dependence on D is general to fractals. Fig. 2.4c, d explore another well-known fractal effect that high D fractals increase the ratio of the object's surface area A_s to its bounding area A_b (i.e. the surface area of the volume containing the arbor, as quantified by its convex hull - see methods Section 2.5.2). Fig. 2.4e,f combine the 'increased surface area effect' seen in Fig. 2.4c,d with the 'blocking area effect' seen in Fig. 2.4a,b by plotting P/A_b (i.e. the multiplication of P/A_s and A_s/A_b) against D. In effect, P/A_b quantifies the large surface area of the arbor while accounting for the fact that some of this area will be blocked and therefore excluded from the profile P. Normalizing P using A_b serves the additional purpose of measuring the arbor's potential connectivity in a way that is independent of its size. Accordingly, P/A_b serves as a connectivity density and is an effective measure of the neurons' capacity to form a network.

The clear rise in P/A_b revealed by Figs. 2.4e, f highlights the functional advantage offered by high D branches - incoming axons will experience the dendritic arbor's large connectivity density. Note that the plotted connectivity density is for individual neurons. Because of the inter-penetrating character of

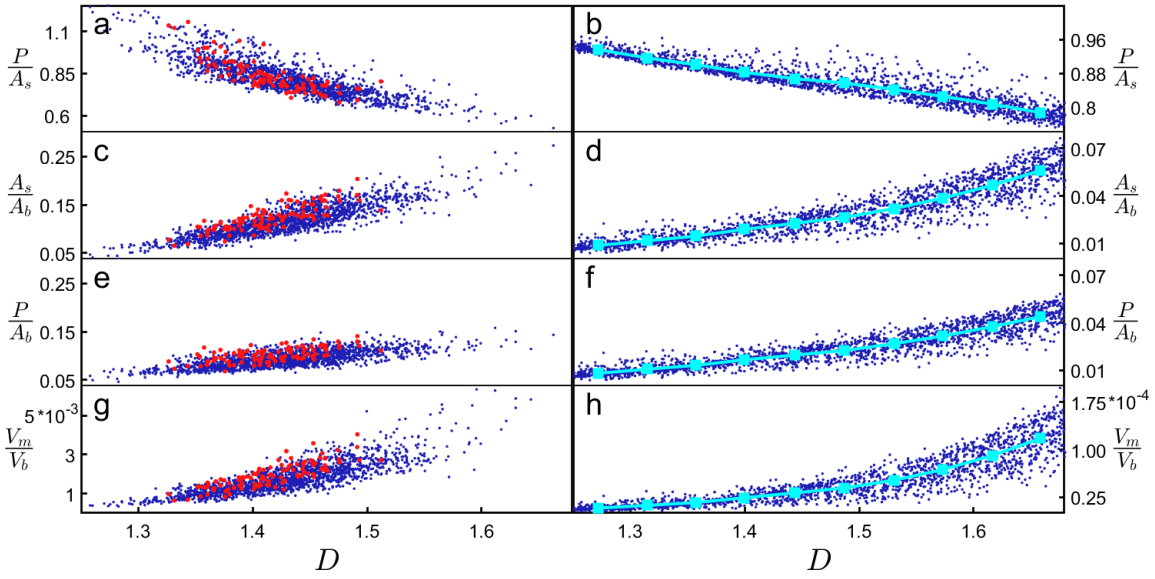

FIGURE 2.4. Physical dependency on D. Dependencies of various parameters (see text for parameter definitions) on D for neurons (left column) and H-Trees (right column). Red data are for unmanipulated basal arbors while the blue data are for basal arbors where either their ϕ or θ values are manipulated. H-Trees with straight and with weaving branches are included. The connected cyan data points are average values of the H-Tree data.

dendritic arbors from neighboring neurons, the collective connectivity density will be even larger due to their combined profiles. If this functionality was the sole driver of neuron morphology, then all neurons would therefore exploit high D values approaching 3. Yet, both the apical and basal dendrites cluster around relatively low values of D $\sim$ 1.41 suggesting that there are additional, negative consequences of increasing D. In Figs. 2.4g, h, we plot the ratio of the volume occupied by the branches V_m to the neuron's bounding volume V_b (i.e. the arbor's convex hull volume). For high D dendrites, the tighter weave angles along with forking angles that bring branches closer together result in more densely packed structures. This produces the observed rise of V_m/V_b. Assuming constant tissue density, V_m is proportional to the neuronal mass. The rise in V_m/V_b therefore quantifies the increase in mass density and associated 'building' costs of high

D neurons. Aside from this, there is also an 'operational' cost. It is well-known from allometric scaling relationships that metabolic costs generally increase with mass[82, 83]. Specifically, previous research proposed that the amount of ATP expended by neurons increases with A_s [38, 70]. Revisiting Fig. 2.4c and Fig. 2.4a, A_s/A_b therefore charts how the normalized energy cost increases with D, and P/A_s measures the neuron connectivity relative to this cost.

2.4. Discussion

Taken together, Figs. 2.4a-h summarize the competing consequences of increasing D for both the neurons and H-Trees: the benefits of enhanced connectivity density increase (Fig. 2.4e, f), but so does the cost of building (Fig. 2.4g, h) and operating (Fig. 2.4c, d) the branches. The distinct forms of these three factors are highlighted for the H-Trees by plotting their average values against D (cyan). Allowing for scatter, the neurons share the same forms as the H-Trees. By establishing these shared forms, the H-Trees serve as artificial neurons. Neuron behavior can then be observed for D values beyond their naturally occurring ranges, allowing a clear picture of their tolerances for the above factors. The sharp increase in building cost and high operating cost observed at high D values explain why the natural neurons (red) don't exceed D = 1.51. Nor do they occur below D = 1.33 because of the low connectivity. This balance of factors is likely optimized at their most prevalent D value (D = 1.41 in Fig. 2.1d). This value agrees with the scaling exponent of 1.38 from a previous study of pyramidal arbors [70] which limited its focus to the optimization condition. Based on our analysis spanning a wide range of D, we hypothesize that different neuron types have different D values depending on the relative importance of connectivity

and cost. Neurons with a greater need for connectivity will optimize around higher D. For example, human Purkinje cells are characterized by D $\sim$ 1.8 [84]. We also hypothesize that pathological states of neurons, for example those with Alzheimer's disease, might affect the fractal optimization and explain previous observations of changes in the neurons' scaling behavior [85].

Fractal analyses of a wide variety of neurons indicate that their D values don't generally exceed D = 2, presumably because of the excessive costs of higher D fractals. For comparison, we note that a sphere (D = 3) achieves much higher connectivity ($P/A_b = 0.25$ compared to the D = 1.4 neuron's 0.1). However, the sphere suffers from large mass density ($V_m/V_b = 1$ compared to 10^{-3}) and higher operational costs ($A_s/A_b = 1$ compared to 0.1), suggesting that neurons adopt fractal rather than Euclidean geometry in part because the mass and operational costs of the latter are too high. We note that neurons' restriction to lower D values doesn't apply to fractal electrodes designed to stimulate neurons [14, 23, 86]. These artificial neurons require large profiles to physically connect with their natural counterparts. However, unlike natural neurons, the large A_s associated with high D electrodes reduces the operation costs because their higher electrical capacitances lead to larger stimulating electric fields [14, 23]. Thus, fractal electrodes approaching D = 3 might be expected to efficiently connect to and stimulate neurons. That said, there might be advantages of matching the electrode's D value to that of the neuron. This will allow the neuron to maintain its natural weave and forking behavior as it attaches to and grows along the electrode branches, so maintaining the neuron's proximity to the stimulating field.

Previous studies of connectivity and dendritic cost focused on component parameters of the neuron geometry (such as tortuosity, branch length and scaling

analysis of small parts of the arbor) [70, 78]. We have shown that our 'effective' D incorporates these parameters in a holistic approach that directly reflects the neuron's fractal-like geometry. For example, our discovery that the neurons' weave (generated by variations in θ) is an important factor in determining D provides a link between D and tortuosity. However, whereas tortuosity quantifies the weave of an individual branch measured at a specific size scale, D captures a more comprehensive picture by accounting for the weave's tortuosity across multiples scales. Because D measures across multiple branches within the arbor it is also sensitive to ϕ and L. Accordingly, by incorporating θ, ϕ, and L, D is the most appropriate parameter for charting the connectivity versus cost optimization. As an indicator of this central role, the forms of Fig. 2.4 are highly sensitive to the intricacies of the neuron structure. This further highlights the power of our approach - the use of D facilitates direct comparisons of the favorable functionalities generated by diverse structures. Here, we compared our neurons to distorted versions, to H-Trees, to fractal electrodes, and to Euclidean shapes, but this approach could readily be extended to many natural fractals. The fact that the H-Trees and neurons exploit the same D-dependent optimization process (Fig. 2.4) raises the question of why the two structures use different branch length distributions (Fig. 2.2) to generate their scaling behavior. The answer lies in the neuron's need to minimize signal transport times within the arbor [87]. This is achieved with short branches close to the soma (Fig. 2.8) while the H-Tree suffers from longer branches. Remarkably, Fig. 2.4 shows that the D-dependent behavior impacts neuron functionality even though it occurs over only a limited range of branch sizes. Many physical fractals are also limited [26], demonstrating the effectiveness of fractal-like behavior for optimizing essential processes ranging from

oxygen transfer by our lungs, to light collection by trees, to neuron connections throughout the body.

2.5. Methods

2.5.1. Rodents

Rat pups were bred and housed with their mother in cages with wood chips and ad libitum food and water in an environmentally controlled room. All procedures pertaining to the use of live rats were conducted in compliance with all relevant ethical regulations for animal testing and research. All procedures were approved by the University of Canterbury Animal Ethics Committee, 2008-05R.

2.5.2. Image acquisition and model reconstruction

Thirty-three adult PVGc male hooded rats (13 – 16 months old) were given an overdose of sodium pentobarbital. The brains were removed fresh without perfusion, rinsed with Milli-Q water, and a 4mm block containing the hippocampus was cut in the coronal plane using a brain matrix (Ted Pella, Kitchener, Canada). These tissue blocks were processed with a metallic Golgi-Cox stain, which stains 1% to 5% of neurons so that their cell bodies and dendritic trees can be visualized. Thick $200\mu m$ coronal brain sections spanning the bilateral dorsal hippocampus were taken using a microtome. A standard microscope was used to locate isolated neurons in the dorsal CA1 subfield (Fig. 2.5a). These large pyramidal neurons consist of a long apical dendritic tree protruding from the apex of the soma and a shorter basal dendritic tree protruding from the other end (Fig. 2.1b). Only some intact whole neurons were located, whereas many intact basal-only or apical-only dendritic trees were located. A Leica laser

scanning confocal microscope was used to collect high-resolution image stacks for each of these neuronal processes (Fig. 2.5b). The image stacks were captured using a 20x glycerol objective lens with a 0.7 numerical aperture, providing an x and y resolution of $0.4\mu m$. The step size (z distance between image stacks) was $2\mu m$. Dendritic arbors were manually traced through the image stacks using Neurolucida[72] (MicroBrightField Bioscience) to create three-dimensional models (Fig. 2.1b and Fig. 2.5c). The data was then exported to the Wavefront .obj format and the cell soma removed.

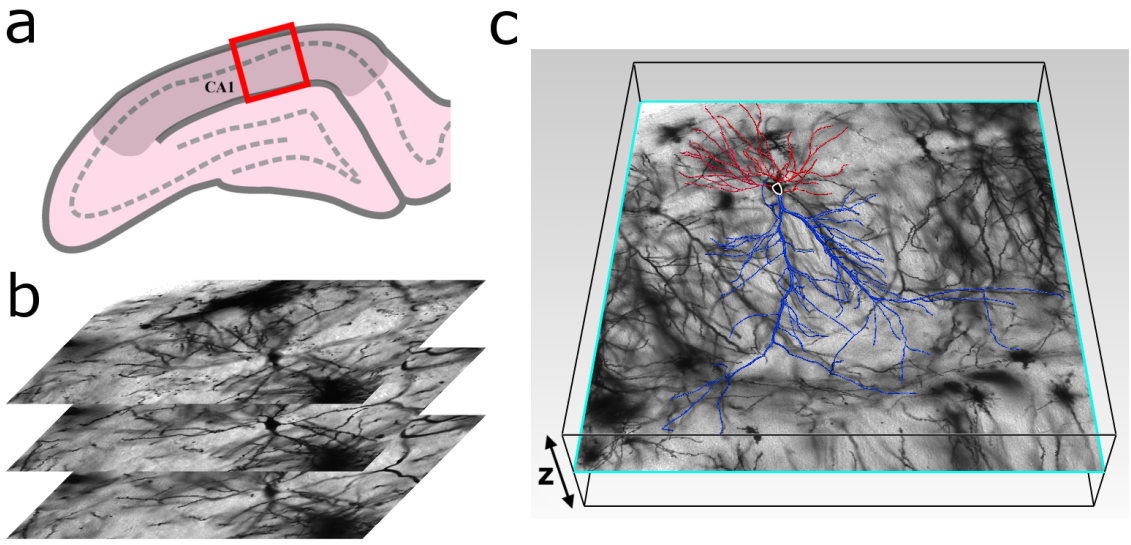

FIGURE 2.5. Image acquisition. (a) Schematic diagram of a coronal slice through the hippocampus at Bregma -4.52mm showing the collection region (red box) within hippocampal CA1 (darkened area); the somata layer is denoted by the dashed line. (b) Confocal micrographs of Golgi-Cox stained cells. Three 774 by $774\mu m$ cross-sections separated by $2\mu m$ in the z-direction are shown. (c) A model showing a neuron's soma (outlined in white) as well as its basal (red) and apical (blue) dendritic arbors superimposed on the original micrograph.

The three-dimensional models are composed of a set of connected hollow cylinders (segments) which form the branches of the arbors. Each cylinder is constructed using two sets of rings of 16 points (vertices) and 32 connecting

triangles (faces). At branch endings, the final segment has 14 faces that form an end cap. Connecting branches start new segments at the same location as the last set of 16 vertices from the previous branch. For the apical arbors, one branch extends from the apex of the soma and all other branches connect either directly or indirectly to it. For the basal arbors, multiple initial branches extend from the soma, each with its own set of connecting branches.

In order to perform the box-counting and profile analyses, the Wavefront files were converted to voxel data using Matlab software. The voxelization was performed at a resolution of 4 voxels/μm for box counting and 1 voxel/μm for the profile calculation. In both cases, the models were voxelized exactly, meaning that if any part of the polygonal model fell inside a voxel, the voxel was added to the list of x; y; z coordinates.

We used rotation quaternions [88] to adjust the weave angles to the modified values multiplied by the pre-factor α. We started with the angles furthest from the soma and, working inwards, adjusted angles one at a time until all of the angles had acquired their new values. When an angle was adjusted, the entire connected section of the branch between that angle and the terminal endcaps was rotated too. This rotation occurred in the plane of the two vectors that define that angle. We created three sets of arbor models modified by the multiplier α for values between 0 and 2, incremented by 0.25. In one set θ was modified, in another ϕ was modified, and in another both were modified simultaneously. The qualitative results shown in Fig. 2.4 were the same for all three sets.

When calculating the surface area, A_s, of the models, the precision was raised by increasing the number of faces in a neuron's construction four-fold by converting each triangle into four sub-triangles using a midpoint method (Fig.

2.6b). We then summed the areas of all the triangles in the model, excluding the faces where all three vertices resided inside another segment. The bounding area, A_b, and bounding volume, V_b, were calculated using the convex hull method [89] on the vertices of the Wavefront object. A_b is the sum of the areas of all triangles composing the convex hull that encloses the vertices, whereas V_b is the volume enclosed within those triangles.

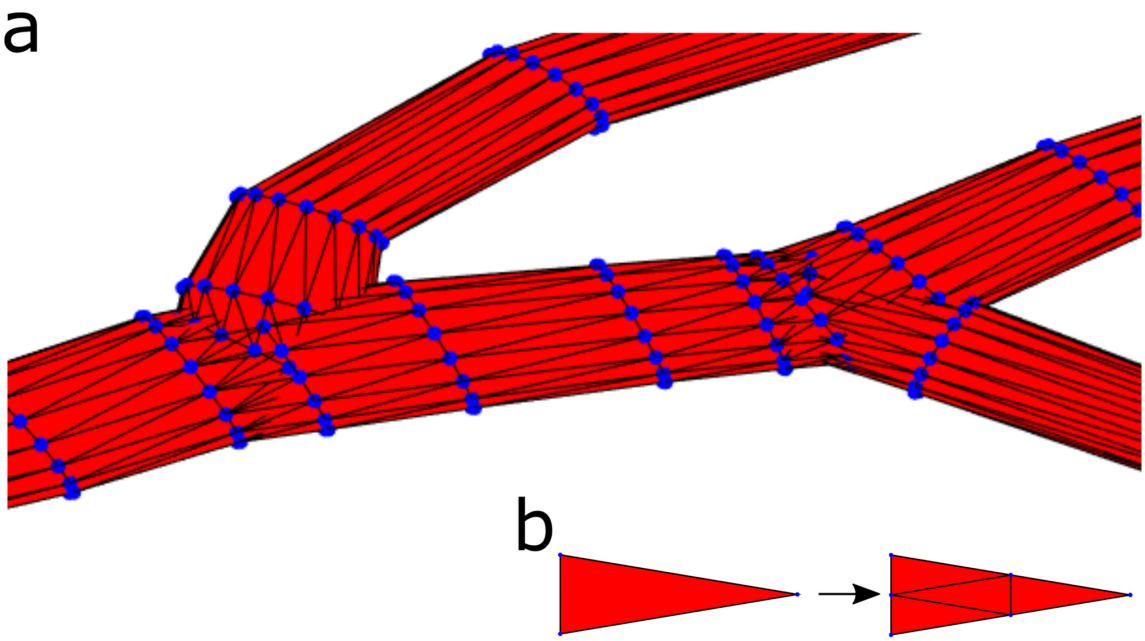

FIGURE 2.6. Model reconstruction. (a) A close-up image of dendritic branches. The Wavefront object files (.obj) consist of cylinders constructed from vertices (blue) and triangular faces (red). (b) The triangular faces are increased 4-fold for the surface area calculations by finding the midpoints between connected vertices in a face and creating new vertices at those points. Then 4 new faces are created that connect the new vertices as shown.

2.5.3. Box counting analysis

The box-counting method used to analyze the fractal characteristics of the neurons is shown in Fig. 2.7. Using Matlab software, the voxelized dentritic arbor was inserted into the three-dimensional array of boxes and the number of boxes

N_{box} occupied by the neuron were counted for different sizes of boxes, L_{box}, and this was normalized to L_{max}, the largest branch size of the arbor. The largest box size was set to the size of the longest side length of the arbor's bounding box and the smallest box size to the voxel pixelization ($0.25\mu m$). The insets show example schematics of the filled boxes for large and small L_{box} values. We performed a modified 'sliding' box count [4] in which the boxes slid in every coordinate direction simultaneously in $0.25\mu m$ steps and the minimum count was selected.

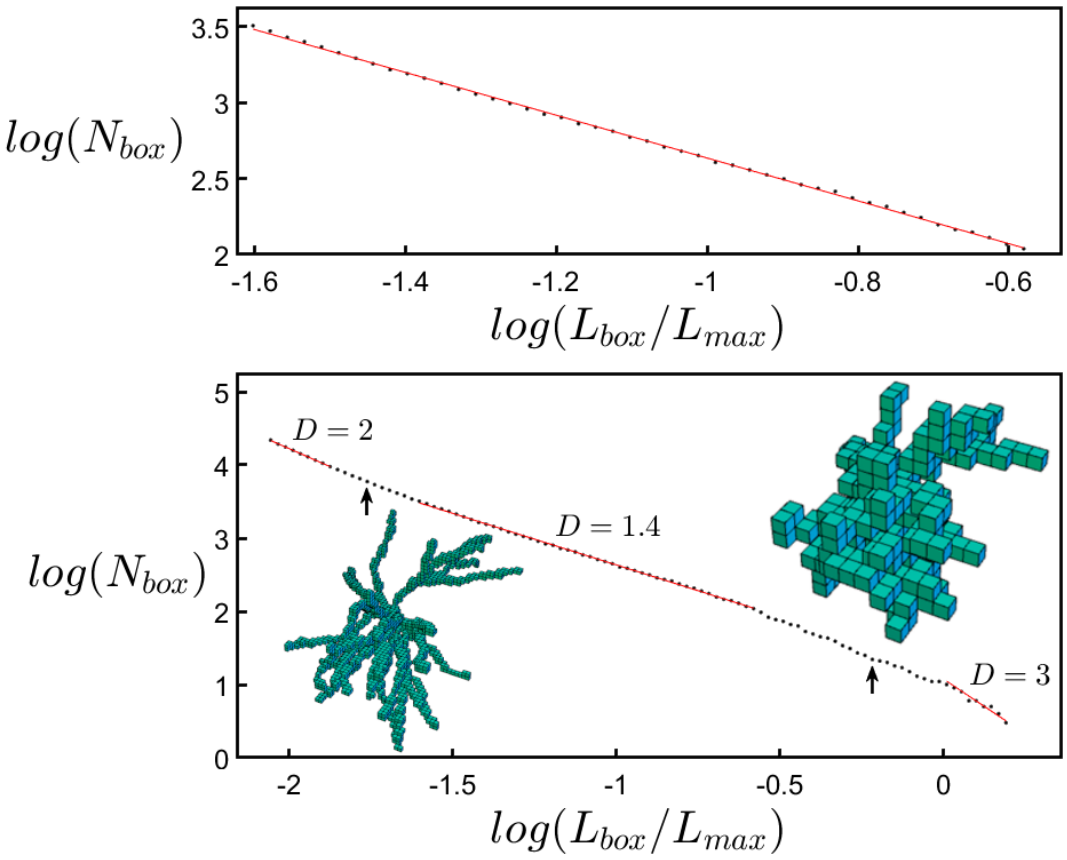

FIGURE 2.7. Scaling plot. $\log(N_{box})$ plotted against $\log(L_{box}/L_{max})$ for an example dendritic arbor, where N_{box} is the number of occupied boxes and L_{box} is the box length. The top graph shows a zoom-in on the fractal-like scaling region of the bottom graph. The insets show occupied boxes at small and large box scales. See the text for explanations of the arrows.

Fractal scaling, $N_{box} \sim L_{box}^{-D}$, appears as a straight line in the log-log plot. The range of L_{box}/L_{max} values for which fractal behavior might be observed lies between the vertical arrows. For large boxes to the right of the right arrow, there are too few boxes (less than five along each side of the bounding box) to reveal the fractal behavior. Consequently, all of the boxes become filled and so the analysis interprets the neuron as being three-dimensional and the gradient eventually shifts to a value of three. To the left of the left arrow (corresponding to $2\mu m$), the box sizes approach the diameters of the branches and so the analysis starts to pick up the two-dimensional character of the branches' surface and the gradient shifts to a value of two.

Between the arrows, a straight line was fitted for all sets of points ranging over at least one order of magnitude. The fit that maximized R^2 was chosen to measure the D value (the slope of the line). When looking at the residuals of this regression analysis, their behavior confirmed that the fit range was appropriate. We note that applying the angle multiplier to the neurons didn't reduce the quality of the fit nor the scaling range of fractal behavior.

2.5.4. Profile analysis

An arbor's physical profile [70] has been shown to be intrinsically related to its ability to connect with other neurons. We developed MATLAB software that measures the profile of the dendritic arbor using a list of cartesian points in space that denote the locations occupied by the dendrites. In our calculations, we used the voxelized list of points generated using the Wavefront file of the dendritic arbor. To allow the dendritic spines to contribute to the calculation of an arbor's profile, we uniformly expanded the voxelized arbor by $2\mu m$ in every direction. The

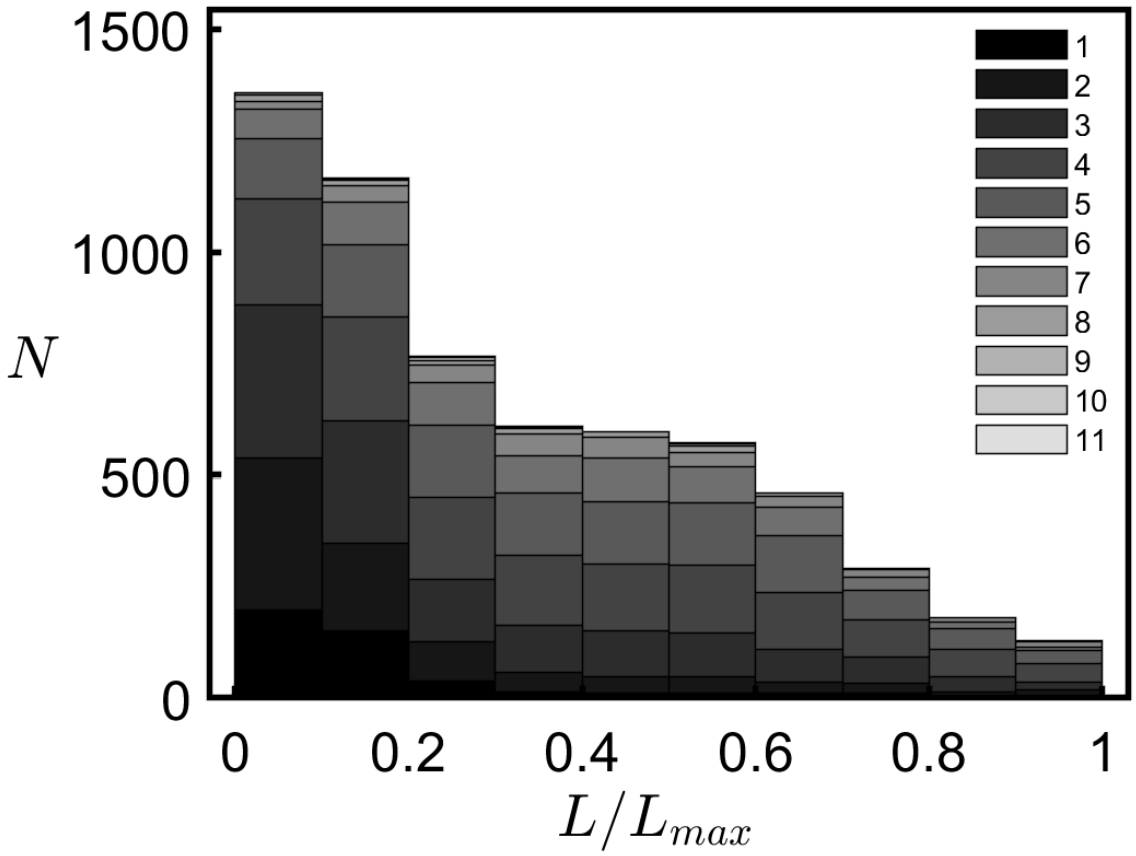

FIGURE 2.8. Branch iteration distribution. Histogram of the number N of normalized branch lengths (L/L_{max}) across all basal arbors used in the study. The shade of gray in each box represents the branch iteration m, with the darker shades corresponding to the lower iterations closer to the somas.

orange region around the black dendrites seen in Fig. 2.9a, b represents the space around the dendrites in which a spine could grow in order to form a synapse with an axon passing through the arbor.

This expanded list of points was then orthographically projected onto the x-y plane. After projection, the points were rounded and any duplicate points occupying the same location were removed. Because the location of the points has been rounded, each point represents a $1\mu m$ area and the total area occupied by this projection can be measured by counting the number of remaining points

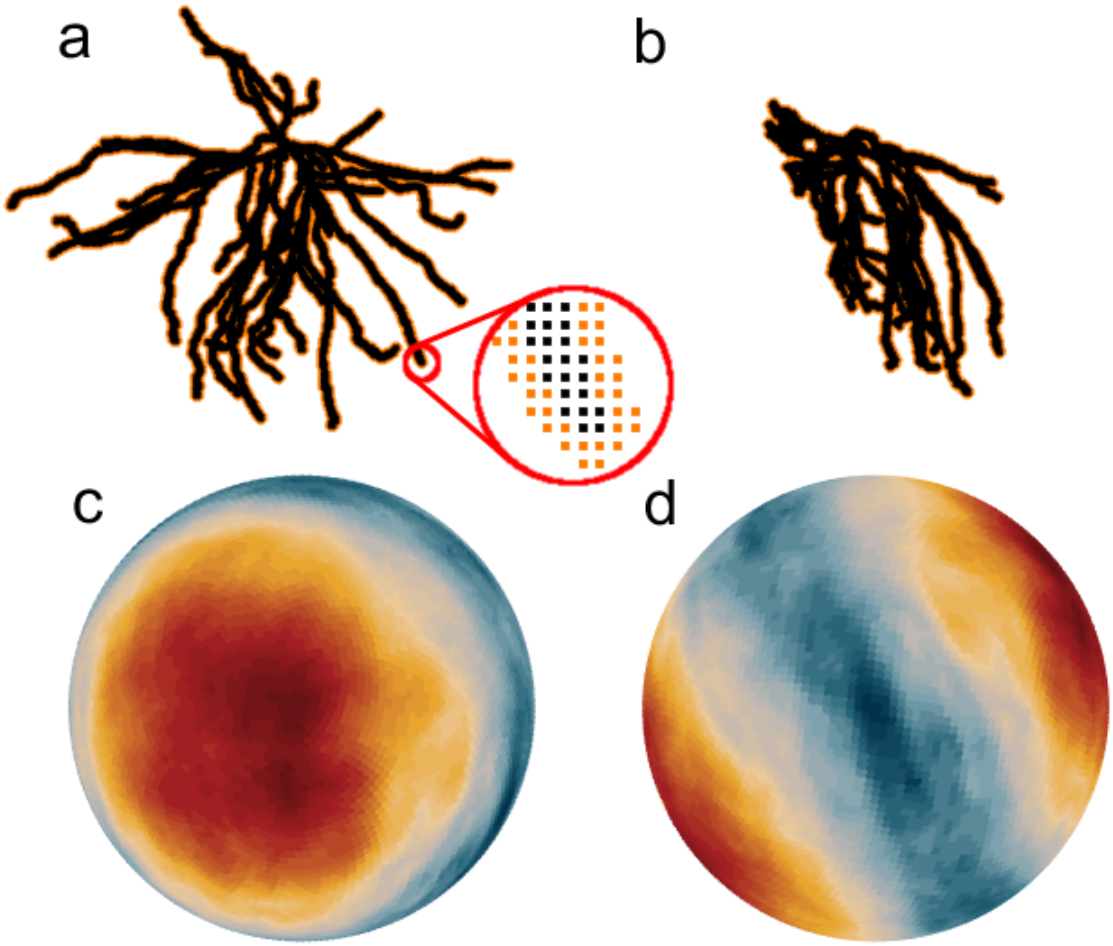

FIGURE 2.9. Profile calculation. (a) An arbor viewed from the direction for which P/A_s peaks. The zoom-in shows a black branch surrounded by the orange region of spines. (b) The same arbor viewed from a different direction. (c) and (d) show the equivalent profile spheres. The middle point on the spheres surface shown in (c) and (d) corresponds to the profile of the arbor as seen from the viewpoints shown in (a) and (b), respectively.

constituting the projection. The area of this projection divided by the bounding area of the neuron is then proportional to the probability of connection with an axon travelling parallel to the z-direction and passing through the dendritic arbor. However, because the axons that pass through the arbors of our CA1 neurons can arrive from any direction [69, 71], we calculated the average profile of each neuron's arbor as though it were viewed from any point on the surface of a sphere

containing the neuron's arbor with its origin at the neuron's center of mass. To accomplish this, we defined a set of polar and azimuthal angles that corresponded to the viewpoints on the sphere. By rotating the expanded list of points by these angles and then projecting the result onto the x-y plane, we obtained what the arbor would look like if seen from the given viewpoint. We calculated the average profile by defining a set of uniformly distributed points on the circumscribing sphere and then averaging the area of the projections corresponding with each viewpoint. Because it is impossible to distribute a general number of equidistant points on the surface of a sphere [90], we defined our set of points using the Fibonacci lattice, a commonly used and computationally efficient method for distributing the points [91].

The colored spheres (comprised of 10001 points) in Fig. 2.3 and Fig. 2.9 give a visual representation of the variation in profile with respect to the viewpoint. The average profile data used in Fig. 2.4 was calculated using only 201 viewpoints, which is sufficient for convergence - the average P for 201 viewpoints deviates by less than 1% from the value achieved when approaching infinite viewpoints.

2.5.5. H-Tree generation

Fig. 2.10 shows examples of the H-Tree models used to generate the data of Fig. 2.4b, d, f. Whereas these H-Trees extend into three-dimensional space (middle and bottom row), we also include two-dimensional H-Trees (top row) for visual comparison. Using Mathematica software, the D values of these straight branched models were generated using the branch scaling relationship

$$L_i = L_1/2^{(i-1)/D} \tag{2.1}$$

where L_i is the branch length of the i^{th} iteration. The H-Trees used to generate the data seen in Fig. 2.4 had 12 iterations of branches and the length of the first branch, L_1, of any given H-Tree was chosen such that the total length of all the branches was constant across all D values. For comparison of the H-Trees with the basal arbors in Fig. 2.4, the number of branch iterations in the H-Tree was chosen to be close to the largest number of iterations observed for the basal arbors (11). The D values of H-Trees in the bottom row are determined by a combination of the length scaling between branch iterations and the weave of the branches. The distribution of weave angles was generated using a fractional Gaussian noise process, which is known to be self-similar, and the resulting D values were measured using the box-counting algorithm. The width of the weave angle distribution was specified before generating the H-Tree, allowing for fine control over the tortuosity of its branches. By using four different weave angle distribution widths and creating H-Trees with a multitude of D values, we demonstrated the robustness of the relationship between the D value and our various functional parameters shown in Fig. 2.4.

A complete description of H-tree properties are included in Appendix A.1.

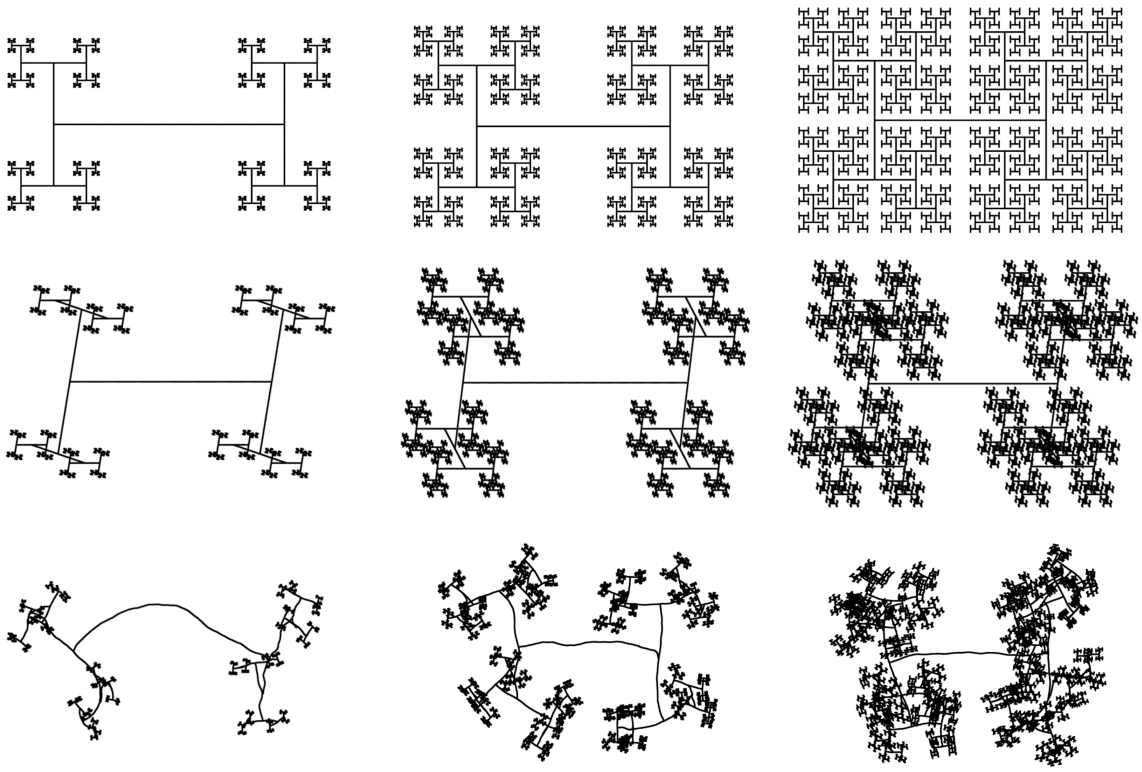

FIGURE 2.10. H-Tree models. A visual comparison of H-Tree models extending into two-dimensional (top row) and three-dimensional (middle row) spaces for D = 1.1 (left), D = 1.5 (middle) and D = 1.9 (right). Their branches are straight, and their D values are set by the scaling relationship between branch lengths L at subsequent iterations i. For the bottom row of H-Trees, the branch angles have been modified to introduce a weave into the branches.

CHAPTER III

APPLICATIONS OF THE FRACTAL FRAMEWORK

In this chapter we will investigate the fundamental behavior of neurons as they establish connectivity with an electrode. One might assume that since neurons are 3-dimensional fractals that a 3-dimensional fractal electrode would perform the best. However, electrodes have two critical differences when compared to neurons. First, we showed in Chapter 2 that neuron morphology is highly impacted by mass. However, there is no such cost for a microfabricated electrode, where adding additional material is not inherently detrimental. Second, in contrast to neurons, an increase in the surface area benefits an electrode as it increases the capacitance which stimulates neurons. We will compare 3 promising electrode designs for their capacitance, connectivity, bio-compatibility, and ease of fabrication.

First, we want to revisit the H-Tree models from Chapter 2. We consider those models generated without adding a weave so that we can exactly calculate all the neuron's costs (Appendix A.1). We use the generative D value defined in Equation 1.1 & 2.1 for simplicity. First we show in more exact detail what we demonstrated previously, that balancing costs and connectivity alone is sufficient to explain why a neuron chooses an intermediate D value. We then do the same for a case where axons only approach from a single direction and find that higher D values are preferred, which is consistent with intuition and previous observations. For example, Purkinje neurons have high D values and parallel fibers that come from a single direction [84, 92, 93]. We then compare ED2 and ED3 H-Tree models. We smoothly transition between those two extreme conditions and

apply the findings to our understanding of neurons. Then we predict the relative number of axons connecting to basal and apical dendrites from different directions.

We use a cost-benefit analysis to justify the types of dendritic morphologies observed. We define two generic functions G and K, which represent the benefits and costs to the neuron respectively. The ratio G/K then motivates more likely neuron geometries. We've already described costs to the neuron in Chapters 1 & 2, but it is worth identifying them here again (summarized in Table 3.1). Because we want to analyze the morphology of dendrites, we will restrict ourselves to the dendritic costs.

For signaling energy expenditures we identified that surface area, A_s, is the primary geometric cost [70]. Non-signalling geometric costs also include the surface area, A_s, the total length, L_t, the segment width, W, a space occupancy cost, A_b, and a mass cost. We use the volume of the mass, V_m, as a substitute for a traditional mass by assuming a constant density throughout the dendritic structure.

Parameter (Symbol)	Neuron	Electrode
Profile (P,$\tilde{P}$,P_{max})	Benefit	Benefit
Surface Area (A_s)	Cost	Benefit
Occupying Space (A_b,V_b)	Cost	Cost
Total Length (L_t)	Cost	NA
Volume of Mass (V_m)	Cost	Neither
Height	NA	Benefit & Cost
Footprint (A_f)	NA	Cost

TABLE 3.1. Summary table of parameters. Parameters used in this chapter are listed and identified as either a benefit, cost, or not applicable (NA) as they apply to neurons and electrodes. P is the average profile, $\tilde{P}$ the median profile, and P_{max} the single largest profile from all viewpoints. The bounding area, A_b, and bounding volume, V_b, both measure occupying space, but we use A_b for consistency with Chapter 2. See Appendix A for definitions.

3.1. Neurons modeled as H-Trees

Using H-Trees as model neurons, we investigate the D dependence of ED3 (Fig. 3.1a) and ED2 (Fig. 3.1b) models in response to incoming axons. By fixing the total length, L_t, and the width, W, we also fix the volume of mass, V_m, and the surface area, A_s. Together these parameters (L_t, W, V_m, A_s) comprise the constant costs, C, of an H-Tree model. The space occupied, A_b, is then the only cost that is free to vary. As done in Chapter 2, we will consider the profile averaged over all viewpoints, P, as a measure of connectivity, which a neuron seeks to increase (see Section 2.5.4). We assume G and K monotonically increase with increasing P and A_b respectively.

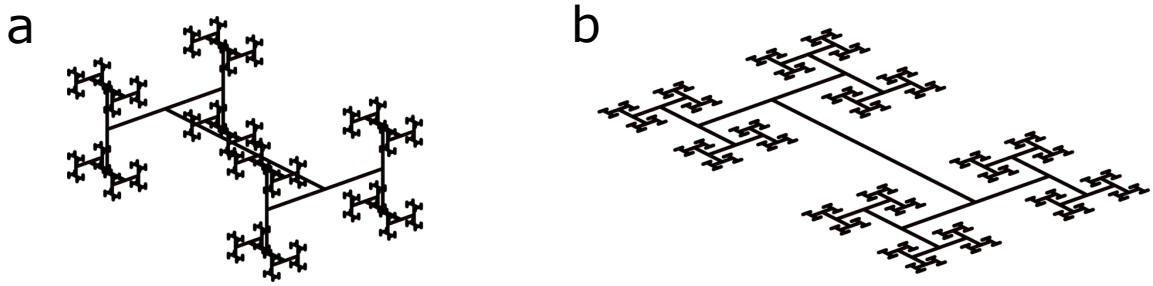

FIGURE 3.1. Two examples of H-Tree models. Both models have a fixed total length and branch width. This correspondingly fixes the surface area and volume of mass. Each branch length is reduced at every bifurcation according to a fractal of D=1.4 and 9 iterations (a) ED3 model (b) ED2 model (see Section 2.5.5 & A.1 for construction).

3.1.1. Uniform axonal inputs

First, we assume that axons approach uniformly from every direction. We apply the same procedure for calculating profile outlined in Section 2.5.4 (Fig. 2.9). For both models P decreases with D, and thus G(P) also decreases with D (Fig. 3.2). A_b also decreases with D. Importantly, the rate at which A_b decreases

is much faster at low D values, and flattens out at higher D values. P on the other hand, decreases at a much more consistent rate with varying D. Therefore it is possible that to maximize the benefit to cost ratio an intermediate D value is preferred (Fig. 3.3a). This preference for an intermediate D value is the behavior seen in many neuron types (e.g. CA1 hippocampal neurons) [94].

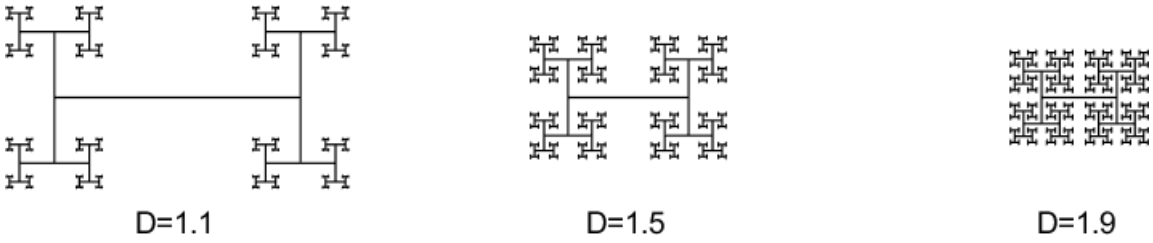

FIGURE 3.2. H-Tree bounding area variation with D. H-Trees with fixed total length have a decreasing bounding area with increasing D.

3.1.2. Unidirectional axonal inputs

Next, we consider the ED2 model interacting with axons that bisect the model plane (e.g. axons interacting with Purkinje cells) [92]. In this case the profile will take on its maximal value, $P_{max} = W \times L_t$, a constant. Therefore, $G(P_{max})$ is also a constant. Our cost function, K has constant input, C, and a variable input, A_b. A_b decreases with D and therefore so does $K(C, A_b)$. Consequently our cost-benefit analysis shows that the ratio G/K then increases with D. This result suggests that any ED2 neuron with inputs from a single direction would choose the highest D value possible. Again, Purkinje cells have relatively high D values which is consistent with this result [84]. Fig. 3.3b demonstrates this behavior with example functions for G and K.

If we would have considered a ED3 model the same logic would hold.

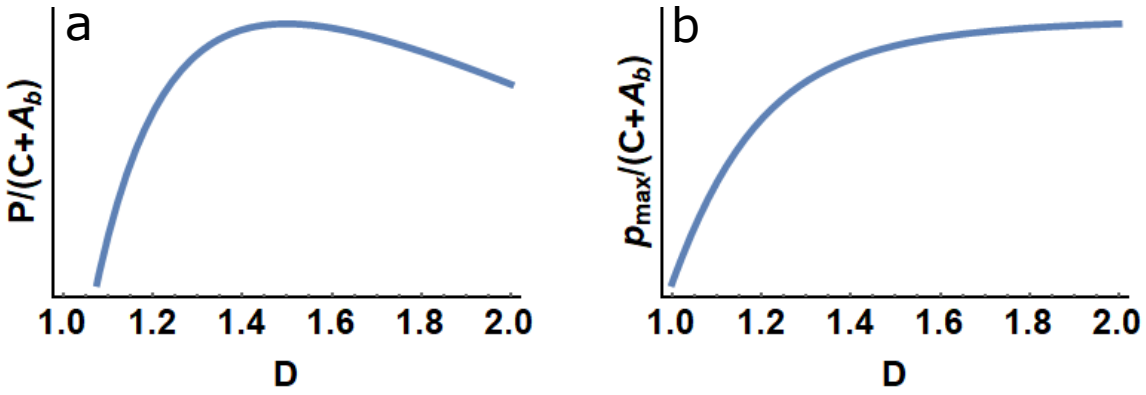

FIGURE 3.3. Cost-Benefit analysis behavior with D. (a) A combination of decreasing P, A_b, and constant costs, C, results in a maximal benefit to cost ratio if C is on the order of A_b. Profile, P, is fitted data of a profile measurement. Here we guess $G = P$ and $K = C + A_b$, where C accounts for the constant costs. (b) When the profile is set to its maximum value ($P \rightarrow P_{max}$, a constant) the benefit to cost ratio monotonically increases with D because K monotonically increases with A_b.

3.1.3. A comparison between ED2 and ED3 H-Tree models

In the previous two sections we asked: Given a model (ED2 or ED3) and a condition (uniform or unidirectional), what D value maximizes the benefit to cost ratio? We identified that the D value behavior matches our expectations. An intermediate D value could be preferred when axons come from many directions, and a high D value would be preferred when axons come from a single direction. We now ask a follow up question. If we have a condition, can we predict the model?

One might reasonably assume based off of observation that an ED3 model would perform better when axons approach from many directions, and an ED2 model would perform better when axons approach from a single direction. That intuition is verified when axons approach from a single direction, the maximum profile is always higher and the bounding area is always lower for the ED2 model.

Therefore $G(P_{max})/K(A_b)$ is always greater for any given D value. However, when axons approach from many uniform directions we find the exact same result, the ED2 model performs better than the ED3 at every D value. Again, this occurs because the measured average profile is always higher and the bounding area is always lower for the ED2 model.

In order to understand these results, it is useful to create H-Trees that vary smoothly between the exact ED2 and ED3 models. In Chapter 2 we briefly introduced, but did not use the angle ψ, which measures the next segment's rotation along the long axis of the current segment. Every new segment had a single ψ associated with it. At a bifurcation one segment splits into two new segments (the start of two new branches). Each of those new segments has a branching angle, ϕ, and a ψ. For instance, if we fix both branching angles ϕ_1 and ϕ_2 (shorthand $\phi_{1,2}$) to be 90° and opposing each other, then rotating about $\psi_{1,2}$ is akin to spinning a two blade propeller with each blade the start of a new branch (Fig. 3.4e).

For H-Trees, the ED2 and ED3 models do not weave and have $\phi = 90°$ everywhere. Both have $\psi = 0°$ associated with every new segment within a branch (for the weave - when only 1 new segment proceeds another). The only difference is that the ED2 model has $\psi_{1,2} = (0°, 180°)$ and the ED3 model has $\psi_{1,2} = (90°, 270°)$ for every pair of segments at the start of a new branch. For the H-Trees described in this dissertation $\psi_2 = \psi_1 + 180°$ always.

If we vary the $\psi_{1,2}$ angle pair, then we can smoothly transition between an ED2 and ED3 model (Fig. 3.4). When ψ_1 is between 0° and 15°, we define this as the semi-ED2 region, for its relatively planar structure. In the semi-ED2 region there is at least one viewpoint at which every segment of every branch is not

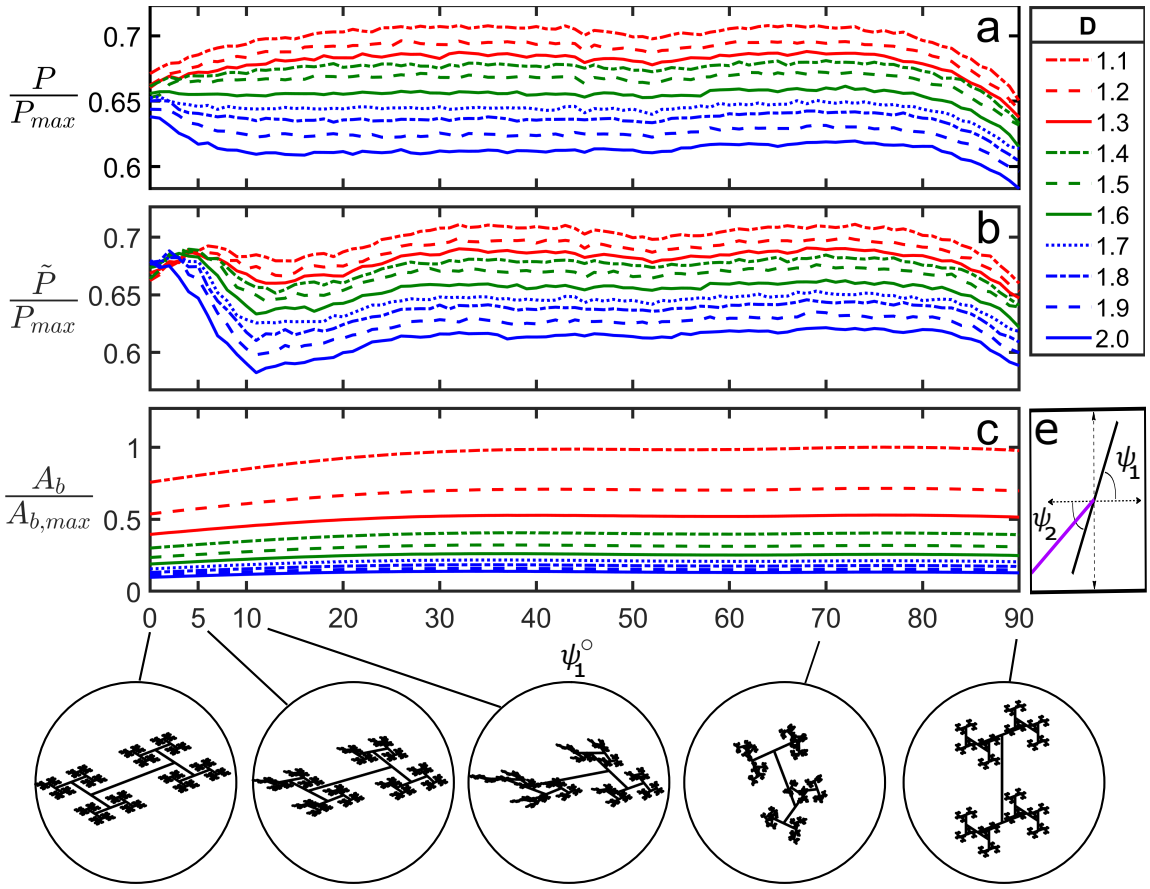

FIGURE 3.4. H-Trees varied between ED2 and ED3 models. The normalized average profile (a), median profile (b), and bounding area (c), are shown as a function of rotation angle ψ, for various D values. ψ_1 varies from the ED2 model ($\psi_1 = 0°$), to a semi-ED2 region ($0 < \psi_1 < 15°$), to a asymmetric-ED3 region ($30° < \psi < 80°$), to the ED3 model ($\psi_1 = 90°$). $\psi_2 = \psi_1 + 180°$. (e) Schematic showing ψ definitions. An incoming segment (purple) bifurcates into two new segments (black).

blocked by another. At angles greater than approximately 15°, every viewing angle has at least some blocking for all D values. We define the range from 30° to 80° as the asymmetric-ED3 region. In this region blocking is more uniform from every viewing angle. Additionally, the bounding area, A_b, and both the mean profile (P) and median profile ($\tilde{P}$) maintain relatively constant values for all D values compared to the variation that exists in the semi-ED2 region for many D values.

We have introduced the median profile because we have identified it as varying with ψ and having a physical interpretation that is different than the mean profile. When a distribution is symmetric the two are identical, but given an asymmetric distribution the median is a better predictor of the most likely outcome because it is less affected by outliers. For an axon that connects with a dendrite, it would be more likely to established a connection from any random direction if the dendritic morphology had a larger median profile. However, for the mean profile those outliers are very important because a neuron can make lots of connections at that viewpoint. Therefore, having a larger mean profile signifies that if axons are connecting from every direction, then the total number of connections would also be larger.

We now ask the same question as before. If axons approach uniformly from every direction, can we predict the more likely model? If we compare $\psi = 0°$ and $\psi = 90°$, then the former always maximizes G/K for the same reason the ED2 did when axons approached from a single direction, $\psi = 0°$ has a higher profile (both mean and median) and a lower bounding area no matter what D value we inspect. However, if considering semi-ED2 and asymmetric-ED3 structures then the largest profile (mean or median) does not always exist at $\psi = 0$. In figure 3.4 the red curves are D values where the maximum P and $\tilde{P}$ occur in the asymmetric-ED3 region, the green curves are D values where the max P is in the asymmetric-ED3 region but the max $\tilde{P}$ is the semi-ED2 region, and the blue curves are D values where the maximum P and $\tilde{P}$ occur in the semi-ED2 region.

For high D values (blue) at least, a semi-ED2 model is always preferred as the benefit from a higher P and $\tilde{P}$ is combined with a lower A_b. For low D values (red) an asymmetric-ED3 has a relatively large P and $\tilde{P}$, but any low D structure

pays an increasingly large A_b cost. For mid range D values (green) it depends on the relative importance of P and $\tilde{P}$, and the importance of the A_b cost. We do not have a robust theory for how any neuron type weighs these benefits and costs, therefore we cannot directly determine which model is preferred for low or mid range D values in the uniform axon input condition.

We can however investigate the relative importance of P and $\tilde{P}$ for the CA1 hippocampal neurons in Chapter 2. We do this by comparing the connectivity maps of H-Trees near the mean D value of the neurons (D=1.4) and at different values of ψ (Fig. 3.5). Does a neuron increase the mean profile? Or does it want to increase the probability that an axon approaching from any direction makes a connection ($\tilde{P}$)?

The connectivity map 'signature' that matches both the apical and basal CA1 hippocampal neurons (Fig. 3.5) is at the minimum ψ (13°) in Fig. 3.4b. Therefore, it is reasonable to assume that it is more important for a neuron to maximize the mean compared to the median profile. The connectivity map 'signature' identified is a right-skewed distribution of profile values (Fig. 3.5f).

3.1.4. Predicting the connection from two regions

The connectivity maps elucidate the axonal input directions for the CA1 hippocampal neurons that have the largest profiles. By looking at regions of the connectivity maps (sets of viewpoints) we can predict the relative proportion of axons approaching from a particular direction. We do so by comparing the measured profile in that region to a naive expectation of the profile. The naive expectation is such that the fraction of the total profile in that region matches the fraction of the total viewpoints that make up a viewing region. For example a

viewing region with 10% of the viewpoints would have 10% of the total profile. If we however calculate 15% of the total profile in that region, we would identify that as having 50% more profile and would predict 50% more axons connecting with dendritic morphologies from that viewing region.

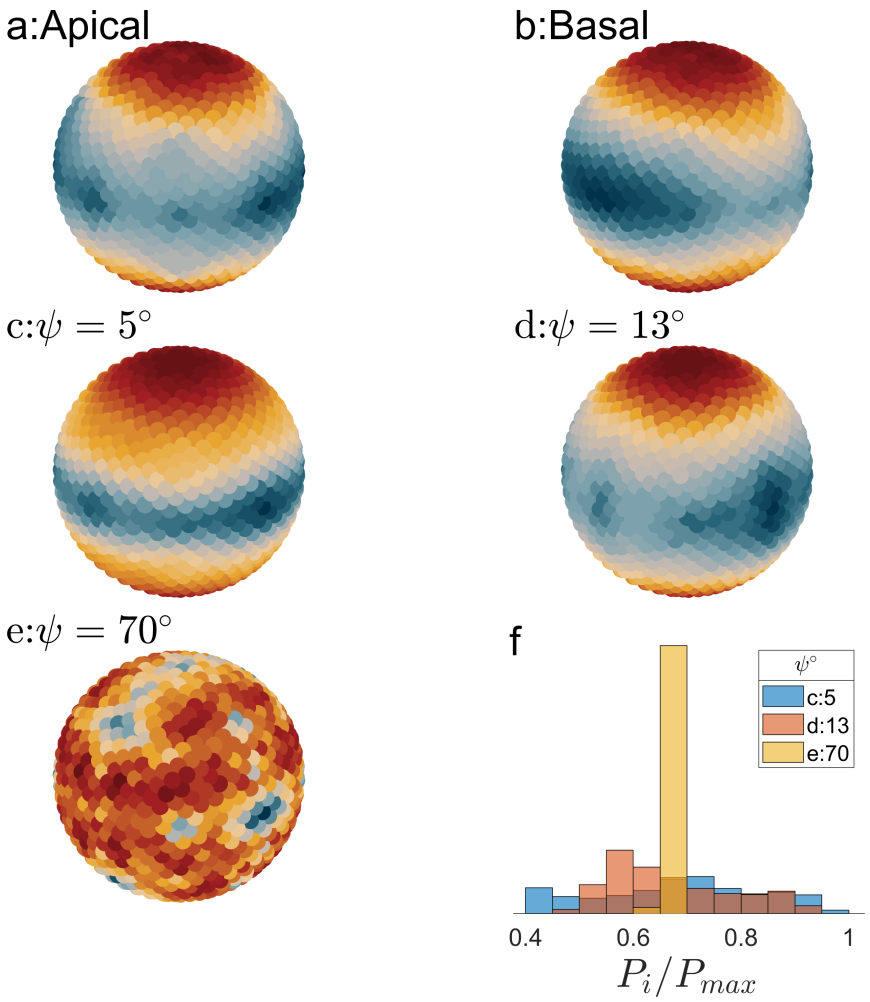

FIGURE 3.5. Connectivity map comparison. Connectivity maps for apical (a) and basal (b) dendrites, as well as for H-Trees with various values of ψ(c,d,e). Larger profile regions (red) in (a,b) are from the view of the incoming parallel fibers. Each color range is set individually for each connectivity map (a,b,c,d,e). (f) Histogram of normalized profile from individual viewpoints in (c,d,e). The range of profile values is much narrower in (e) than (c,d) as can be seen in (f).

We identify two viewing regions of interest: 1) viewpoints associated with incoming parallel fibers (Schaffer collaterals) and 2) viewpoints in a ring perpendicular to region 1 (Fig. 3.6). We restrict both regions to 10% of the total viewpoints. In region 1 this corresponds to a spherical cap with a solid angle of 51.6° centered on the incoming direction of the parallel fibers ($\hat{z}$-direction in Fig. 2.5c). In region 2 this corresponds to a ring with an angular width of 11.5°.

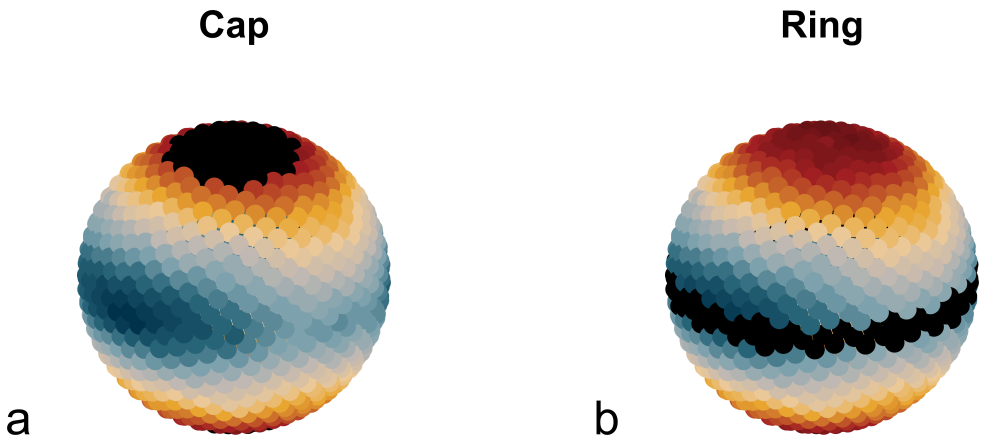

FIGURE 3.6. Two viewing regions of interest. The color black identifies viewpoints within a region of interest.(a) Region 1: a spherical cap associated with the direction of incoming parallel fibers.(b) Region 2: a ring perpendicular to region 1. Both regions are displayed overlapping the apical connectivity map and account for 10% of the total viewpoints.

Using this analysis on the basal and apical connectivity maps, we predict 11% and 19% more axons respectively connecting with dendrites from viewpoints in region 1 than one would naively expect (Fig. 3.2). This is in contrast to region 2, where 7% and 14% fewer axons would connect with basal and apical dendritic morphologies from viewpoints in that region respectively. Furthermore, we notice that the apical and basal values are much less polarized than the ED2 and semi-ED2 H-Trees, and more polarized than the asymmetric-ED3 and ED3 H-Trees.

Structure	Region 1: Cap	Region 2: Ring
basal	+11%	-7%
apical	+19%	-14%
H-Tree ($\psi = 0°$)	+39%	-55%
H-Tree ($\psi = 5°$)	+38%	-40%
H-Tree ($\psi = 13°$)	+32%	-19%
H-Tree ($\psi = 70°$)	-1%	-1%
H-Tree ($\psi = 90°$)	-5%	-5%

TABLE 3.2. Relative connectivity from two incoming axon directions. Quantitative predictions for the relative increase/decrease for axons connecting with neuron and H-Tree models from viewpoints in a spherical cap and ring region compared to a naive expectation.

Currently, a host of complex mapping techniques are utilized in order to identify the relative number of axons from different neuron types that connect with a particular neuron [95]. If tested and proven accurate, the predictions in Table 3.2 could allow a researcher to identify the relative numbers of connecting neuron types based solely on the receiving neuron's morphology. This would inform a further link between structure and function we have not previously touched on, which infers the quality of processing that a neuron executes based on the relative quantity of different types of neurons that connect with it.

3.1.5. Neurons modeled as H-Trees summary

We have applied the fractal framework that was established in Chapter 2 and introduced a cost-benefit formalism. We first asked which D value maximizes the benefit to cost ratio given a model (ED2 or ED3) and an axon condition (uniform or unidirectional). We found that a D=2 geometry would maximize the benefit to cost ratio for either model for the unidirectional condition. In uniform condition

we found the same competing benefits and costs for either model could explain the peak at D=1.4 we found for the CA1 hippocampal neurons in Chapter 2.

Next we asked if we could predict either a ED2 or ED3 model given an axon condition. We found in the unidirectional condition that the cost-benefit analysis predicted an ED2 model for any D value. In the uniform condition our analysis still predicted an ED2 model, even though there are clearly ED3 neurons in the brain. We then investigated H-Tree models that vary between the ED2 and ED3 model with the angle ψ. We defined a semi-ED2 and asymmetric-ED3 region and found that the region that maximized the average and median profile was dependent on D. ED2 and semi-ED2 models were still favored for high D values (1.7-2.0), but the framework could not predict exactly for low- or mid-range D values which region would be preferred. However, we were able to indirectly investigate whether the mean and median profile had a larger impact on the neuron morphology. We compared the connectivity maps of the CA1 hippocampal neurons in Chapter 2 to H-Trees. The mid-range D values of the neurons had a profile signature at the edge of the semi-ED2 region, where the median profile was a minimum. Thus it is more important for a neuron to maximize the mean compare to the median profile.

Finally, based on our analysis of profile connectivity maps, we predicted 11% and 19% more axons innervating basal and apical dendrites respectively in the direction of the parallel fibers. We identified that with these results a researcher could theoretically determine the relative numbers of connecting neurons of different types on to a target neuron based solely on the receiving neuron's morphology.

3.2. Applying the framework to electrode design

Here we consider retinal electrodes with varying constructions (Fig. 3.7). Instead of fixing the total length as before, we fix the electrode footprint, A_f. Where A_f is defined as the square area that contains the entire electrode (including the photodiode and the outer ground electrode), which is particularly relevant as it is advantageous to fit more electrodes into a given area [96]. We also fix the feature width and the number of iterations. For convenience we construct the electrode pattern using method 2 in Appendix A.2. For the two ED3 fractal constructions (Fig. 3.7(b,c)) the height of the electrode is half the electrode width. In Section 3.1 our target structures were dendrites and we envisioned axons connecting with them. Now we consider an electrode to be the target with dendrites connecting with the electrode. In this case, when the electrode is biased by a voltage it will produce an electric field that contributes to stimulating the neurons that have extended processes into the vicinity of the electrode [14, 23]. Processes that connect to an electrode also create a tensile force that pulls the neuron closer to the electrode, or even parts of the electrode (if it's flexible enough) to the neuron. As before we have a set of potentially relevant physical parameters; P, V_m, A_s, A_b, A_f and L_t.

The profile, P, is still relevant as it determines the connectivity and indirectly the stimulating efficiency of the electrode. Because we are interested in retinal electrodes, we also consider the light let through to the photodiode (i.e. the footprint minus the light blocked in the $\hat{z}$-direction by the stimulating and ground electrode). The bounding area, A_b, varies between Electrode 1 (E1) and the other two, but they are constant between Electrode 2 (E2) and Electrode 3 (E3). The total electrode length, L_t, doesn't hold the same meaning as it

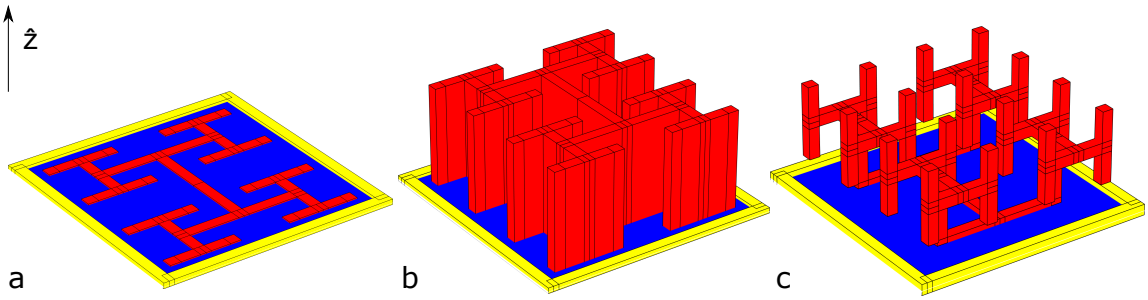

FIGURE 3.7. Comparison of three electrode models. All constructions have the same footprint, ground electrode (yellow), and photodiode area (blue). Feature width and iterations are chosen such that they block the same amount of light from the z-direction. The surface area of the electrode pattern (red) holds a charge to stimulate neurons. (a) Electrode 1 (E1) has a planar construction with a height of 250nm, D=2, and 2 iterations. (b) Electrode 2 (E2) has a planar construction but is extruded to a height that is half the pattern width, D=2, and 2 iterations. (c) Electrode 3 (E3) has a 3D H-Tree construction, D = 3, and 2 iterations. The full 3D structure is bisected such that its first "H" lies flat on the photodiode. Thus the height is half the pattern width. See Section A.2 for construction.

did with neurons, and its effects should be viewed through other parameters. Adding additional material is not inherently detrimental in the fabrication of a microfabricated electrode and therefore the volume of mass, V_m, is negligible. However, the way this material is distributed is important. Critically, the surface area of the electrode pattern, A_s, is no longer a cost to the system but instead the driver of capacitance that stimulates nearby neurons.

3.2.1. Comparing electrode constructions

First we compare E1 to E2/3. The surface area of the E1 pattern is 5 times less than the E3 pattern and 11 times less than the E2 pattern. Consequently the capacitance is far inferior for E1 than either E2 or E3. However, even E1 is better at stimulating neurons than a traditional square electrode [23]. Second, E2/3 can penetrate further into the retina, bringing the stimulating field closer to the functional neurons it intends to stimulate [97]. The physically larger size

could however induce more trauma than a shorter electrode. This response might be mitigated, or even eliminated by features that mimic the retinas natural environment (e.g. natural height variation). Finally, E2/3 has the same profile from the z-direction, but if you include all angles that neuron processes might approach the electrode from, then the profile is much larger for both E2/3 compared to E1.

So long as the electrode is sufficiently strong to survive insertion and one does not cause undue trauma to the retina, it is only logical to construct electrodes that have some height to them.

We now compare E2 to E3. First, E2 always has more surface area than E3. For example, considering the electrodes described in Table 3.3 E2 has 2.5 times the surface area compared to E3. With one more iteration, E2 has 1.4 times the surface area compared to E3. This trend approaches equal surface areas for high iterations and small feature widths. We take note that traditionally typical D=3 fractals like E3 are thought to have more surface area for a given bounding area than a D=2 fractal, but we note that the pattern in E2 is not a typical D=2 fractal as it is extruded with a large height. In particular, E2 arrives at such a high pattern surface area by using much more material than E3. Consequently, E3 has more space open at the size scale of the smallest iteration. These openings ($> 2\mu m$ for electrodes in Table 3.3) could allow more processes to make their way inside the bounding area of E3 compared to E2. More processes that are closer to the electrode would be beneficial for stimulation. A single process might connect with several points on a pattern which could increase adhesion. Additionally, glial cells could also penetrate into the structure on the level of the substrate, supporting neurons more directly and with fewer cells. If the feature sizes are

chosen (or the number of iterations is increased) such that the gaps are too small for a neuron process to penetrate into the structure, the E3 would still have a more varied topography. With enough iterations the varied topography could mimic fractal mountains, which have been shown to increase neuron growth [98, 99].

Property	E1	E2	E3
Connectivity (off axis)	Low	High	Med
Insertion Trauma	Low	High	High
Fluid flow	High	Low	Med
Electrode Surface Area	155 μm^2	1,975 μm^2	796 μm^2
Fabrication Technique	Established	Established	Not Established
Penetration	250 nm	20 μm	20 μm
Flexibility	Med	Low	High
Exerted fluid forces	Low	High	Med
Structural stability	High	Med	Low
Nano-scale roughness	Med	High	Med
Photodiode area	258 μm^2	258 μm^2	258 μm^2

TABLE 3.3. Comparison of electrode designs. A summary table comparing the properties of the 3 electrode designs in Fig. 3.7, with a 20 $\mu m \times 20$ μm footprint, 18 μm pattern width, 2 iterations, a feature width of $1\mu m$, and a ground electrode width of $1\mu m$.

E2 would likely be more stable than E3 but also would have greater forces exerted on it due to the large flat sidewalls. This stability might come at the cost of flexibility. Fractals are mechanically flexible, a desirable property for implanting electrodes in the curved space at the back of the eye [15]. However, the large amount of material in E2 might add an undesirable rigidity [100] to the design. E3 might even out-compete E1 in terms of flexibility with its relatively small pattern-substrate contact area.

Retinal fluid, which contains nutrients and helps with waste removal [36] would not be able to perfuse through E2 as easily as with E3, thus increasing the

risk of a defense response and a rejection of the electrode [101]. Fluid flow could even work to dislodge the electrode from its base, which could be more likely with the large euclidean walls of E2.

3.2.2. Electrode comparison summary

We have seen that Electrode 2 has some functional advantages and it best suits established CNT fabrication techniques [102]. Additionally the CNTs have the advantage of an inherent nano-scale roughness that promotes neuron growth and adhesion (i.e. CNTs are biophilic without modification). Electrode 3 has many advantages over Electrode 1 and 2. However, it would have the most intricate fabrication challenges. Complicated ED3 structures can be fabricated with techniques such as two photon lithography [103], however adding a metallic layer would increase the complexity of the design even further. Electrode 1 can be fabricated with a thin metal layer, yet it is the least functional electrode presented for most of the desirable properties. For both Electrode 1 and 3 ensuring that the metallic layer is biophilic would be an added technical challenge.

Another commonly fabricated electrode beyond the 3 presented here is a fractal mountain [98, 99]. Fractal mountains have high capacitance and high connectivity. However, their traditional design would block incoming light and would lack the mechanical flexibility of fractal branched structures. Most crucially, we hypothesize that it is important to have fractal branches (akin to neurons) to encourage neurons to maintain proximity to an electrode once they are growing along it. We propose an experiment to test this hypothesis in the next chapter.

CHAPTER IV

NEURONS INTERACTING WITH PATTERNED CNTS: AN EXPERIMENT PROPOSAL

By examining the profile we discussed in Chapter 3, we investigated the likelihood of a neuron making contact with an electrode. In this chapter we propose an experiment to examine how the neuron interacts with the electrode after contact has been established. In particular we investigate whether we can increase the probability of a neuron maintaining contact with an electrode as we adjust electrode parameters. In Chapter 1 we considered this question at large scales, now we propose an experiment to map out a strategy at the size scale of a single neuron.

In Chapter 2 we showed that neurons have characteristic weave and forking angles. We propose that it is advantageous for them to maintain those characteristic angles after having established a connection with an electrode. If we provide an electrode that has those characteristic angles available to the neurons, will they increase their probability of maintaining proximity to the electrode? We have preliminary evidence that shows that neurons follow features that are at the same width as their processes (Fig. 4.1a). However, when neurons grow along those features they are constantly exploring their surroundings, presumably searching for other features to grow along that also support their growth. What if we were able to provide an underlying pattern for sufficient unconstrained growth, but without completely covering the surface with an electrode? Can we identify the precise geometric characteristics that promote natural branching patterns? If we do, will we see more growth or other desirable behaviors?

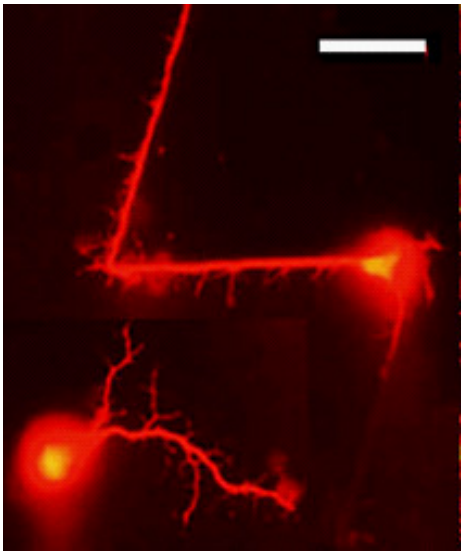

FIGURE 4.1. Neurons interacting with textured and smooth surfaces. The top neuron follows a textured V-shaped line, while the bottom neuron grows fractal dendrites on a nearby smooth surface. The white scale bar is 20 μm and the texture is patterned in SU8.

Generally we may design an experiment in two fundamentally different ways: A holistic approach might look at many neuron processes together on a non-trivial branching electrode, where-as a reductionist approach might look at individual neuron branching dynamics in a limited environment. The holistic approach is exciting but runs the risk of being unable to control the relevant parameters of interest in a reproducible way. The reductionist approach might miss unintended discoveries due to its narrow focus. This chapter offers a reductionist map for future experiments that could be performed independently or in tandem with the holistic approach.

We seek to understand the branching dynamics of neuron processes at the single neuron level. We propose a control group of uniform CNTs and an experimental group of varying branching angle electrodes informed by the description of neuron morphology given in Chapter 2 (e.g. branch lengths,

branching angles, and turning angles. Fig. 2.1). We specifically include angles that match those of the reconstructed CA1 hippocampal neurons in Chapter 2. We focus on branching and turning angle dynamics to see how changes in an underlying texture change specific growth behaviors. This experimental setup would allow a researcher to compare the *in vivo* neuronal branching dynamics to conditions where a neuron is more or less likely to be able to maintain its natural morphology *in vitro*. We predict that when the natural morphology is encouraged (or at least not restricted) by the underlying pattern that the chance of maintaining contact with the electrode will be increased. This in turn could be used in the retina, or in any neuron-electrode interface to enhance the efficacy of stimulation.

Crucially we propose an experiment with a meaningful null result. If there is no response to different patterns compared to uniform CNT patterns, then that would be valuable information in the design of electrodes as other more important features could be focused on without a reduction in performance. If specific patterns are favored as we expect, then that could be used to tune the ability of neurons to maintain connection with an electrode material.

4.1. Culture design

4.1.1. Culture procedure

We are interested in the dynamics of single neurons interacting with patterns. Therefore we suggest that pattern samples are placed in a culture of randomly sampled dissociated mouse retinal cells as described in Section 1.4 (although we note that many culture procedures would be sufficient for similar results). We propose a 7 day *in vitro* culture to minimize superfluous glial growth.

At this duration we have previously demonstrated that cultures typically have glial cells, but minimal to no glial proliferation, and still have healthy neuron growth. Additionally, diluting the seeding density by half would help to avoid misidentification of one neurite with one from another neuron.

To minimize any potential variation in culturing and fabrication, we strongly suggest that both are accomplished in rapid succession over a period of less than two months. We propose 3 separate cultures of 16 samples each (12 in the experimental group and 4 in the control). Three separate cultures is the minimum necessary to properly account for biological variation from one culture to another, and including 16 samples of each would provide a sufficient number of interactions for robust statistics.

4.1.2. Pattern element

We propose implementing pattern elements that are reminiscent of the 3D neurons introduced in Chapter 2 at locations where a neurite bifurcates or turns. We suggest the construction of a pattern element fabricated out of CNTs with varying angles (Fig. 4.2). Each pattern element consists of a central node with extending line segments at angles described by α and δ. All line segments of the pattern element are intended to guide neuron growth at the single neurite size scale. Therefore, we suggest a width and height of 2μm, which is approximately the diameter of a neurite.

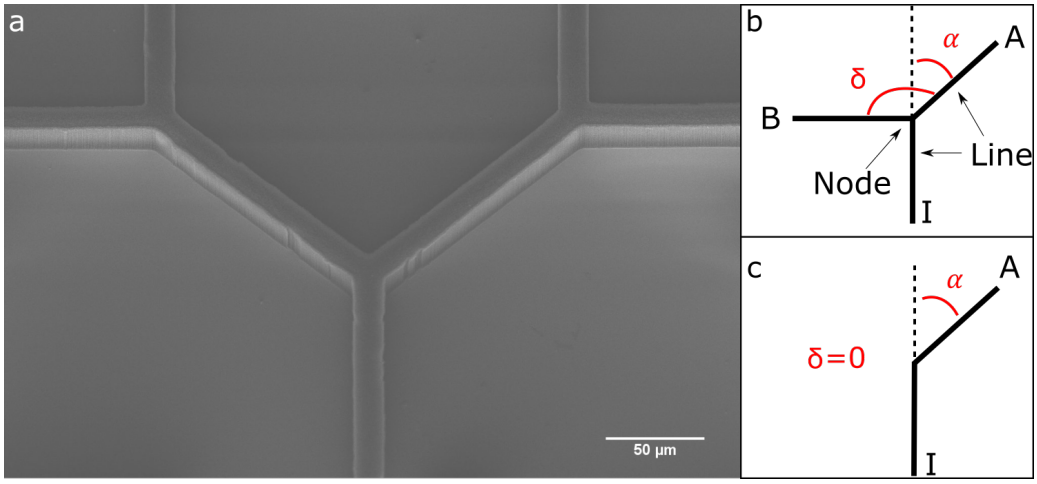

FIGURE 4.2. Pattern element description. (a)Example scanning electron microscope image of vertically aligned CNTs patterned on a silicon substrate. The proposed line segments for this experiment will have a width and height of 2 μm.(b) At a node there are 3 straight line segments, I, A, & B. The direction of A is defined by the angle α from the extended line of I. The direction of B is defined by the angle δ from the A segment. (c) When $\delta = 0$ only one outgoing line segment exists. This pattern isolates the turning angle and establishes a reference point for other behaviors.

4.1.3. Pattern

A single pattern is comprised of 10 (7 for $\delta = 0°$) pattern elements. Each pattern is set to have an identical central pattern element with $\alpha = 60°$ and $\delta = 120°$. The rest of the pattern elements explore combinations of α ($-30°$ to $90°$) and δ ($0°$ to $\alpha + 90°$). We specifically propose a set of pattern elements at $\delta = 75°$ ($\alpha = 0°$,37.5°, and $75°$) because it matches typical branching angles of the CA1 hippocampal neurons. See Fig. 4.3 for all patterns.

The length distribution of the patterns is held constant and is set by the fractal dimension to D = 2 (Fig. 4.4a). These lengths optimize pattern packing while maintaining enough space between line segments for reliable data.

The angle definition assumes that a neurite grows from a pattern's central node outwards but in actuality a neuron could grow in any direction. If we

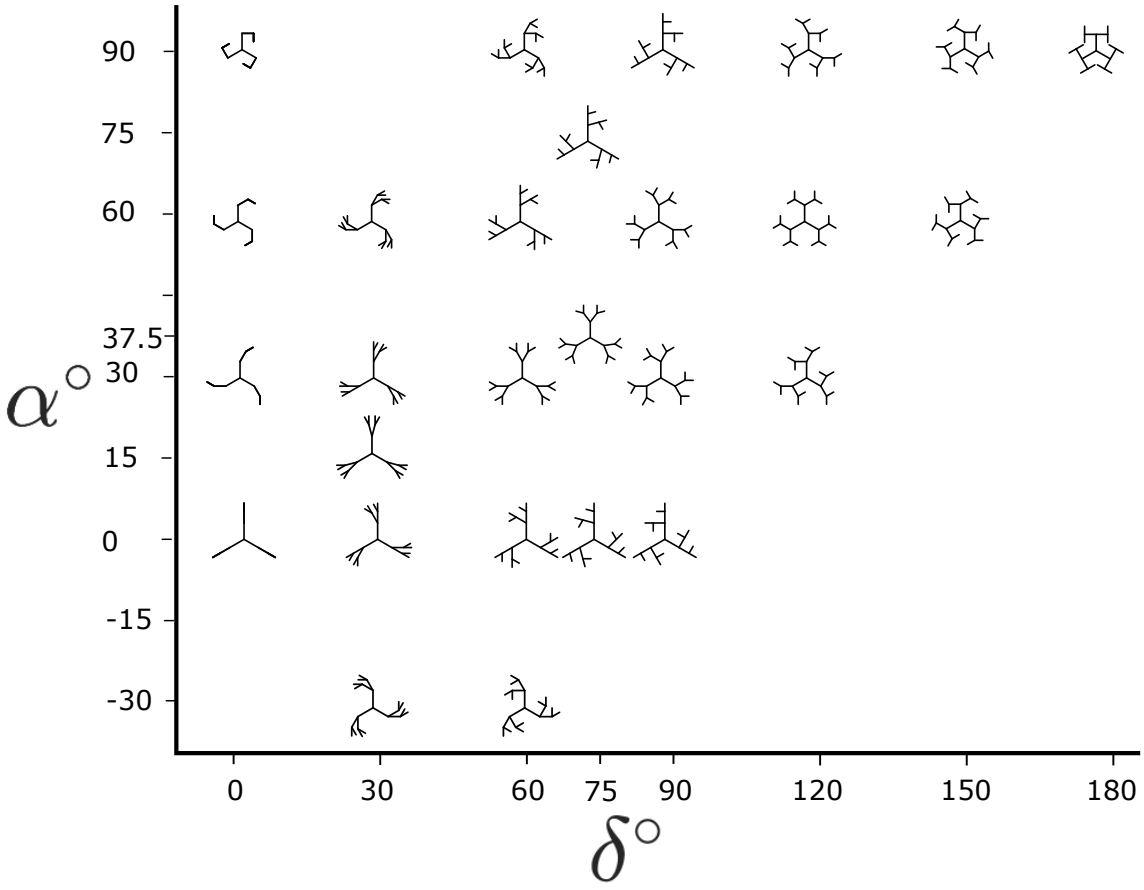

FIGURE 4.3. All patterns. A schematic showing all individual patterns on the sample. ∼220 of each pattern will be on a sample.

consider these new possibilities of α and δ (Fig. 4.4b), then our parameter space increases by more than half.

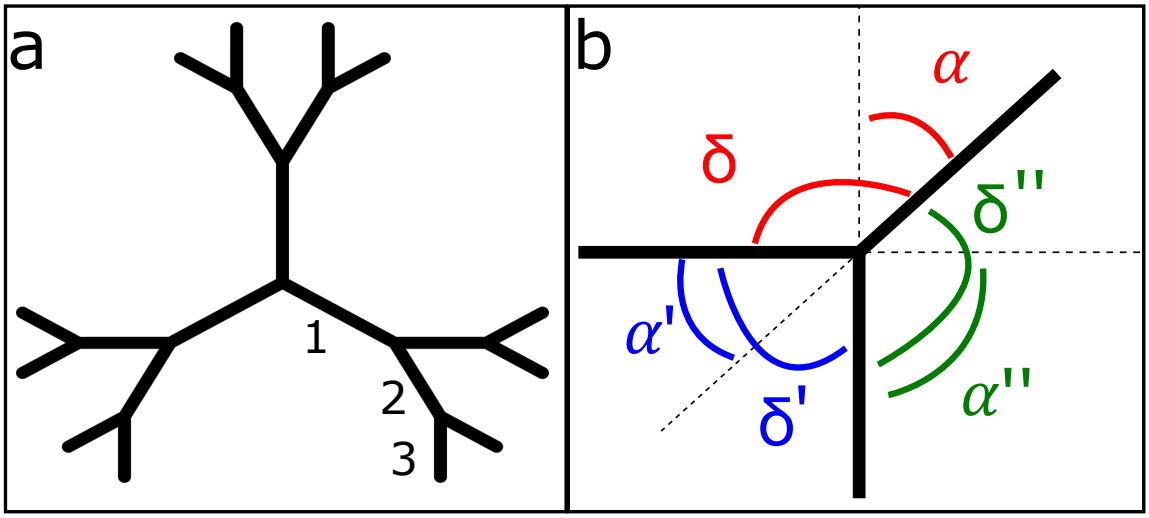

FIGURE 4.4. Pattern description. (a) A single pattern is shown with $\alpha = 30°$ and $\delta = 60°$. The lengths of segments 1, 2, and 3 are given by $L_1 = 20\ \mu m$, $L_2 = \frac{L_0}{\sqrt{2}}$, and $L_3 = \frac{L_0}{2}$. The pattern's dimensions are $80.2\mu m \times 69.5\mu m$. (b) A larger parameter space of angles is obtained when considering that a neurite could grow inwards along any part of the pattern element. These angles are given by: $\alpha' = \pi - \delta : \delta' = \pi + \alpha - \delta : \alpha'' = \delta - \alpha : \delta'' = \pi - \alpha$

4.1.4. Pattern repeat

Each pattern can be inscribed in a rectangle with an area of $6,000\ \mu m^2$. Three patterns of each type are randomly distributed on a 9×9 grid (Fig: 4.5a). A single sample has an area of investigation of $6mm \times 6mm$ which can accommodate ~6000 patterns. 27 pattern types correspond to ~220 patterns of each type (and ~57000 pattern elements) per sample.

4.1.5. Control

We propose a CNT serpinski carpet as a control sample (Fig. 4.5b). The side lengths of the individual squares that comprise the entire pattern are 80 μm, 240

μm, 720 μm, and 2160 μm. This control has large isotropic CNT regions where neuron growth direction on the surface is topographically unbiased. The various square sizes serve a dual purpose: 1) CNT surface topology can vary with height and CNT height can vary with the size of the area being grown. The individual patterns have a relatively small area of CNTs being grown and therefore would likely have a different surface topography than any of the squares. By including a multi-scale set of squares a researcher could track any differences in neuron growth behavior within the control group. Statistically identical growth dynamics between square sizes would provide evidence that growth dynamic differences are due to differences in the experimental and control group. If statistically different growth dynamics between square sizes were observed, then the quality of behavior change could potentially be extrapolated to the experimental group. 2) We established that glial cells have a strong proximity dependent effect on neurons in Section 1.4. Multi-scaled square sizes would ensure that some glial cells are far from neurons but others are close, increasing the likelihood of matching the neuron-glia distances in the experimental group established by random seeding.

4.2. Quantifying neuron behavior

A neurite growing along a line segment of a pattern element towards a node can exhibit one of five behaviors. A neurite will:

1. Terminate Growth
2. Grow off the pattern
3. Grow along the A branch
4. Grow along the B branch

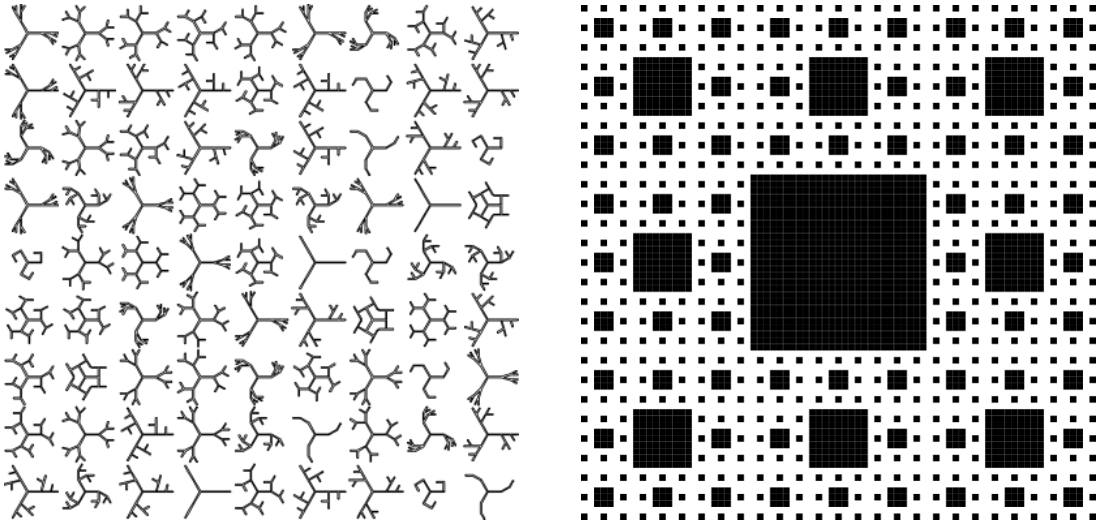

(a) (b)

FIGURE 4.5. Experimental pattern repeat and control. (a) Pattern repeat including all 27 patterns (3 of each) randomly distributed in a 9 × 9 grid.(b) A serpinski carpet control with squares ranging in side length from 80 μm to 2160 μm.

5. Bifurcate (β)

To simplify the results these behaviors should first be identified in regions far from the influence of glial cells.

4.2.1. Primary questions

The behavior observed would likely depend on the angles of that pattern element. We ask:

1. What is the probability of a bifurcation (β) given α and δ? Prob($\beta|\alpha, \delta$)

2. What is the preference for the A segment given α and δ? Prob(A$|\alpha, \delta$)

First, we predict a peak near the δ that matches the CA1 hippocampal neurons, $\delta = 75°$ (Fig. 4.6a). Furthermore, the probability might maximize close to the symmetric value of α. Second, we have previously identified that neurites

will make extreme turns (at least up to 90°) when following an edge, but from our analysis of 3D neurons we see that turning angles are relatively small. We predict a preference for straight trajectories since those are closest to the *in vivo* condition (Fig. 4.6b). Regardless of whether or not the prediction is satisfied, the topography of this plot would be particularly interesting.

Additionally it would be fruitful to analyze neuron behaviors on patterns compared to large isotropic regions on a control sample (Fig. 4.5b). By identifying the neuron's branching and turning angles on this isotropic surface one could determine the characteristic angles (we expect a branching angle of $\sim 75°$ based off of our 3D analysis). Next, a researcher would compare neurons grown on patterns with the angles that match the characteristic angles to patterns with different angles. By quantifying observable differences, such as neurite length, it will shed light on if they are enhanced when the angles match. If for example the neurite length is increased then the first purpose of this study would be satisfied, to maximize the chances of a neuron process following an electrode.

Explicitly we ask:

3. If we match a condition (e.g branching angle) observed on an unbiased CNT region, will that correspond to unique behavior (e.g. increased neuron length) on the pattern?

4.3. Data analysis

Fluorescence microscopy can be used to image neurons, glia, and nuclei separately. Data analysis tools would need to be built in addition to those established by our group, not only to identify glia and neurons, but also to track the direction of neurite growth, distances between cells, branching angles, and

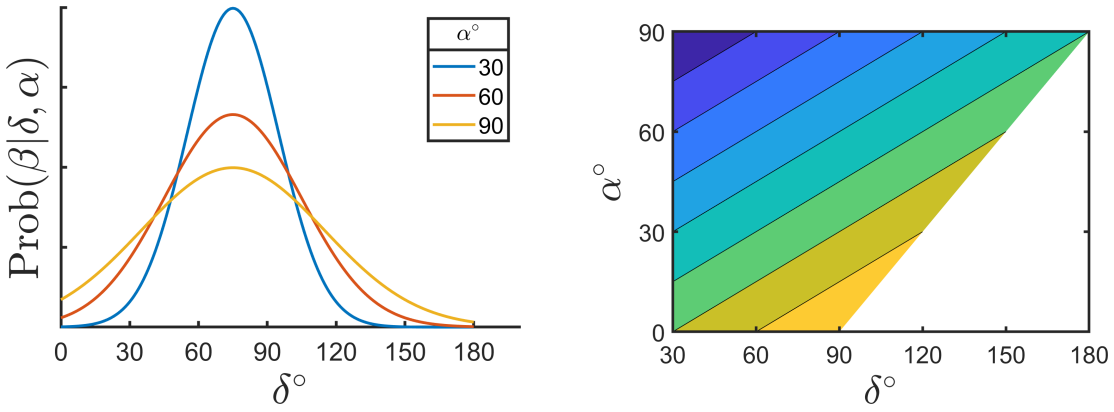

FIGURE 4.6. Predicted results. (a) Probability of a bifurcation given α and δ. (b) Possible segment A/B preference results. Preference for segment A is given by 'warmer' colors, and for B by 'cooler' colors.

turning angles. These tools combined will allow the creation of a 'library' of neuron morphology and behavior.

4.4. Secondary questions

For our primary questions the proximity of a neurite to other neurons and glia was controlled for. Ultimately the aim is to develop a model that includes geometric effects and the distances to other cells.

We propose a model of the form,

$$F(\alpha, \delta, \vec{G}, \vec{N}) = f(\alpha, \delta) + g(\vec{G}) + n(\vec{N}),$$

where 'g' and 'n' are yet to be determined functions of the relative distances to nearby glial ($\vec{G}$) and neural ($\vec{N}$) cells, and 'f' accounts for geometric effects of the underlying pattern. F is then the combined influence from which we calculate the probability of a neurite exhibiting a behavior at a node. In particular we seek to examine $Prob(\beta|F)$ and $Prob(A|F)$.

4.5. Conclusions

Ultimately, the fundamental question we ask here is simple but potentially profound. Is there enhanced behavior by matching the scale and branching patterns of the electrodes to the neuron behavior?

We're hopeful that the aforementioned approach of reducing neuron morphology into its primary descriptors and analyzing that behavior in response to varying physical environments will not only elucidate the fundamental branching dynamics of a neuron as it grows along an electrode, but will also help in the design of a better implant-retina interface.

CHAPTER V

CONCLUSIONS

From the results in the introduction we know that a simple system can be created that hinders glial growth on an electrode surface and simultaneously improves neuronal growth, while keeping glia inside Si areas in close contact with neurons on both surfaces. The neuronal small-world network created an efficient communication mechanism between neurons on both surfaces, thereby increasing the area of neurons that could stimulate downstream neurons. Furthermore, we found that we could modify the proliferation of glial cells and the small-world network properties by changing the D value of the electrode. The *in vitro* experiments were done at a large scale ($\sim$ $6mm$), however, each individual electrode used in a retinal prosthesis would need to be much smaller ($20\mu m$ for a theoretical 20/80 vision). Still, these large scale *in vitro* experiments present a map for the design of future electrode arrays. Those electrode arrays would not be restricted to subretinal implant technologies. The fundamental findings of their interactions with neurons and glia could be utilized in implants that interface with other parts of the central nervous system.

We showed in the introduction that a fractal electrode at the size scale of just a few neurons was better at stimulating surrounding neurons than a square electrode, potentially leading to an improved visual acuity. Furthermore, the fractal electrode stimulated the same neurons but required less power from incoming light via a photodiode.

Large scale networks and small scale electrical results provide a promising path towards designing better functioning electrodes. However, we identified that

it would be important to further investigate the fundamental behaviors of neurons in order to design electrodes that facilitate better neuron-electrode connections.

In Chapter 2, we investigated how neurons exploit fractal geometry to optimize their network connectivity, which addresses a major question concerning the operation of the human body - how neurons optimize their connections to each other in order to form a network. The results from this chapter have broad implications such as providing a framework for interpreting Connectome data to increase the viability of novel medical implants designed to interface with neurons. Previous studies showed that neurons are composed of fractal branching patterns, but it was not clear how neurons benefit from these patterns and to what extent they were fractal. To better understand these two questions we constructed 3-dimensional models of rat hippocampal neurons using confocal microscopy to identify the precise geometric properties that contribute to their fractal character.

Unexpectedly, we found that neurons are not like other commonly branched fractals such as trees where the distribution of branch lengths dominate their fractal characteristics. Instead, we showed that the ways in which the branches fork and weave through space are important determiners of their connectivity and costs. By manipulating the weave and fork angles of the branches in the neuron models, we created distorted neurons that deviate from their natural state. We examined their evolving properties as a function of a geometric parameter called fractal dimension D.

Based on the fractal framework we developed, we proposed that the neuron D values quantify network cooperation that balances the neurons need to connect to their neighbor neurons with the energetic cost of maintaining this connectivity. Neurons have the ability to develop more branches to connect to their neighbors,

but each extra branch requires vital operational energy. The neurons solve this dilemma using their fractal character to fine-tune the connectivity of the branches using D.

We show that this fractal strategy can be achieved with branch patterns that repeat over only one order of magnitude of scale. Furthermore, we found that neurons adopt the opposite geometric strategy to fractal trees whereas tree branches become increasingly small further from the central trunk, the neuron branches become longer. The impetus for this lies in the neurons need to minimize signal transport times within the arbor. This is achieved with short branches close to the soma while the H-Tree suffers from longer branches.

Our fractal framework allows neurons, including healthy and pathological neurons (e.g. Alzheimers) and even artificial neurons, to be compared to many branching objects. For example, our results can inform the choice of the D values of fractal electrodes used in retinal implants designed to combat diseases such as macular degeneration. In addition to medical applications, our fractal framework provides an automated approach for fundamental research that allows researchers to easily analyze large amounts of data (e.g. the 121,544 neurons on neuromorpho.org).

In Chapter 3 we applied the fractal framework that was established in Chapter 2 and we introduced a cost-benefit formalism that we first used to calculate the behaviors of our CA1 hippocampal neurons using heavily constrained exact H-Tree models. We assessed two conditions: One in which axons approach from a single direction and the other in which axons approached from many directions uniformly. In the former we found that a D=2 geometry would maximize the benefit to cost ratio. In the latter we found the same competing

benefits and costs could explain the peak at D=1.4 we found for the CA1 hippocampal neurons in Chapter 2.

Next we asked whether an ED2 or ED3 model would maximize the benefit to cost ratio for those same two conditions. We found that when axons come from a single direction, the cost-benefit analysis predicts an ED2 model for any D value, which is consistent with what we see in the literature (e.g. Purkinje cells). When axons approach uniformly from many directions our analysis still predicted an ED2 model, even though there are ED3 neurons in the brain. This result motivated us to transform H-Tree smoothly between the ED2 and ED3 model. We defined a semi-ED2 and asymmetric-ED3 region and found that the region that maximized the average and median profile was dependent on D. We predicted which region would be preferred for a set of the D values. Furthermore, we identified results that indicated that it is more important for a neuron to maximize the mean compared to the median profile.

The direction that they favored corresponds to parallel axon fibers that pass through CA1. Based on our analysis of profile connectivity maps, we predicted 11% and 19% more axons connecting to Basal and Apical dendrites respectively in the direction of the parallel fibers.

In the next section of Chapter 3, we applied the fractal framework to compare 3 different electrode designs for bio-compatibility, connectivity, and ease of fabrication. We found that for the two most critical properties, surface area, and connectivity, electrodes that extended into 3 dimensions (ED3) achieved higher values than a mostly flat electrode. The height of the ED3 electrodes also brought them closer to the neurons they would stimulate. However, they paid a penalty in the ease that fluid would flow across them. Still, when considering all the

properties for most applications, it would be unlikely that the flat electrode would perform better than either of the ED3 electrodes. Between the two ED3 electrodes it was clear that the specific requirements of the application would dictate which electrode was best suited.

In Chapter 4 we proposed an experiment to investigate the fundamental behaviors of neurons interacting with patterned CNTs. This experiment would serve two purposes: 1) to understand how to maximize the chances of maintaining proximity to the electrode once the neuron has reached it and 2) to learn the fundamental branching dynamics of neurons as they grow along an electrode. The experiment would build on the knowledge we learned in the previous chapters; the techniques established in the introduction, the fundamental properties of neuron branching dynamics discovered in Chapter 2, and the principles of electrode design established in Chapter 3.

We must consider a host of relevant features in order to design a better electrode. The system dynamics of retinal cells, their interactions with artificial surfaces at the single neuron size scale, the stimulation power of a single electrode, knowing how neurons curve through space in-vivo, the use of fabrication techniques to increase electrode surface area, connectivity, or fluid flow - all of these are necessary components, but none in isolation are sufficient. However, if we consider these concepts in tandem we might break free from established designs that fall short of theoretical maximums, achieve a much better electrode interface, and improve the quality of life for those who benefit from these technologies and the fundamental research that makes them possible.

APPENDIX

H-TREE FUNCTION DEFINITIONS

In this appendix function definitions are defined for exact H-Trees.

A.1. Method 1: H-trees with lengths that decrease every branch

We work in the regime such that the width of any branch is much smaller than the bounding length of any pattern.

A.1.1. ED2 H-trees

The side length of the entire ED2 H-Tree in the $\hat{x}$, $\hat{y}$, and $\hat{z}$ direction is

$$L_x(D, N, L_1) = 2L_1 \sum_{n=0}^{N/2} \frac{1}{2^{2n/D}}, \tag{A.1}$$

$$L_y(D, N, L_1) = 2L_1 \sum_{n=0}^{(N-1)/2} \frac{1}{2^{(2n+1)/D}}, \tag{A.2}$$

$$L_z(W) = W, \tag{A.3}$$

where W is the width of a branch, N is the number of iterations minus 1, D is the fractal dimension, and L_1 is the length of the initial segment.

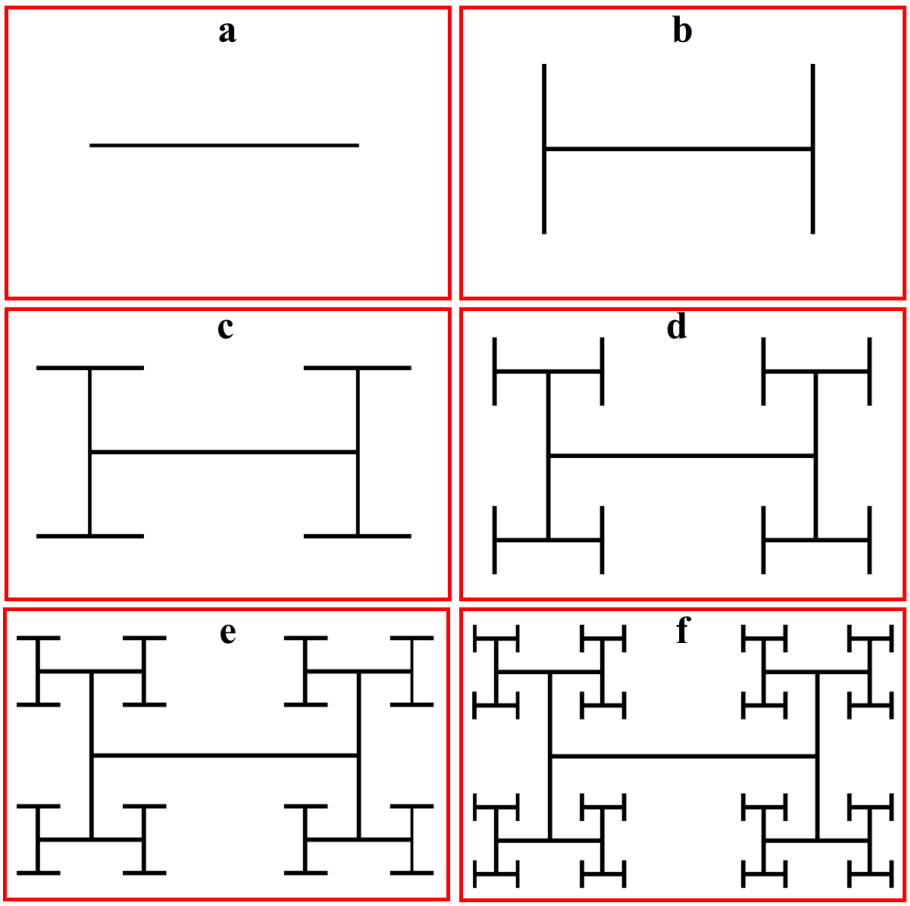

FIGURE A.1. H-Tree generation: Method 1. Schematic of different stages of an H-tree fractal generation. a) through f) show consecutive stages of generating an H-tree with D = 1.5 and 6 iterations. Reprinted with permission from the author [24]

A.1.2. ED3 H-trees

The side length of the entire ED3 H-Tree in the $\hat{x}$, $\hat{y}$, and $\hat{z}$ direction is

$$L_x(D,N,L_1) = 2L_1 \sum_{n=0}^{N/3} \frac{1}{2^{3n/D}}, \tag{A.4}$$

$$L_y(D,N,L_1) = 2L_1 \sum_{n=0}^{(N-1)/3} \frac{1}{2^{(3n+1)/D}}, \tag{A.5}$$

$$L_z(D,N,L_1) = 2L_1 \sum_{n=0}^{(N-2)/3} \frac{1}{2^{(3n+2)/D}}. \tag{A.6}$$

A.1.3. Definitions for both ED2 & ED3 models

The convex hull bounding volume is given by

$$V_B = L_x L_y L_z. \tag{A.7}$$

The area is given by

$$A_B = 2L_x L_y + 2L_z L_y + 2L_x L_z. \tag{A.8}$$

The total length of all the branches is

$$L = L_1 \sum_{n=0}^{N} 2^{n+1} \left(\frac{1}{2^{1/D}} \right)^n. \tag{A.9}$$

Therefore the volume occupied by the branches is

$$V_m = \pi \left(\frac{W}{2} \right)^2 L \tag{A.10}$$

and the surface area is

$$A_s = \pi W L. \tag{A.11}$$

A.2. Method 2: H-Trees with lengths that decrease every 'H'

For method 2 H-Trees all lengths in the H are equal, and each H is scaled down according to D. For ED3 method 2 H-Trees, there is a length in each dimension that is constant, and that entire structure is scaled down. Segments are rectangular, with a width W in both transverse directions. No simplifying assumptions are made.

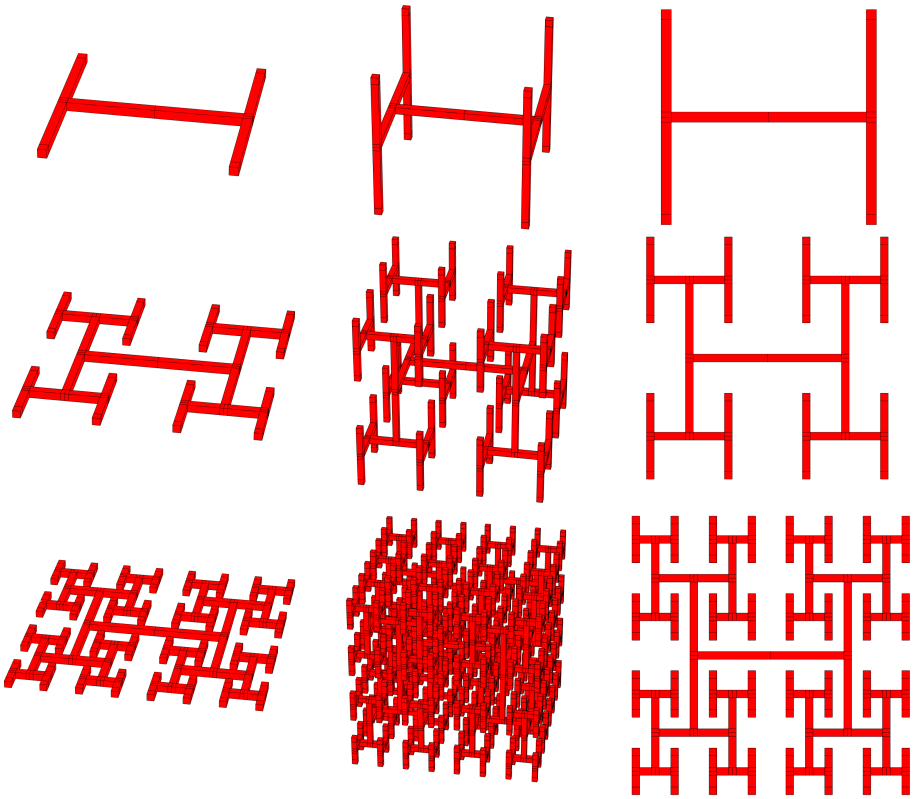

FIGURE A.2. H-Tree generation: Method 2. Each row is a new iteration. (Left Column) ED2 generation method for a D=2 fractal with H=W. (Middle Column) ED3 generation method for a D=3 fractal. (Right Column) View from above without perspective for both generation methods. From this viewpoint they have the same profile.

A.2.1. ED2

The side length of the entire ED2 H-Tree in either the $\hat{x}$ or $\hat{y}$ direction is

$$L_{xy} = W + 2L_1 \sum_{n=0}^{N} \frac{1}{4^{n/D}}. \tag{A.12}$$

The bounding volume is given by

$$V_B = HL_{xy}^2. \tag{A.13}$$

The area by

$$A_B = 2L_{xy}^2 + 4HL_{xy}. \tag{A.14}$$

The total length of all the branches is

$$L = \frac{W}{2}4^{N+1} + 6L_1 \sum_{n=0}^{N} \left(\frac{4}{4^{1/D}} \right)^n. \tag{A.15}$$

Therefore the volume occupied by the branches is

$$V_m = WH \left(L - W - \frac{3W}{2} \sum_{n=1}^{N} 4^n \right) \tag{A.16}$$

and the surface area is

$$A_s = (2H + W)L + HW4^{N+1} - \frac{1}{2}(4HW + W^2)(2 + 3\sum_{n=1}^{N} 4^n). \tag{A.17}$$

The profile in the $\hat{z}$ direction is

$$P_z = W \left(L - W - \frac{3W}{2} \sum_{n=1}^{N} 4^n \right). \tag{A.18}$$

The smallest gap is

$$S_H = L_1 \left(\frac{1}{4^{(N-1)/D}} - \frac{1}{4^{N/D}} \right) - W \tag{A.19}$$

and the maximum segment width without overlap is

$$W_{max} = \frac{\sqrt{A}}{-1 + 2^{2+N}}. \tag{A.20}$$

A.2.2. 3D

The side length of the entire ED3 H-Tree in the $\hat{x}$, $\hat{y}$, or $\hat{z}$ direction is

$$L_{xyz} = W + 2L_1 \sum_{n=0}^{N} \frac{1}{8^{n/D}}. \tag{A.21}$$

The bounding volume is given by

$$V_B = L_{xyz}^3. \tag{A.22}$$

The area is given by

$$A_B = 6L_{xyz}^2. \tag{A.23}$$

The footprint, A_f, is the square area of entire electrode The total length of all the branches is

$$L = \frac{W}{2} 8^{N+1} + 14L_1 \sum_{n=0}^{N} \left(\frac{8}{8^{1/D}} \right)^n. \tag{A.24}$$

Therefore the volume of the mass is

$$V_m = W^2 \left(L - 3W - \frac{7W}{2} \sum_{n=1}^{N} 8^n \right) \tag{A.25}$$

and the surface area is

$$A_s = W \left(4L + W8^{N+1} - W \left(18 + 21 \sum_{n=1}^{N} 8^n \right) \right). \tag{A.26}$$

The profile in the $\hat{z}$ direction is

$$P_z = W \left(\frac{4^{N+1}}{2} + 6L_0 \sum_{n=0}^{N} \frac{4^n}{8^{n/D}} - W - \frac{3W}{2} \sum_{n=1}^{N} 4^n \right) \tag{A.27}$$

REFERENCES CITED

[1] James B. Bassingthwaighte, Larry S. Liebovitch, and Bruce J. West. *Fractal Physiology*. Methods in Physiology. Springer-Verlag, New York, 1994. ISBN 978-1-4614-7572-9. URL https://www.springer.com/gp/book/9781461475729.

[2] Philip M. Iannaccone and Mustafa Khokha. *Fractal Geometry in Biological Systems: An Analytical Approach*. CRC Press, Boca Raton, FL, 1 edition edition, September 1996. ISBN 978-0-8493-7636-8.

[3] The Petilla Interneuron Nomenclature Group (PING), Giorgio A. Ascoli, Lidia Alonso-Nanclares, Stewart A. Anderson, German Barrionuevo, Ruth Benavides-Piccione, Andreas Burkhalter, Gyrgy Buzski, Bruno Cauli, Javier DeFelipe, Alfonso Fairn, Dirk Feldmeyer, Gord Fishell, Yves Fregnac, Tamas F. Freund, Daniel Gardner, Esther P. Gardner, Jesse H. Goldberg, Moritz Helmstaedter, Shaul Hestrin, Fuyuki Karube, Zoltn F. Kisvrday, Bertrand Lambolez, David A. Lewis, Oscar Marin, Henry Markram, Alberto Muoz, Adam Packer, Carl C. H. Petersen, Kathleen S. Rockland, Jean Rossier, Bernardo Rudy, Peter Somogyi, Jochen F. Staiger, Gabor Tamas, Alex M. Thomson, Maria Toledo-Rodriguez, Yun Wang, David C. West, and Rafael Yuste. Petilla terminology: nomenclature of features of GABAergic interneurons of the cerebral cortex. *Nature Reviews Neuroscience*, 9(7): 557–568, July 2008. ISSN 1471-0048. doi: 10.1038/nrn2402. URL https://www.nature.com/articles/nrn2402.

[4] T. G. Smith Jr., G. D. Lange, and W. B. Marks. Fractal methods and results in cellular morphology dimensions, lacunarity and multifractals. *Journal of Neuroscience Methods*, 69(2):123–136, November 1996. ISSN 0165-0270. doi: 10.1016/S0165-0270(96)00080-5. URL http://www.sciencedirect.com/science/article/pii/S0165027096000805.

[5] Sidiney Alves. Fractal patterns for dendrites and axon terminals. *Physica A*, 232, 1996.

[6] S.L. Wearne, A. Rodriguez, D.B. Ehlenberger, A.B. Rocher, S.C. Henderson, and P.R. Hof. New techniques for imaging, digitization and analysis of three-dimensional neural morphology on multiple scales. *Neuroscience*, 136 (3):661–680, January 2005. ISSN 03064522. doi: 10.1016/j.neuroscience.2005.05.053. URL http://linkinghub.elsevier.com/retrieve/pii/S0306452205005865.

[7] BRENDAN ZIETSCH and ELSTON ELSTON. FRACTAL ANALYSIS OF PYRAMIDAL CELLS IN THE VISUAL CORTEX OF THE GALAGO (OTOLEMUR GARNETTI):: REGIONAL VARIATION IN DENDRITIC BRANCHING PATTERNS BETWEEN VISUAL AREAS. *Fractals*, 13(2): 83–90, June 2005.

[8] Mark A. Wood and Kenneth A. Ellenbogen. Cardiac Pacemakers From the Patients Perspective. *Circulation*, 105(18):2136–2138, May 2002. ISSN 0009-7322, 1524-4539. doi: 10.1161/01.CIR.0000016183.07898.90. URL http://circ.ahajournals.org/content/105/18/2136.

[9] *Cochlear Implants*. August 2015. URL https://www.nidcd.nih.gov/health/cochlear-implants. Publication Title: NIDCD.

[10] *Medtronic Innovation in Deep Brain Stimulation*. 2016. URL https://www.medtronicdbs.com/why-dbs/innovation-leader/index.htm.

[11] Catherine G.Y. Ngan, Rob M.I. Kapsa, and Peter F.M. Choong. Strategies for neural control of prosthetic limbs: from electrode interfacing to 3D printing. *Materials*, 12(12), June 2019. ISSN 1996-1944. doi: 10.3390/ma12121927. URL https://www.ncbi.nlm.nih.gov/pmc/articles/PMC6631966/.

[12] Eberhart Zrenner. Will Retinal Implants Restore Vision? *Science*, 295(5557): 1022–1025, February 2002. ISSN 0036-8075, 1095-9203. doi: 10.1126/science.1067996. URL http://science.sciencemag.org/content/295/5557/1022.

[13] William Watterson, Saba Moslehi, Julian Smith, Rick Montgomery, and Richard Taylor. Fractal Electronics as a Generic Interface to Neurons. In *The Fractal Geometry of the Brain*, pages 553–565. Springer, 2016.

[14] William J. Watterson, Rick D. Montgomery, and Richard P. Taylor. Modeling the Improved Visual Acuity Using Photodiode Based Retinal Implants Featuring Fractal Electrodes. *Frontiers in Neuroscience*, 12, April 2018. ISSN 1662-453X. doi: 10.3389/fnins.2018.00277. URL http://journal.frontiersin.org/article/10.3389/fnins.2018.00277/full.

[15] Jonathan A. Fan, Woon-Hong Yeo, Yewang Su, Yoshiaki Hattori, Woosik Lee, Sung-Young Jung, Yihui Zhang, Zhuangjian Liu, Huanyu Cheng, Leo Falgout, Mike Bajema, Todd Coleman, Dan Gregoire, Ryan J. Larsen, Yonggang Huang, and John A. Rogers. Fractal design concepts for stretchable electronics. *Nature Communications*, 5:ncomms4266, February 2014. ISSN 2041-1723. doi: 10.1038/ncomms4266. URL https://www.nature.com/articles/ncomms4266.

[16] Farzaneh Afshinmanesh, Alberto G. Curto, Kaveh M. Milaninia, Niek F. van Hulst, and Mark L. Brongersma. Transparent Metallic Fractal Electrodes for Semiconductor Devices. *Nano Letters*, 14(9):5068–5074, September 2014. ISSN 1530-6984, 1530-6992. doi: 10.1021/nl501738b. URL http://pubs.acs.org/doi/abs/10.1021/nl501738b.

[17] Guanhai Li, Xiaoshuang Chen, Bo Ni, Oupeng Li, Lujun Huang, Yuan Jiang, Weida Hu, and Wei Lu. Fractal H-shaped plasmonic nanocavity. *Nanotechnology*, 24(20):205702, May 2013. ISSN 0957-4484, 1361-6528. doi: 10.1088/0957-4484/24/20/205702. URL http://stacks.iop.org/0957-4484/24/i=20/a=205702?key=crossref.d8f2d49c3b6580af5eae13092e2dcac5.

[18] Yong-Jun Bao, Hong-Min Li, Xiao-Chun Chen, Ru-Wen Peng, Mu Wang, Xiang Lu, Jun Shao, and Nai-Ben Ming. Tailoring the resonances of surface plasmas on fractal-featured metal film by adjusting aperture configuration. *Applied Physics Letters*, 92(15):151902, 2008. ISSN 00036951. doi: 10.1063/1.2908972. URL http://scitation.aip.org/content/aip/journal/apl/92/15/10.1063/1.2908972.

[19] Samuel Gottheim, Hui Zhang, Alexander O. Govorov, and Naomi J. Halas. Fractal Nanoparticle Plasmonics: The Cayley Tree. *ACS Nano*, 9(3):3284–3292, March 2015. ISSN 1936-0851, 1936-086X. doi: 10.1021/acsnano.5b00412. URL http://pubs.acs.org/doi/abs/10.1021/acsnano.5b00412.

[20] Duncan J. Watts and Steven H. Strogatz. Collective dynamics of small-world networks. *Nature*, 393(6684):440–442, June 1998. ISSN 1476-4687. doi: 10.1038/30918. URL https://www.nature.com/articles/30918. Number: 6684 Publisher: Nature Publishing Group.

[21] Daniel de Santos-Sierra, Irene Sendia-Nadal, Inmaculada Leyva, Juan A. Almendral, Sarit Anava, Amir Ayali, David Papo, and Stefano Boccaletti. Emergence of Small-World Anatomical Networks in Self-Organizing Clustered Neuronal Cultures. *PLOS ONE*, 9(1):e85828, January 2014. ISSN 1932-6203. doi: 10.1371/journal.pone.0085828. URL https://journals.plos.org/plosone/article?id=10.1371/journal.pone.0085828.

[22] Orit Shefi, Ido Golding, Ronen Segev, Eshel Ben-Jacob, and Amir Ayali. Morphological characterization of in vitro neuronal networks. *Physical Review E*, 66(2):021905, August 2002. doi: 10.1103/PhysRevE.66.021905. URL https://link.aps.org/doi/10.1103/PhysRevE.66.021905.

[23] William Watterson. *Fractal interfaces for stimulating and recording neural implants*. PhD Thesis, 2017.

[24] Saba Moslehi. *Bio-inspired fractal electrodes interfacing with retinal cells*. PhD Thesis, University of Oregon, Eugene, OR, March 2020.

[25] Benoit Mandelbrot and Roberto Pignoni. *The fractal geometry of nature*, volume 173. WH freeman, New York, 1983.

[26] David Avnir, Ofer Biham, Daniel Lidar, and Ofer Malcai. Is the Geometry of Nature Fractal? *Science*, 279(5347):39–40, January 1998. ISSN 0036-8075, 1095-9203. doi: 10.1126/science.279.5347.39. URL https://science.sciencemag.org/content/279/5347/39.

[27] Rick Daniel Montgomery. *Fractal electrodes for interfacing neurons to retinal implants*. PhD Thesis, University of Oregon, 2014. URL http://search.proquest.com/openview/6c8e1a5a056f65bcd06db34dfad174e8/1?pq-origsite=gscholar&cbl=18750&diss=y.

[28] P. A. Rutecki. Neuronal excitability: voltage-dependent currents and synaptic transmission. *Journal of Clinical Neurophysiology: Official Publication of the American Electroencephalographic Society*, 9(2):195–211, April 1992. ISSN 0736-0258.

[29] Fundamental Neuroscience - 4th Edition, . URL https://www.elsevier.com/books/fundamental-neuroscience/squire/978-0-12-385870-2.

[30] F. Irie and Y. Yamaguchi. Eph Receptor Signaling and Spine Morphology. In Larry R. Squire, editor, *Encyclopedia of Neuroscience*, pages 1141–1145. Academic Press, Oxford, January 2009. ISBN 978-0-08-045046-9. doi: 10.1016/B978-008045046-9.01799-X. URL http://www.sciencedirect.com/science/article/pii/B978008045046901799X.

[31] Mark F. Bear. *Neuroscience : exploring the brain /*. Lippincott Williams & Wilkins,, Baltimore ;, 3rd ed. edition. ISBN 978-0-7817-7607-3.

[32] P. Werginz, H. Benav, E. Zrenner, and F. Rattay. Modeling the response of ON and OFF retinal bipolar cells during electric stimulation. *Vision Research*, 111:170–181, June 2015. ISSN 0042-6989. doi: 10.1016/j.visres.2014.12.002. URL http://www.sciencedirect.com/science/article/pii/S0042698914003046.

[33] R Heidelberger and G Matthews. Calcium influx and calcium current in single synaptic terminals of goldfish retinal bipolar neurons. *The Journal of Physiology*, 447(1):235–256, February 1992. ISSN 1469-7793. doi: 10.1113/jphysiol.1992.sp019000. URL http://onlinelibrary.wiley.com/doi/10.1113/jphysiol.1992.sp019000/abstract.

[34] A. L. Hodgkin and B. Katz. The effect of sodium ions on the electrical activity of the giant axon of the squid. *The Journal of Physiology*, 108(1):37–77, March 1949. ISSN 0022-3751. URL http://www.ncbi.nlm.nih.gov/pmc/articles/PMC1392331/.

[35] Hui Ye and Amanda Steiger. Neuron matters: electric activation of neuronal tissue is dependent on the interaction between the neuron and the electric field. *Journal of NeuroEngineering and Rehabilitation*, 12(1):65, August 2015. ISSN 1743-0003. doi: 10.1186/s12984-015-0061-1. URL https://doi.org/10.1186/s12984-015-0061-1.

[36] Daniel Palanker, Alexander Vankov, Phil Huie, and Stephen Baccus. Design of a high-resolution optoelectronic retinal prosthesis. *Journal of Neural Engineering*, 2(1):S105–S120, March 2005. ISSN 1741-2560, 1741-2552. doi: 10.1088/1741-2560/2/1/012. URL http://stacks.iop.org/1741-2552/2/i=1/a=012?key=crossref.106811c61075b3756df8d685234fc998.

[37] NeuroMorpho.Org - a centrally curated inventory of digitally reconstructed neurons, . URL http://neuromorpho.org/.

[38] D. Attwell and S. B. Laughlin. An energy budget for signaling in the grey matter of the brain. *Journal of Cerebral Blood Flow and Metabolism: Official Journal of the International Society of Cerebral Blood Flow and Metabolism*, 21(10):1133–1145, October 2001. ISSN 0271-678X. doi: 10.1097/00004647-200110000-00001.

[39] Lucia Rodrguez-Berdini and Beatriz L. Caputto. Lipid Metabolism in Neurons: A Brief Story of a Novel c-Fos-Dependent Mechanism for the Regulation of Their Synthesis. *Frontiers in Cellular Neuroscience*, 13, 2019. ISSN 1662-5102. doi: 10.3389/fncel.2019.00198. URL https://www.frontiersin.org/articles/10.3389/fncel.2019.00198/full. Publisher: Frontiers.

[40] Anne-Sophie Hafner, Paul G. Donlin-Asp, Beulah Leitch, Etienne Herzog, and Erin M. Schuman. Local protein synthesis is a ubiquitous feature of neuronal pre- and postsynaptic compartments. *Science*, 364(6441):eaau3644, May 2019. ISSN 0036-8075, 1095-9203. doi: 10.1126/science.aau3644. URL https://www.sciencemag.org/lookup/doi/10.1126/science.aau3644.

[41] Larry W. Swanson and Jeff W. Lichtman. From Cajal to Connectome and Beyond. *Annual Review of Neuroscience*, 39(1):197–216, 2016. doi: 10.1146/annurev-neuro-071714-033954. URL https://doi.org/10.1146/annurev-neuro-071714-033954.

[42] Yuh-Nung Jan and Lily Yeh Jan. Branching out: mechanisms of dendritic arborization. *Nature reviews. Neuroscience*, 11(5):316, May 2010. doi: 10.1038/nrn2836. URL https://www.ncbi.nlm.nih.gov/pmc/articles/PMC3079328/.

[43] Wesley B. Grueber and Alvaro Sagasti. Self-avoidance and Tiling: Mechanisms of Dendrite and Axon Spacing. *Cold Spring Harbor Perspectives in Biology*, 2 (9), September 2010. ISSN 1943-0264. doi: 10.1101/cshperspect.a001750. URL https://www.ncbi.nlm.nih.gov/pmc/articles/PMC2926746/.

[44] Frederico A. C. Azevedo, Ludmila R. B. Carvalho, Lea T. Grinberg, Jos Marcelo Farfel, Renata E. L. Ferretti, Renata E. P. Leite, Wilson Jacob Filho, Roberto Lent, and Suzana HerculanoHouzel. Equal numbers of neuronal and nonneuronal cells make the human brain an isometrically scaled-up primate brain. *Journal of Comparative Neurology*, 513(5):532–541, 2009. ISSN 1096-9861. doi: 10.1002/cne.21974. URL https://onlinelibrary.wiley.com/doi/abs/10.1002/cne.21974. _eprint: https://onlinelibrary.wiley.com/doi/pdf/10.1002/cne.21974.

[45] Elena Vecino, F. David Rodriguez, Noelia Ruzafa, Xandra Pereiro, and Sansar C. Sharma. Glianeuron interactions in the mammalian retina. *Progress in Retinal and Eye Research*, 51:1–40, March 2016. ISSN 1350-9462. doi: 10.1016/j.preteyeres.2015.06.003. URL http://www.sciencedirect.com/science/article/pii/S1350946215000452.

[46] Vadim S. Polikov, Patrick A. Tresco, and William M. Reichert. Response of brain tissue to chronically implanted neural electrodes. *Journal of Neuroscience Methods*, 148(1):1–18, October 2005. ISSN 0165-0270. doi: 10.1016/j.jneumeth.2005.08.015. URL http://www.sciencedirect.com/science/article/pii/S0165027005002931.

[47] J. E. Sanders, C. E. Stiles, and C. L. Hayes. Tissue response to single-polymer fibers of varying diameters: evaluation of fibrous encapsulation and macrophage density. *Journal of biomedical materials research*, 52(1):231–237, 2000. URL http://orzo.union.edu/khetans/Teaching/BNG331/Sanders%20et%20al_JBMR_2000__LBL3.pdf.

[48] Takashi D. Yoshida Kozai, Nicholas B. Langhals, Paras R. Patel, Xiaopei Deng, Huanan Zhang, Karen L. Smith, Joerg Lahann, Nicholas A. Kotov, and Daryl R. Kipke. Ultrasmall implantable composite microelectrodes with bioactive surfaces for chronic neural interfaces. *Nature materials*, 11(12): 1065–1073, December 2012. ISSN 1476-1122. doi: 10.1038/nmat3468. URL http://www.ncbi.nlm.nih.gov/pmc/articles/PMC3524530/.

[49] Jonas Thelin, Henrik Jrntell, Elia Psouni, Martin Garwicz, Jens Schouenborg, Nils Danielsen, and Cecilia Eriksson Linsmeier. Implant Size and Fixation Mode Strongly Influence Tissue Reactions in the CNS. *PLOS ONE*, 6(1): e16267, January 2011. ISSN 1932-6203. doi: 10.1371/journal.pone.0016267. URL http://journals.plos.org/plosone/article?id=10.1371/journal.pone.0016267.

[50] Yinghui Zhong and Ravi V. Bellamkonda. Dexamethasone-coated neural probes elicit attenuated inflammatory response and neuronal loss compared to uncoated neural probes. *Brain Research*, 1148:15–27, May 2007. ISSN 0006-8993. doi: 10.1016/j.brainres.2007.02.024.

[51] Stphane Woerly, Van Diep Doan, Norma Sosa, Jean de Vellis, and Araceli Espinosa-Jeffrey. Prevention of gliotic scar formation by NeuroGel allows partial endogenous repair of transected cat spinal cord. *Journal of Neuroscience Research*, 75(2):262–272, January 2004. ISSN 0360-4012. doi: 10.1002/jnr.10774.

[52] Galle Piret, Maria-Thereza Perez, and Christelle N. Prinz. Support of Neuronal Growth Over Glial Growth and Guidance of Optic Nerve Axons by Vertical Nanowire Arrays. *ACS Applied Materials & Interfaces*, 7(34):18944–18948, September 2015. ISSN 1944-8244. doi: 10.1021/acsami.5b03798. URL http://dx.doi.org/10.1021/acsami.5b03798.

[53] Age-Related Macular Degeneration: Facts & Figures, July 2015. URL https://www.brightfocus.org/macular/article/age-related-macular-facts-figures. Library Catalog: www.brightfocus.org.

[54] Raya Sorkin, Alon Greenbaum, Moshe David-Pur, Sarit Anava, Amir Ayali, Eshel Ben-Jacob, and Yael Hanein. Process entanglement as a neuronal anchorage mechanism to rough surfaces. *Nanotechnology*, 20(1):015101, January 2009. ISSN 0957-4484, 1361-6528. doi: 10.1088/0957-4484/20/1/015101. URL http://stacks.iop.org/0957-4484/20/i=1/a=015101?key=crossref.c55f9bc3d60100909e345a12b28b5690.

[55] X Zhang, S Prasad, S Niyogi, A Morgan, M Ozkan, and C Ozkan. Guided neurite growth on patterned carbon nanotubes. *Sensors and Actuators B: Chemical*, 106(2):843–850, May 2005. ISSN 09254005. doi: 10.1016/j.snb.2004.10.039. URL http://linkinghub.elsevier.com/retrieve/pii/S0925400504006999.

[56] Tamir Gabay, Moti Ben-David, Itshak Kalifa, Raya Sorkin, Zeev R Abrams, Eshel Ben-Jacob, and Yael Hanein. Electro-chemical and biological properties of carbon nanotube based multi-electrode arrays. *Nanotechnology*, 18(3): 035201, January 2007. ISSN 0957-4484, 1361-6528. doi: 10.1088/0957-4484/18/3/035201. URL http://stacks.iop.org/0957-4484/18/i=3/a=035201?key=crossref.3acdea8b19cce5afc7fb95a83458fc9b.

[57] Edward Bloch, Yvonne Luo, and Lyndon da Cruz. Advances in retinal prosthesis systems. *Therapeutic Advances in Ophthalmology*, 11, January 2019. ISSN 2515-8414. doi: 10.1177/2515841418817501. URL https://www.ncbi.nlm.nih.gov/pmc/articles/PMC6350159/.

[58] Simon W. Moore and Michael P. Sheetz. Biophysics of substrate interaction: influence on neural motility, differentiation and repair. *Developmental Neurobiology*, 71(11):1090–1101, November 2011. ISSN 1932-8451. doi: 10.1002/dneu.20947. URL https://www.ncbi.nlm.nih.gov/pmc/articles/PMC3307797/.

[59] Saida P. Khan, Gregory G. Auner, and Golam M. Newaz. Influence of nanoscale surface roughness on neural cell attachment on silicon. *Nanomedicine: Nanotechnology, Biology and Medicine*, 1(2):125–129, June 2005. ISSN 15499634. doi: 10.1016/j.nano.2005.03.007. URL http://linkinghub.elsevier.com/retrieve/pii/S1549963405000638.

[60] Natalia Gomez, Shaochen Chen, and Christine E. Schmidt. Polarization of hippocampal neurons with competitive surface stimuli: contact guidance cues are preferred over chemical ligands. *Journal of The Royal Society Interface*, 4 (13):223–233, April 2007. ISSN 1742-5689, 1742-5662. doi: 10.1098/rsif.2006.0171. URL http://rsif.royalsocietypublishing.org/cgi/doi/10.1098/rsif.2006.0171.

[61] Lisa A. Flanagan, Yo-El Ju, Beatrice Marg, Miriam Osterfield, and Paul A. Janmey. Neurite branching on deformable substrates. *Neuroreport*, 13(18): 2411–2415, December 2002. ISSN 0959-4965. doi: 10.1097/01.wnr.0000048003.96487.97. URL https://www.ncbi.nlm.nih.gov/pmc/articles/PMC2408859/.

[62] Daniel Koch, William J. Rosoff, Jiji Jiang, Herbert M. Geller, and Jeffrey S. Urbach. Strength in the periphery: growth cone biomechanics and substrate rigidity response in peripheral and central nervous system neurons. *Biophysical Journal*, 102(3):452–460, February 2012. ISSN 1542-0086. doi: 10.1016/j.bpj.2011.12.025.

[63] Henrik Persson, Carsten Kbler, Kristian Mlhave, Lars Samuelson, Jonas O Tegenfeldt, Stina Oredsson, and Christelle N Prinz. Fibroblasts Cultured on Nanowires Exhibit Low Motility, Impaired Cell Division, and DNA Damage. *Small (Weinheim an Der Bergstrasse, Germany)*, 9(23):4006–4016, December 2013. ISSN 1613-6810. doi: 10.1002/smll.201300644. URL `https://www.ncbi.nlm.nih.gov/pmc/articles/PMC4282547/`.

[64] Sifis Micheloyannis. Graph-based network analysis in schizophrenia. *World Journal of Psychiatry*, 2(1):1–12, February 2012. doi: 10.5498/wjp.v2.i1.1. URL `https://www.wjgnet.com/2220-3206/full/v2/i1/1.htm`. Publisher: Baishideng Publishing Group Inc.

[65] Michele Guida and Funaro Maria. Topology of the Italian airport network: A scale-free small-world network with a fractal structure? *Chaos, Solitons & Fractals*, 31(3):527–536, February 2007. ISSN 0960-0779. doi: 10.1016/j.chaos.2006.02.007. URL `http://www.sciencedirect.com/science/article/pii/S0960077906001792`.

[66] Hidefumi Sawai. A Small-World Network Immune from Random Failures and Resilient to Targeted Attacks. *Procedia Computer Science*, 18:976–985, January 2013. ISSN 1877-0509. doi: 10.1016/j.procs.2013.05.263. URL `http://www.sciencedirect.com/science/article/pii/S1877050913004067`.

[67] V. Latora and M. Marchiori. Efficient behavior of small-world networks. *Physical Review Letters*, 87(19):198701, November 2001. ISSN 0031-9007. doi: 10.1103/PhysRevLett.87.198701.

[68] Manuel Schrter, Ole Paulsen, and Edward T. Bullmore. Micro-connectomics: probing the organization of neuronal networks at the cellular scale. *Nature Reviews Neuroscience*, 18(3):131–146, March 2017. ISSN 1471-0048. doi: 10.1038/nrn.2016.182. URL `https://www.nature.com/articles/nrn.2016.182`.

[69] Per Andersen, Richard Morris, David Amaral, Tim Bliss, and John O'Keefe. *The Hippocampus Book*. Oxford University Press, Oxford ; New York, 1 edition edition, November 2006. ISBN 978-0-19-510027-3.

[70] Quan Wen, Armen Stepanyants, Guy N. Elston, Alexander Y. Grosberg, and Dmitri B. Chklovskii. Maximization of the connectivity repertoire as a statistical principle governing the shapes of dendritic arbors. *Proceedings of the National Academy of Sciences*, 106(30):12536–12541, 2009. URL `http://www.pnas.org/content/106/30/12536.short`.

[71] Diek W Wheeler, Charise M White, Christopher L Rees, Alexander O Komendantov, David J Hamilton, and Giorgio A Ascoli. Hippocampome.org: a knowledge base of neuron types in the rodent hippocampus. *eLife*, 4. ISSN 2050-084X. doi: 10.7554/eLife.09960. URL https://www.ncbi.nlm.nih.gov/pmc/articles/PMC4629441/.

[72] *Neurolucida \textbar Neuron Tracing Software \textbar MBF Bioscience*. . URL https://www.mbfbioscience.com/neurolucida.

[73] F. Caserta, W. D. Eldred, E. Fernandez, R. E. Hausman, L. R. Stanford, S. V. Bulderev, S. Schwarzer, and H. E. Stanley. Determination of fractal dimension of physiologically characterized neurons in two and three dimensions. *Journal of Neuroscience Methods*, 56(2):133–144, February 1995. ISSN 0165-0270.

[74] E Fernndez, J. A Bolea, G Ortega, and E Louis. Are neurons multifractals? *Journal of Neuroscience Methods*, 89(2):151–157, July 1999. ISSN 0165-0270. doi: 10.1016/S0165-0270(99)00066-7. URL http://www.sciencedirect.com/science/article/pii/S0165027099000667.

[75] Hermann Cuntz, Alexandre Mathy, and Michael Husser. A scaling law derived from optimal dendritic wiring. *Proceedings of the National Academy of Sciences of the United States of America*, 109(27):11014–11018, 2012. URL http://www.jstor.org/stable/41601721.

[76] Alexandra Vormberg, Felix Effenberger, Julia Muellerleile, and Hermann Cuntz. Universal features of dendrites through centripetal branch ordering. *PLOS Computational Biology*, 13(7):e1005615, July 2017. ISSN 1553-7358. doi: 10.1371/journal.pcbi.1005615. URL https://journals.plos.org/ploscompbiol/article?id=10.1371/journal.pcbi.1005615.

[77] Sean L. Hill, Yun Wang, Imad Riachi, Felix Schrmann, and Henry Markram. Statistical connectivity provides a sufficient foundation for specific functional connectivity in neocortical neural microcircuits. *Proceedings of the National Academy of Sciences*, 109(42):E2885–E2894, October 2012. ISSN 0027-8424, 1091-6490. doi: 10.1073/pnas.1202128109. URL https://www.pnas.org/content/109/42/E2885.

[78] Dmitri B. Chklovskii. Synaptic Connectivity and Neuronal Morphology: Two Sides of the Same Coin. *Neuron*, 43(5):609–617, September 2004. ISSN 0896-6273. doi: 10.1016/j.neuron.2004.08.012. URL http://www.sciencedirect.com/science/article/pii/S0896627304004982.

[79] Michael P. McAssey, Fetsje Bijma, Bernadetta Tarigan, Jaap van Pelt, Arjen van Ooyen, and Mathisca de Gunst. A Morpho-Density Approach to Estimating Neural Connectivity. *PLoS ONE*, 9(1):e86526, January 2014. ISSN 1932-6203. doi: 10.1371/journal.pone.0086526. URL http://dx.plos.org/10.1371/journal.pone.0086526.

[80] A Stepanyants and D Chklovskii. Neurogeometry and potential synaptic connectivity. *Trends in Neurosciences*, 28(7):387–394, July 2005. ISSN 01662236. doi: 10.1016/j.tins.2005.05.006. URL https://linkinghub.elsevier.com/retrieve/pii/S0166223605001311.

[81] Nir Kalisman, Gilad Silberberg, and Henry Markram. Deriving physical connectivity from neuronal morphology. *Biological Cybernetics*, 88(3): 210–218, March 2003. ISSN 0340-1200, 1432-0770. doi: 10.1007/s00422-002-0377-3. URL http://link.springer.com/10.1007/s00422-002-0377-3.

[82] Geoffrey B. West, James H. Brown, and Brian J. Enquist. A General Model for the Origin of Allometric Scaling Laws in Biology. *Science*, 276(5309): 122–126, April 1997. ISSN 0036-8075, 1095-9203. doi: 10.1126/science.276.5309.122. URL https://science.sciencemag.org/content/276/5309/122.

[83] Jayanth R. Banavar, Amos Maritan, and Andrea Rinaldo. Size and form in efficient transportation networks. *Nature*, 399(6732):130–132, May 1999. ISSN 1476-4687. doi: 10.1038/20144. URL https://www.nature.com/articles/20144.

[84] Toshiaki Takeda, Atsushi Ishikawa, Katsuhiko Ohtomo, Yukio Kobayashi, and Takahide Matsuoka. Fractal dimension of dendritic tree of cerebellar Purkinje cell during onto- and phylogenetic development. *Neuroscience Research*, 13 (1):19–31, February 1992. ISSN 0168-0102. doi: 10.1016/0168-0102(92)90031-7. URL http://www.sciencedirect.com/science/article/pii/0168010292900317.

[85] Elliott J. Mufson, Laura Mahady, Diana Waters, Scott E. Counts, Sylvia E. Perez, Steven DeKosky, Stephen D. Ginsberg, Milos D. Ikonomovic, Stephen Scheff, and Lester Binder. Hippocampal Plasticity During the Progression of Alzheimers disease. *Neuroscience*, 309:51–67, November 2015. ISSN 0306-4522. doi: 10.1016/j.neuroscience.2015.03.006. URL https://www.ncbi.nlm.nih.gov/pmc/articles/PMC4567973/.

[86] Laleh Golestanirad, Behzad Elahi, Alberto Molina, Juan R. Mosig, Claudio Pollo, Robert Chen, and Simon J. Graham. Analysis of fractal electrodes for efficient neural stimulation. *Frontiers in Neuroengineering*, 6, 2013. ISSN 1662-6443. doi: 10.3389/fneng.2013.00003. URL `http://journal.frontiersin.org/article/10.3389/fneng.2013.00003/abstract`.

[87] Hermann Cuntz, Friedrich Forstner, Alexander Borst, and Michael Husser. One Rule to Grow Them All: A General Theory of Neuronal Branching and Its Practical Application. *PLoS Computational Biology*, 6(8):e1000877, August 2010. ISSN 1553-7358. doi: 10.1371/journal.pcbi.1000877. URL `http://dx.plos.org/10.1371/journal.pcbi.1000877`.

[88] Simon L. Altmann. *Rotations, Quaternions, and Double Groups*. Oxford University Press, Oxford Oxfordshire : New York, October 1986. ISBN 978-0-19-855372-4.

[89] de Berg Mark, van Krefeld M, M. Overmars, and O. Schwarzkopf. *Computational Geometry: Algorithms and Applications, Second Edition*. Springer, Berlin ; New York, 2nd edition edition, February 2000. ISBN 978-3-540-65620-3.

[90] Matthew J. Gregory, A. Jon Kimerling, Denis White, and Kevin Sahr. A comparison of intercell metrics on discrete global grid systems. *Computers, Environment and Urban Systems*, 32(3):188–203, May 2008. ISSN 0198-9715. doi: 10.1016/j.compenvurbsys.2007.11.003. URL `http://www.sciencedirect.com/science/article/pii/S0198971507000877`.

[91] lvaro Gonzlez. Measurement of areas on a sphere using Fibonacci and latitude-longitude lattices. *Mathematical Geosciences*, 42(1):49–64, January 2010. ISSN 1874-8961, 1874-8953. doi: 10.1007/s11004-009-9257-x. URL `http://arxiv.org/abs/0912.4540`.

[92] Kazuto Fujishima, Kelly Kawabata Galbraith, and Mineko Kengaku. Dendritic Self-Avoidance and Morphological Development of Cerebellar Purkinje Cells. *The Cerebellum*, 17(6):701–708, December 2018. ISSN 1473-4230. doi: 10.1007/s12311-018-0984-8. URL `https://doi.org/10.1007/s12311-018-0984-8`.

[93] Jordan A. Taylor and Richard B. Ivry. Chapter 9 - Cerebellar and Prefrontal Cortex Contributions to Adaptation, Strategies, and Reinforcement Learning. In Narender Ramnani, editor, *Progress in Brain Research*, volume 210 of *Cerebellar Learning*, pages 217–253. Elsevier, January 2014. doi: 10.1016/B978-0-444-63356-9.00009-1. URL `http://www.sciencedirect.com/science/article/pii/B9780444633569000091`.

[94] H. F. Jelinek and E. Fernandez. Neurons and fractals: how reliable and useful are calculations of fractal dimensions? *Journal of Neuroscience Methods*, 81 (1-2):9–18, June 1998. ISSN 0165-0270.

[95] Trygve B. Leergaard, Claus C. Hilgetag, and Olaf Sporns. Mapping the Connectome: Multi-Level Analysis of Brain Connectivity. *Frontiers in Neuroinformatics*, 6, 2012. ISSN 1662-5196. doi: 10.3389/fninf.2012.00014. URL `https://www.frontiersin.org/articles/10.3389/fninf.2012.00014/full`. Publisher: Frontiers.

[96] Conrad D. James, Robert Davis, M. Meyer, AATA Turner, SATS Turner, GAWG Withers, LAKL Kam, GABG Banker, HACH Craighead, MAIM Issacson, and others. Aligned microcontact printing of micrometer-scale poly-L-lysine structures for controlled growth of cultured neurons on planar microelectrode arrays. *Biomedical Engineering, IEEE Transactions on*, 47(1): 17–21, 2000. URL `http://ieeexplore.ieee.org/xpls/abs_all.jsp?arnumber=817614`.

[97] Joseph Rizzo. Use of Penetrating Electrodes in the Boston Retinal Prosthesis. URL `https://grantome.com/grant/NIH/I01-RX000115-01A1`.

[98] Stuart F. Cogan. Neural Stimulation and Recording Electrodes. *Annual Review of Biomedical Engineering*, 10(1):275–309, 2008. doi: 10.1146/annurev.bioeng.10.061807.160518. URL `https://doi.org/10.1146/annurev.bioeng.10.061807.160518`.

[99] Tams Pajkossy. Electrochemistry at fractal surfaces. *Journal of Electroanalytical Chemistry and Interfacial Electrochemistry*, 300(1):1–11, February 1991. ISSN 0022-0728. doi: 10.1016/0022-0728(91)85379-4. URL `http://www.sciencedirect.com/science/article/pii/0022072891853794`.

[100] Wenwen Yi, Chaoyang Chen, Zhaoying Feng, Yong Xu, Chengpeng Zhou, Nirul Masurkar, John Cavanaugh, and Mark Ming-Cheng Cheng. A flexible and implantable microelectrode arrays using high-temperature grown vertical carbon nanotubes and a biocompatible polymer substrate. *Nanotechnology*, 26(12):125301, 2015. ISSN 0957-4484. doi: 10.1088/0957-4484/26/12/125301. URL `http://stacks.iop.org/0957-4484/26/i=12/a=125301`.

[101] Henri Lorach, Georges Goetz, Richard Smith, Xin Lei, Yossi Mandel, Theodore Kamins, Keith Mathieson, Philip Huie, James Harris, Alexander Sher, and Daniel Palanker. Photovoltaic restoration of sight with high visual acuity. *Nature Medicine*, 21(5):476–482, May 2015. ISSN 1546-170X. doi: 10.1038/nm.3851. URL `https://www.nature.com/articles/nm.3851`. Number: 5 Publisher: Nature Publishing Group.

[102] William J. Watterson, Saba Moslehi, Kara Zappitelli, Julian H. Smith, David Miller, Conor Rowland, Julie Chouinard, Stephen Golledge, Richard P. Taylor, Maria-Thereza Perez, and Benjamin Aleman. The Role of an Aluminum Adhesive Layer on the Biocompatibility and Mechanical Integrity of Vertically Aligned Carbon Nanotubes for Interfacing with Retinal Neurons. *Micromachines*, 2020.

[103] Lucas R. Meza, Alex J. Zelhofer, Nigel Clarke, Arturo J. Mateos, Dennis M. Kochmann, and Julia R. Greer. Resilient 3D hierarchical architected metamaterials. *Proceedings of the National Academy of Sciences*, 112(37): 11502–11507, September 2015. ISSN 0027-8424, 1091-6490. doi: 10.1073/pnas.1509120112. URL `https://www.pnas.org/content/112/37/11502`. Publisher: National Academy of Sciences Section: Physical Sciences.